Physics Studies at a Future Linear Collider

Hajrah Tabassam

A thesis submitted in fulfilment of the requirements
for the degree of Doctor of Philosophy
to the
University of Edinburgh

May 2011

Abstract

With the start of the Large Hadron Collider (LHC) at CERN, we will obtain a new understanding of the physics beyond our current limits. New discoveries will be made; but we will require a deeper understanding, which the LHC machine, being a hadron collider, will not be able to elucidate. Instead, we will need an e^+e^- collider to make precision measurements of the newly discovered phenomena. Electroweak symmetry breaking and the origin of fermion and boson masses are fundamental issues in our understanding of particle physics. The essential piece of electroweak symmetry breaking - the Higgs boson - will probably be discovered at the LHC. If there are one, or more, Higgs boson(s) precise measurements of all properties of the Higgs will be very important.

In this thesis I present two measurements of Standard Model Higgs boson properties in the context of the International Linear Collider (ILC) at $\sqrt{s} = 500$ GeV, using the proposed International Linear Detector (ILD). First a performance study of ILD to measure the branching ratios of the Higgs boson with $m_H = 120$ GeV, where the Higgs boson is produced with a Z-boson via the Higgsstralung process, and the Z decays into e^+e^- or $\mu^+\mu^-$. It will also be essential to study the Higgs Yukawa coupling. Therefore, in the second part of this thesis, I present a study of $e^+e^- \rightarrow t\bar{t}H$ with the aim of making a direct measurement of the the top-Higgs coupling, using the semi-leptonic final state and m_H of 120 GeV. I show that the top-Higgs coupling can be measured with an accuracy of better than 28%.

Declaration

Except where otherwise stated, the research undertaken in this thesis was the unaided work of the author. Where the work was done in collaboration with others, a significant contribution was made by the author.

Hajrah Tabassam
May 2011

Acknowledgements

I would like to record my thanks to all those who have helped me in the course of this work. In particular, the following:

Dr. Victoria Martin, my supervisor for her guidance, assistance and advice over the last three and half years and providing encouragement when things got tough, and for her unflagging interest. She provided me opportunities to get to know a wide range of physicists and different experiments.

Professor Steve Playfer, my second supervisor, for his encouragement and help whenever I need it for my work, specially the second analysis of my thesis would not be possible without his guidance.

Dr. Roberval Walsh with whom first part of this thesis was done. His help and companionship in learning the techniques and tricks of the experimental particles physics is significant. Victoria, Steve and Roberval are the three people who taught me everything I know about experimental high energy physics.

My best friends, Gemma and Ross, without them it would not be easy to accommodate in a new place and integrate in a different culture.

The Higher Education Commission for their financial support.

My parents, my brother and sisters, for their unfailing encouragement and support throughout, and to whom this thesis is dedicated.

Contents

List of Figures

List of Tables

Chapter 1

Introduction

The most intriguing questions for a human being are: "what are we made of?", "what is the origin of this Universe?" and "what will be its end?" Physicists are able to understand the answers to these questions in the evolution of the universe from the Big Bang to its present appearance in terms of galaxies, stars, black holes, chemical elements and biological systems: the key role is of elementary particles and their interaction.

1.1 The Standard Model

We now know that there are four fundamental forces in nature: the strong, electromagnetic, weak and gravitational forces. The electromagnetic and weak interactions have been found to emerge from the unified electroweak interaction [1, 2, 3]. We have been able to formulate a quantum theory of elementary particles based on the strong and electroweak interactions. These interactions arise from the interchange of the massless photon for the electromagnetic interaction, massive W and Z bosons for the weak interaction, and the massless gluon for the strong interaction.

Our understanding indicates that all forces may be incorporated into a unified framework [5]. But our picture of observed particles is incomplete. It needs an important ingredient, related to the origin of mass and the breaking of the symmetry governing the electroweak interaction. The favourite candidate for this ingredient is the Higgs field, a scalar field that spreads out in all space. Its field quanta is the Higgs particle. The Higgs boson is the last missing

particle of the theory explaining the electroweak and the strong interactions: the Standard Model (SM) [6]. The SM is a very successful theory which has described phenomena of these interactions with high precision [8].

1.2 Beyond the Standard Model

If a Higgs boson is found with characteristics predicted by the SM, the SM cannot yet be the ultimate theory. A particular shortcoming of the SM is its instability against the huge hierarchy of vastly different scales relevant to particle physics. The hierarchy problem can be stated as: Why is the Higgs boson so much lighter than the Planck mass? The two known scales are the electroweak scale at a few hundred GeV and the Planck scale at about 10^{19} GeV, where the strength of gravity and the other interactions are predicted to become comparable [11]. The experimental evidence shows that neutrinos have a very small mass, $m_\nu < 0.28$ eV, which points towards the physics beyond SM [12, 13]. We also know that ordinary matter (quarks and leptons), makes up a small fraction of the matter density of the Universe [12]. But the SM does not give any explanation for the missing dark matter and dark energy.

A very attractive possibility for physics beyond the SM is supersymmetry (SUSY) [16]. In SUSY, every SM particle has a 'superpartner' which has spin one half unit different. This stabilises the hierarchy between the electroweak and Planck scales, if SUSY exits close to the TeV energy scale. Figure 1.1 shows the corrections to the Higgs boson mass, m_H, from a top quark loop. The presence of superpartner of the top quark, the stop, reduces the size of the quantum corrections as the fermionic and bosonic Higgs interactions automatically cancel, thus solving the hierarchy problem.

Supersymmetric theories allow the unification of the strong, electromagnetic and weak interactions at a scale of about 10^{16} GeV, as shown in figure 1.2. The possible scale of grand unification is the same as the one at which neutrinos gain mass [14].

The discovery of new physics, such as SUSY, can be studied at experiments with colliding beams. These experiments will play a crucial role in the understanding of the physics beyond SM. The discovery of new particles needs two things: the highest possible energy and the highest possible precision of

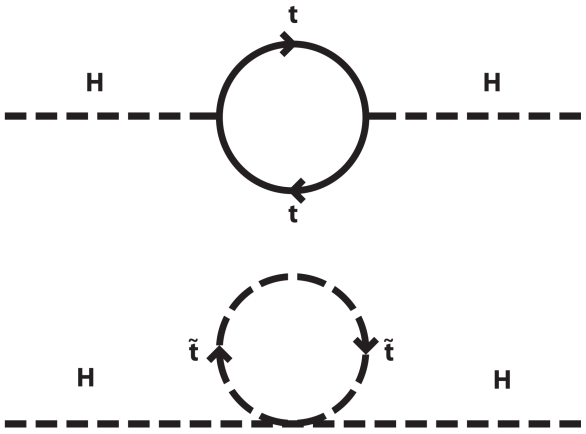

Figure 1.1: Top and stop loop corrections to Higgs boson mass. Top: Feynman diagram for top-quark (t) corrections to the Higgs boson mass. This diagram is quadratically divergent, leading to corrections proportional to $|\lambda_t|^2 \Lambda_{UV}^2$, where λ_t is the top quark - Higgs boson Yukawa coupling and Λ_{UV} is Planck scale. Bottom: Feynman diagram for stop corrections ($\tilde{t}$) to the Higgs boson mass. This leads to corrections proportional to $-\lambda_{\tilde{t}} \Lambda_{UV}^2$ where $\lambda_{\tilde{t}}$ is the stop coupling to the Higgs. These two corrections cancel if $|\lambda_t|^2 = \lambda_{\tilde{t}}$.

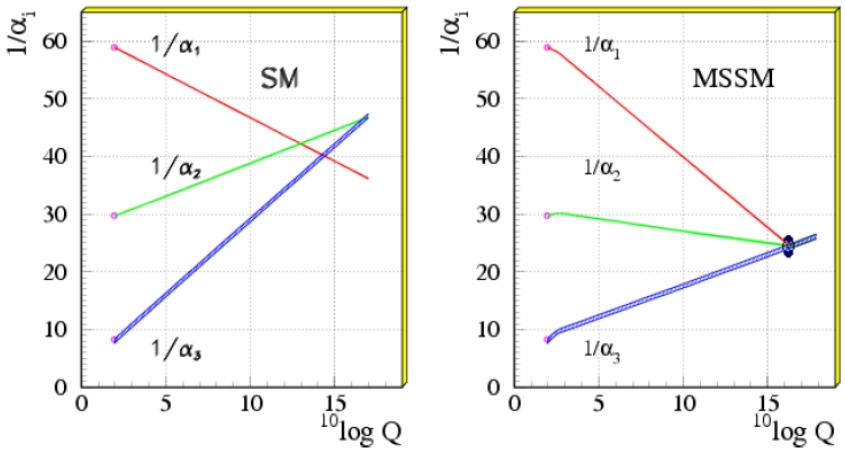

Figure 1.2: Left: $1/\alpha$, the inverse of couplings in SM. Right: Couplings in the Minimal Supersymmetric Standard Model (MSSM) [7].

the measurements. These two requirements cannot be obtained with one single collider. Therefore we need both a hadron collider to make new discoveries and a lepton collider to make the precision measurements of the physics discovered at the hadron collider.

Advances in accelerator technology has made possible the next generation of hadron and lepton colliders. The Large Hadron Collider (LHC) at CERN is currently running and will be able to discover new particles [17]. The International Linear Collider (ILC) is proposed as the next lepton collider [25].

1.3 Complementarity of LHC and ILC

In the next few years, data from the CERN's Large Hadron Collider (LHC) will have a direct look at the TeV physics. No one knows what will be found at the LHC, but the discovery potential of the LHC experiments is well studied [17, 18, 19, 20]. For all of the outcomes from LHC, a future linear collider such as the International Linear Collider (ILC) will be essential to move forward on our understanding of Higgs boson physics [15]. The ILC is designed to collide electrons and positrons with a maximum center-of-mass energy of $\sqrt{s} = 500$ GeV, with a possible upgrade to 1 TeV. The discoveries at LHC and ILC will hopefully explain the breaking of electroweak symmetry and thus the origin of the masses of particles, and then it is most likely that we will be able to find the physics which is responsible for stabilising the hierarchy problem, so the unification of all forces.

This thesis is concerned with the search for the SM Higgs boson. The measurements at ILC of the Higgs boson branching ratios and the top quark - Higgs boson Yukawa coupling are the main analyses of this thesis. An overview of the Standard Model and the Higgs mechanism is reproduced in chapter 2. Chapter 3 contains a description of the ILC and its proposed detector concepts. Simulation and reconstruction tools used in this thesis are provided in chapter 4. The Higgs branching ratio and top Higgs Yukawa coupling analyses are presented in chapters 5 and 6, respectively. The work described in this thesis is summarised in chapter 7 and an outlook is given.

Chapter 2

Theoretical Motivation

The 'Standard Model' of particle physics is the result of the immense experimental and inspired theoretical effort, spanning more than fifty years. The beauty and basic simplicity of the theory lies in explaining the fundamental constituents that made up the Universe and their interactions with one another. However, one aspect of the theory is unconfirmed, that is how the fundamental constituents acquire their masses. This chapter gives an introduction to the Standard Model and the Higgs mechanism which allow particles to acquire a mass within the theory [21, 22].

2.1 The Standard Model

The Standard Model explains what the world is made of and what holds it together. It is a simple and comprehensive theory that explains the hundred of particles and complex interactions with only 6 quarks: bottom (b), charm (c), top (t), strange (s), up (u) and down (d), 6 leptons: electron (e), muon (μ) tau (τ) and their neutrinos (ν_e, ν_μ, ν_τ), force carrier particles: photon (γ), gluon and W and Z bosons and one Higgs boson (H) as shown in Table 2.1 and figure 2.1.

The quarks and leptons are spin $\frac{1}{2}$ fermions but distinct on the basis of their interactions: quarks carry one of three colour charges associated with the strong interaction whereas leptons do not. Table 2.1 shows the fermions arranged in three generations of progressively more massive doublets. There exists an anti-particle for each particle with identical mass but opposite additive quantum numbers. The first generation is the only constituent of ordinary matter. Second and

Figure 2.1: Recipe for the Standard Model.

third generation particles are created at high energy, for example in particle accelerators. Once these particles are created, they decay quickly into the first generation particles.

The Standard Model describes three types of interaction out of four that are present in the Universe: the electromagnetic interaction, weak and the strong interactions, as shown in Table 2.2. The massless photon, massive $W^{\pm}$ and Z^0 bosons and eight massless gluons are the mediating particles for the three interactions respectively. The Standard Model gives precise values for the allowed couplings amongst the fermions and bosons. The gravitational force is too weak to have any significant effect at the level of these forces.

2.2 The Gauge Principle

In the Standard Model the strong and electroweak interactions are implemented as gauge theories, which are spontaneously broken via the Higgs mechanism [24][6]. A gauge theory requires an invariance of the system under a set of local transformations. Noether's theorem provides an important result related to the invariance of the theory under some transformations, that there exist one or more conserved quantities associated to these transformations [31].

Table 2.1: Six of the particles in the Standard Model are quarks (shown in purple). Each of the first three columns forms a generation of matter.

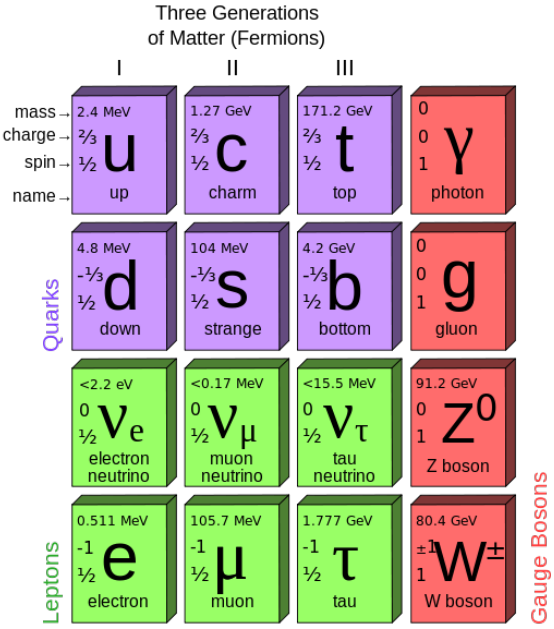

Table 2.2: Forces, mediating particles and range.

Force	Mediating particle	Range
Electromagetic	γ	infinite
Weak	$W^{\pm}$ and Z^0	$\sim 10^{-18}$ m
Strong	8 types of gluon	$\sim 10^{-15}$ m
Gravitational	Graviton	infinite

Gauge Principle for the Electromagnetic Force

In electromagnetism, the existence and some of the properties of the gauge field - the photon - follow from the principle of invariance under local gauge transformations of the $U(1)$ group. Let us consider the Dirac free particle Lagrangian, $\mathcal{L}$, for a particle of mass, m:

$$\mathcal{L} = \bar{\psi}\left(i\gamma^{\mu}\partial_{\mu} - m\right)\psi. \tag{2.1}$$

Where ψ is the fermionic spinor field, $\bar{\psi} = \psi^{\dagger}\gamma^{0}$, and γ^{μ} are the Dirac matrices. Equation 2.1 is not invariant under the local gauge transformation, $\psi \rightarrow \psi' = \exp(-i\alpha(x))\psi$, where $\alpha(x)$ depends on the space-time coordinate, x. However, if we introduce the gauge field A_{μ} through the minimal coupling $D_{\mu} \equiv \partial_{\mu} + ieA_{\mu}$ thus requiring $A_{\mu} \rightarrow A'_{\mu} = A_{\mu} + \frac{1}{e}\partial_{\mu}\alpha(x)$, the resulting Lagrangian is:

$$\mathcal{L} = \bar{\psi}\left(i\gamma^{\mu}\partial_{\mu} - m\right)\psi - \frac{1}{4}F_{\mu\nu}^{2} + e\,\bar{\psi}\gamma^{\mu}A_{\mu}\psi \tag{2.2}$$

where e is the coupling between the fermion and the photon (essentially the electron charge) and $F_{\mu\nu} \equiv \partial_{\mu}A_{\nu} - \partial_{\nu}A_{\mu}$. $F_{\mu\nu}$ and $\mathcal{L}$ are now invariant under the local gauge transformation. There is no allowed mass term for the photon in the Lagrangian, therefore the photon is required to be massless. The effect of imposing local gauge invariance gives an interacting system.

Gauge Principle for the Standard Model

The Standard Model is locally gauge invariant under $SU(2)_L \otimes U(1) \otimes SU(3)$ [1, 2, 3]. The strong force is described by quantum chromodynamics (QCD) and is based on the $SU(3)$ symmetry group with eight massless gluons corresponding to the eight generators of the group. The $SU(2)_L$ and $U(1)$ groups correspond to the weak isospin and hypercharge respectively. The electroweak sector of the theory requires four gauge bosons: a triplet (W^1, W^2, W^3) associated to the generators of $SU(2)_L$ and a neutral field (B) related to $U(1)$. As will be shown in equations 2.12 - 2.14, the charged weak bosons appear as a linear combination of W^1 and W^2, while the photon and a neutral weak boson Z^0 are given by mixtures of W^3 and B. The theory does not have mass terms for $W^{\pm}$ and Z^0. The idea of spontaneous symmetry breaking of $SU(2)_L \otimes U(1) \rightarrow U(1)$ and Higgs mechanism

is to give mass to the weak bosons as described in the next section.

2.3 Spontaneous Symmetry Breaking and the Higgs Mechanism

Exact symmetries give rise, generally, to exact conservation laws. In this case the Lagrangian and the vacuum are invariant under the gauge transformation. There are some conservation laws which do not follow this rule. Quark Flavour is one example. There is another situation when a system has Lagrangian invariant but a vacuum is non-invariant. A classic example of the situation is provided by a ferromagnet where the Lagrangian describing spin-spin interaction is invariant under tridimensional rotations but the vacuum is non-invariant below a critical temperature where the ferromagnetic phase occurs.

2.3.1 The Goldstone Mechanism

The Goldstone theorem examines the spontaneous breaking of a continuous global symmetry which is not the symmetry of the vacuum [21, 32]. To explain the Goldstone theorem let us consider a complex scalar field $\Phi = (\phi_1 + i\phi_2)/\sqrt{2}$. The Lagrangian density for the field Φ is:

$$\mathcal{L} = \partial_\mu \Phi^\dagger \partial^\mu \Phi - m^2 \Phi^\dagger \Phi \tag{2.3}$$

In this case, as Φ is independent of space and time, the only contribution to the energy is $m^2\Phi^\dagger\Phi$. As m^2 is positive so the minimum will occur when $\phi_1 = \phi_2 = 0$. Thus $\Phi = 0$ corresponds to the vacuum state. If the Lagrangian density is slightly different by changing the sign in front of m^2, the vacuum state is unstable. Stability can be restored by introducing a term $(1/2m^2\phi_0^2)(\Phi^\dagger\Phi)^2$ where ϕ_0^2 is a real parameter. The Lagrangian can be written as:

$$\mathcal{L} = \partial_\mu \Phi^\dagger \partial^\mu \Phi - V(\Phi^\dagger \Phi) \tag{2.4}$$

where:

$$V(\Phi^\dagger \Phi) = \frac{m^2}{2\phi_0^2}[\Phi^\dagger \Phi - \phi_0^2]^2 \tag{2.5}$$

.

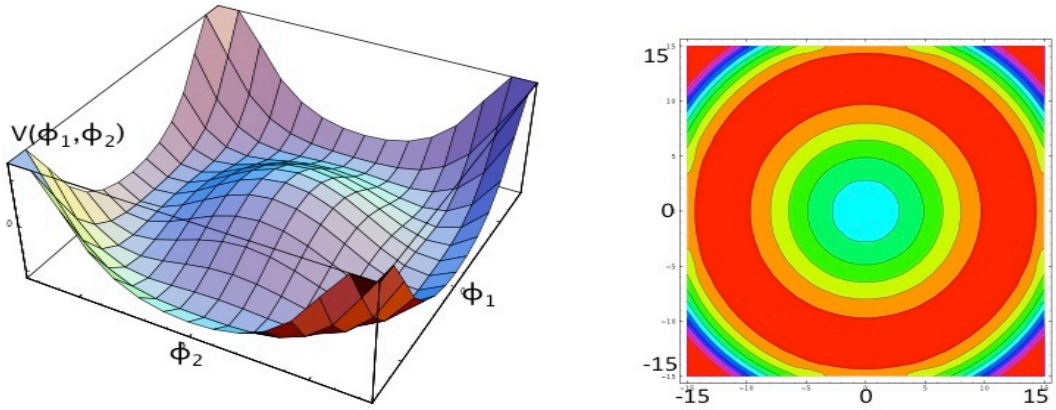

(a) (b)

Figure 2.2: Scalar potential for $V(\phi_1, \phi_2)$ (a) and its contour plot (b) taken from [32].

The minimum field energy is now obtained with Φ constant independent of space and time, but such that $\Phi^\dagger\Phi = |\Phi|^2 = \phi_0^2$. Such a field is not unique but is defined by a point on the circle $|\Phi| = \phi_0$ in the state space (ϕ_1, ϕ_2), so that the number of possible vacuum states are infinite.

The Lagrangian density has a global $U(1)$ symmetry: $\Phi \rightarrow \Phi' = e^{ix}\Phi$. As we see from the contour plot in figure 2.2, the vacua are also invariant under this global $U(1)$ transformation: this transformation rotates the state round a circle $|\Phi|$ = constant in the state space (ϕ_1, ϕ_2). If we pick out the particular direction in (ϕ_1, ϕ_2) space for which Φ is real and take the vacuum state to be $(\phi_0, 0)$, we break the $U(1)$ symmetry.

Expanding Φ around this ground state $(\phi_1, 0)$, we get a Lagrangian shifting $\Phi \rightarrow \Phi' \equiv (1\sqrt{2})(\chi + i\psi) + \phi_0$:

$$\mathcal{L} = \frac{1}{2}\partial_\mu\chi\partial^\mu\chi + \partial_\mu\psi\partial^\mu\psi - \frac{m^2}{2\phi_0^2}\left[\sqrt{2}\phi_0\chi + \chi^2/2 + \psi^2/2\right]^2 \tag{2.6}$$

where χ and ψ are scalars. Here we can write $\mathcal{L} = \mathcal{L}_{free} + \mathcal{L}_{int}$, where the $\mathcal{L}_{free}$ contains all the terms which are quadratic in the fields and $\mathcal{L}_{int}$ has all contributions from the interaction terms. This is the Goldstone theorem which states that when a global symmetry is spontaneously broken, the theory contains one massless scalar particle for each broken generator of the original symmetry.

2.3.2 Higgs Mechanism

The Goldstone theorem implies the existence of a massless scalar particle but this particle is never seen experimentally. The Higgs Mechanism provides a way out by giving mass to the gauge boson. This is accomplished by constructing a Lagrangian density which is invariant under a local $U(1)$ gauge transformation: $\Phi \rightarrow \Phi' = e^{-iq\theta}\Phi$, where $\theta = \theta(x)$ is space time dependent. Consequently, we introduce a massless gauge field A_μ. The Lagrangian density is:

$$\mathcal{L} = \left[(\partial_\mu - iqA_\mu)\Phi^\dagger\right]\left[(\partial^\mu + iqA^\mu)\Phi\right] - \frac{1}{4}F_{\mu\nu}F^{\mu\nu} - V(\Phi^\dagger\Phi) \tag{2.7}$$

with V as defined in equation 2.5 and $F_{\mu\nu}$ as defined above. $\mathcal{L}$ is invariant under the local gauge transformation:

$$\Phi(x) \rightarrow \Phi'(x) = e^{-iq\theta}\Phi(x) \qquad A_\mu(x) \rightarrow A'_\mu(x) = A_\mu(x) + \partial_\mu\theta(x). \tag{2.8}$$

A minimum field energy is obtained when the fields A_μ vanish and Φ is constant, defined by the point on the circle $|\Phi| = \phi_0$. Any gauge transformation on this field is also a minimum. There are an infinite number of vacuum states. We can always choose $\theta(x)$ so that $\Phi'(x)$ is real for a given $\Phi(x)$. Consequently, symmetry is broken as we are no longer free to make further gauge transformations.

Expanding $\Phi(x)$ around $\phi_0(x)$, we get Lagrangian:

$$\begin{aligned}\mathcal{L} \;=\; & \left[(\partial_\mu - iqA_\mu)(\phi_0 + h(x)/\sqrt{2})\right]\left[(\partial^\mu + iqA^\mu)(\phi_0 + h(x)/\sqrt{2})\right] \\ & -\frac{1}{4}F_{\mu\nu}F^{\mu\nu} - \frac{m^2}{2\phi_0^2}[\Phi^\dagger\Phi - \phi_0^2]^2\end{aligned} \tag{2.9}$$

where we have made the substitution $\Phi'(x) = \phi_0 + h(x)/\sqrt{2}$, where $h(x)$ is a real function.

Separating Lagrangian again into free and interaction parts: $\mathcal{L} = \mathcal{L}_{free} + \mathcal{L}_{int}$:

$$\mathcal{L}_{free} = \frac{1}{2}\partial_\mu h\,\partial^\mu h - m^2h^2 - \frac{1}{4}F_{\mu\nu}F^{\mu\nu} + q^2\phi_0^2A_\mu A^\mu, \tag{2.10}$$

$$\mathcal{L}_{int} = q^2A_\mu A^\mu\left(\sqrt{2}\phi_0 h + \frac{1}{2}h^2\right) - \frac{m^2h^2}{2\phi_0^2}\left(\sqrt{2}\phi_0 h + \frac{1}{2}h^2\right) \tag{2.11}$$

Before symmetry breaking, we had Φ, a complex scalar field and a massless vector field with two polarisation states. After breaking the symmetry, $\mathcal{L}_{free}$ has one single scalar field corresponding to a spinless boson with mass $\sqrt{2}m$ and a vector field A_μ corresponding to a vector boson of mass $\sqrt{2}q\phi_0$ with three polarisation states.

Therefore we can interpret this as the Higgs field $h(x)$, resulting in a physical scalar boson particle with the mass $\sqrt{2}m$. In the case of the electroweak Lagrangian, the $SU(2)$ group has three generators which correspond to the gauge bosons $(W^1_\mu, W^2_\mu, W^3_\mu)$ and a coupling denoted by g. The $U(1)$ group has one boson and a coupling g'. The relative strength of these interactions is determined according to $g' = g\tan\theta_W$, where θ_W is defined to be the weak mixing angle.

The linear combination of gauge fields give the physical mediators:

$$W^\pm \equiv (W^1_\mu \mp iW^2_\mu/\sqrt{2}) \tag{2.12}$$

$$Z_\mu \equiv \cos\theta_W W^3_\mu - \sin\theta_W B_\mu \tag{2.13}$$

$$A_\mu \equiv \cos\theta_W B_\mu - \sin\theta_W W^3_\mu \tag{2.14}$$

of which only Z and W acquire mass through the Higgs mechanism.

In order to break the $SU(2)_L \otimes U(1)_Y$ symmetry we extend Φ to be doublet of complex fields, providing four extra degrees of freedom:

$$\Phi = \begin{pmatrix} \phi_+ \\ \phi_0 \end{pmatrix} = \sqrt{\frac{1}{2}} \begin{pmatrix} \phi_1 + i\phi_2 \\ \phi_3 + i\phi_4 \end{pmatrix} \tag{2.15}$$

During spontaneous symmetry breaking, three of the extra degree of freedom are given to the $W^\pm$ and Z bosons allowing them to become massive and the other corresponds, as before, to a massive scalar Higgs boson. The photon remains massless as the electroweak Lagrangian remains invariant under local Abelian transformation.

2.3.3 Higgs Boson Coupling to Fermions

The Lagrangian does not have an explicit term for the fermions mass as in the weak interaction helicity $+\frac{1}{2}$ (right-handed) and helicity $-\frac{1}{2}$ (left-handed) are treated separately. However, there is one possibility in which left and right handed fermions interact with each other and Higgs field, Φ. These interactions are known

as Yukawa interactions and gives terms in Lagrangian:

$$\mathcal{L}_{Yukawa} = g(\bar{\psi}_L \Phi \psi_R + \bar{\psi}_R \Phi \psi_L) \tag{2.16}$$

where g is the coupling constant of the interaction.
The Yukawa coupling for electrons in unitary gauge is:

$$g_e = g\frac{m_e}{\sqrt{2}M_W} \tag{2.17}$$

We can see that the coupling is proportional to the electron mass. In a similar way the quarks also acquire mass and coupling which is proportional to their masses. Hence, each of the quark and charged lepton has its unique coupling defined by its mass.

$$g_{fHf} = \frac{m_f}{v} \tag{2.18}$$

where $v = (\sqrt{2}G_F)^{-1/2} \equiv 246$ GeV.

The Yukawa couplings are free parameters of the Standard Model and they are determined to a certain accuracy from the measured fermion masses. Both analysis in this thesis investigate the coupling of Higgs boson with quarks. Analysis in chapter 5 probes the branching fraction of Higgs boson to $b\bar{b}$, $c\bar{c}$ and gluons. Second analysis of this thesis is focused on studying how well the top Higgs Yukawa coupling can be measured at a specific detector model of a linear collider.

2.4 Higgs Boson Mass Constraints

The Higgs couplings to fermions and gauge bosons are related to the masses of these particles and the only free parameter of the model is the mass of the Higgs boson itself; there are, however, both experimental and theoretical constraints on this fundamental parameter.

Experimental bounds The available direct information on the Higgs mass (M_H) is the lower limit $M_H \gtrsim 114.4$ GeV established at LEP [27][1]. The high accuracy of the electroweak data measured at LEP, SLC and Tevatron provides

[1]We are using natural units, $c = \hbar = 1$

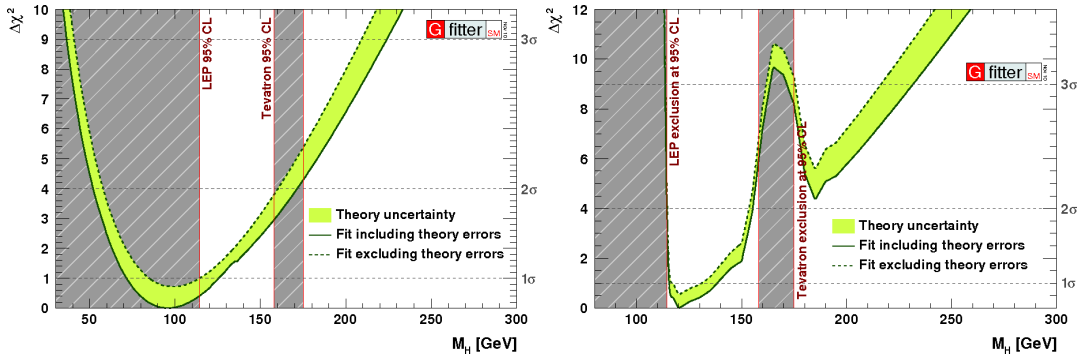

Figure 2.3: Left: χ^2 fit to the SM electroweak precision data - excluding direct results on Higgs searches - as a function of the Higgs boson mass, M_H. Right: As left, but this time including direct results on Higgs searches. Both taken from reference [33]. The most probable M_H is $120.6^{+17.9}_{-5.2}$ GeV.

an indirect sensitivity to M_H: the Higgs boson contributes logarithmically, $\propto \log(M_H/M_W)$, to the radiative corrections to the W/Z boson propagators. A recent analysis, which uses the updated value of the top quark mass [28] yields the value 85±25 GeV, with upper limit of $M_H \lesssim 165$ GeV. Direct searches by CDF and D0 exclude a region at high mass between $156 < M_H < 177$ GeV [29].

The left-hand side of figure 2.3 shows the standard fit to the electroweak data. The solid (dashed) line gives the results when including (ignoring) theoretical errors. If the Higgs boson turns out to be significantly heavier than 200 GeV, there should be an additional new ingredient that is relevant at the Electroweak symmetry breaking scale which should be observed at the next round of experiments.

Theoretical bounds From the theoretical side, interesting constraints can be derived from assumptions on the energy range within which the SM is valid before perturbation theory breaks down and new phenomena would emerge. For instance, if the Higgs mass were larger than $\sim$ 1 TeV, the W and Z bosons would interact very strongly with each other which would violate the unitarity in their scattering at high energies. Imposing the unitarity requirement in the high-energy scattering of gauge bosons leads to the bound $M_H \lesssim 700$ GeV [23]. If the Higgs boson were too heavy, unitarity would be violated in these processes at energies above $\sqrt{s} \gtrsim 1.2$ TeV and new phenomena should appear to restore it.

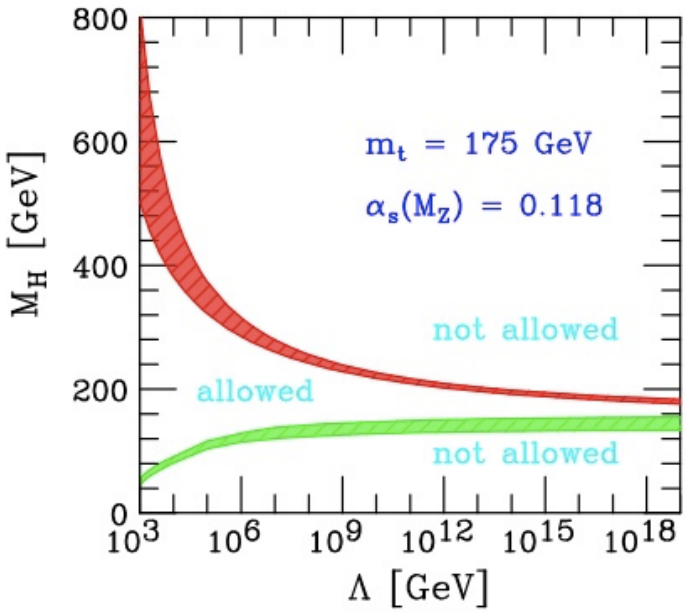

Figure 2.4: Theoretical upper and lower bounds on mass of Higgs, M_H [42].

Requiring the SM to be extended to the GUT scale and including the effects of top quark loops on the running coupling, the Higgs boson mass should lie in the range 130 GeV$\lesssim M_H \lesssim$ 180 GeV; see figure 2.4.

In fact in any model beyond the SM in which the theory is required to be weakly interacting up to the GUT or Planck scales the Higgs boson should be lighter than $M_H \lesssim 200$ GeV. Such a Higgs particle can be produced at the ILC already for the center of mass energies of $\sqrt{s} \sim 300$ GeV. However, to cover the entire Higgs mass range in the SM, $M_H \lesssim 700$ GeV, center of mass energies close to $\sqrt{s} = 1$ TeV would be required.

2.5 Higgs Production and Decay

In the SM, the profile of the Higgs particle is uniquely determined once its mass M_H is fixed [23, 42]. The decay width, the branching ratios and the production cross sections are given by the strength of the Yukawa couplings to fermions (figure 2.5 and gauge bosons, the scale of which is set by the masses of these particles.

$$g_{fHf} \propto m_f \tag{2.19}$$

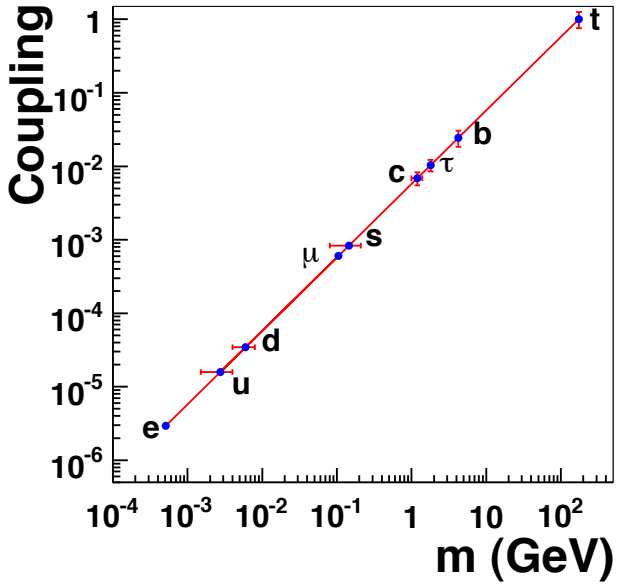

Figure 2.5: Couplings of the Higgs boson to the fermions as a function of their masses. The error bars show the uncertainty in the quark mass measurement.

The trilinear and quartic Higgs self-couplings are also uniquely fixed in terms of the Higgs boson mass, for example trilinear coupling is:

$$g_{HHH} = \frac{m_H^2}{2v} \tag{2.20}$$

The Standard Model Higgs boson decays are dominated by the heaviest, kinematically accessible particles. Thus of $m_H \leq 135$ GeV, the largest branching ratio is $H \to b\bar{b}$.

2.5.1 Decay Channels

Low Mass Higgs

In the "low Higgs mass" range, $M_H \lesssim 140$ GeV, the Higgs boson decays into a large variety of channels. As shown in figure 2.7 the main decay mode is the decay into $b\bar{b}$ pairs with branching ratio of $O(80\%)$, followed by the decays into $c\bar{c}$ and $\tau^+\tau^-$ pairs with fractions of $O(5\%)$. Also of significance, the top-loop mediated Higgs decays into gluons which for M_H around 120 GeV occurs at the

level of $\sim O(6)\%$. The top and W-loop mediated $\gamma\gamma$ and $Z\gamma$ decay modes are very rare with the branching fractions being of $O(10^{-3})$. However, these decays are, together with $H \to gg$, theoretically interesting being sensitive to new heavy states such as SUSY particles.

High Mass Higgs

In the "high Higgs mass" range, $M_H \gtrsim 140$ GeV, the Higgs bosons decays mostly into WW^* and ZZ^* pairs, with one of the gauge bosons being virtual if energy is below the threshold. Above the ZZ threshold, the Higgs boson decays almost exclusively into these channels with a branching ratio of 2/3 for $H \to WW$ and 1/3 for $H \to ZZ$ decays. The opening of the $t\bar{t}$ channel for $M_H \gtrsim 350$ GeV does not alter this pattern significantly as $BR(M_H \to t\bar{t})$ does not exceed the level of 10-15% when kinematically accessible. In the low mass range, the Higgs boson is very narrow $\Gamma < 10$ MeV, but the width becomes rapidly wider for masses larger than 140 GeV, reaching $\Gamma \sim 1$ GeV at the ZZ threshold as shown in figure 2.6. For large masses, $M_H \gtrsim 500$ GeV, the Higgs becomes very broad since its total width is comparable to its mass, and it is hard to consider it as a resonance.

In our study of branching ratios, Higgs bosons were produced with M_H of 120 GeV. At this mass, Higgs decays 68% into $b\bar{b}$, 3% into $c\bar{c}$ and 6% into both $\tau^+\tau^-$ and gg.

2.5.2 Higgs Production at Lepton Colliders

In this section the main production process of Higgs at the lepton collider such as ILC are presented. First one is the Higgs-strahlung process including $e^+e^- \to ZH$ which is studied in this thesis for measurement of the Higgs branching ratio. Second process is the associated production with top pair, as studied in this thesis for the top Higgs Yukawa coupling. The production rates for all these processes are shown in figure 2.8 at energies $\sqrt{s} = 500$ GeV as a function of M_H.

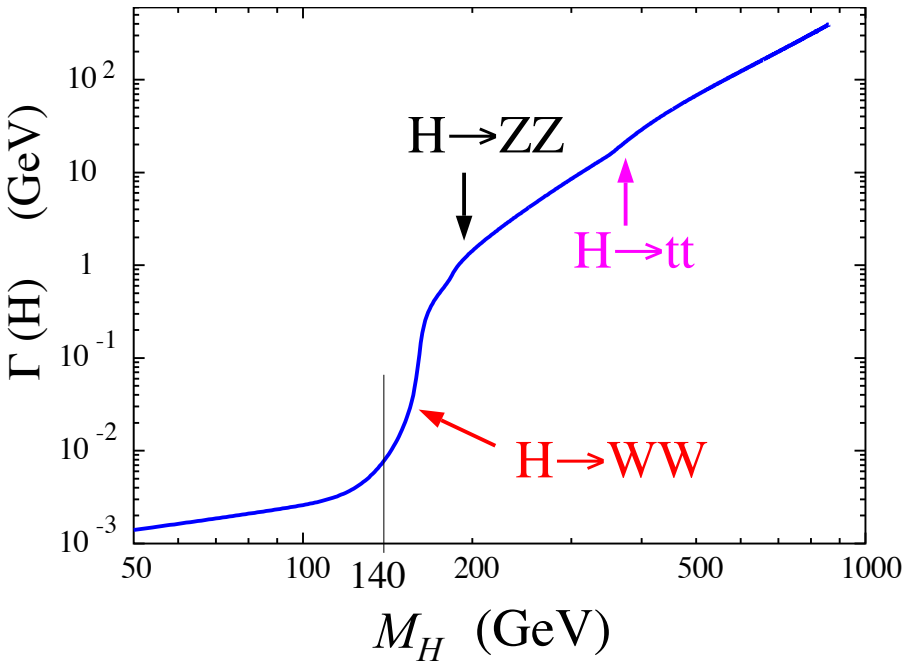

Figure 2.6: The total decay width of the SM Higgs boson as function of its mass [37].

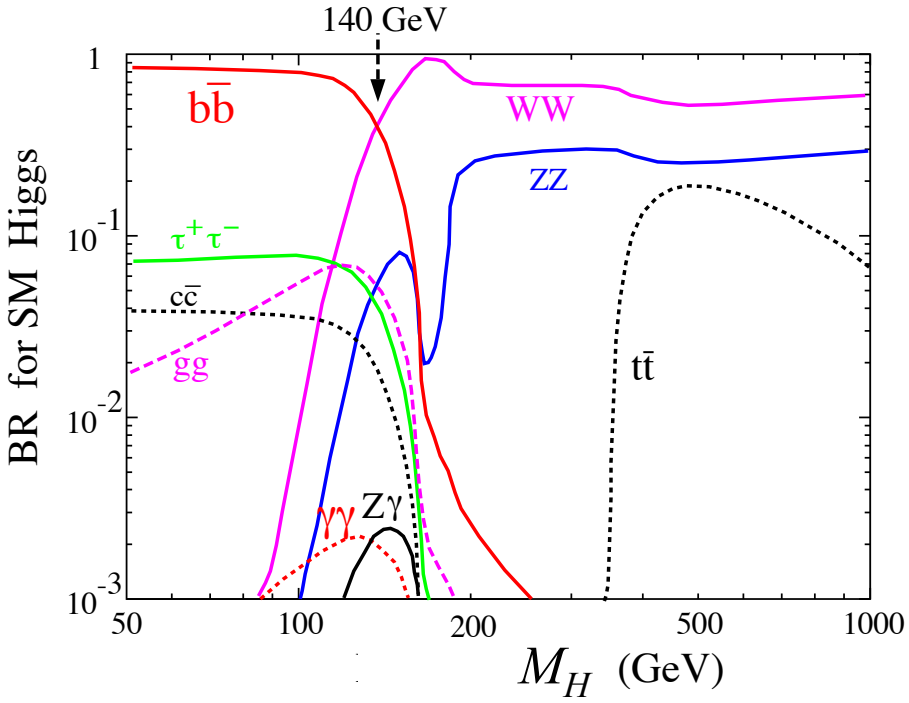

Figure 2.7: The branching ratios of the SM Higgs boson as function of its mass [37].

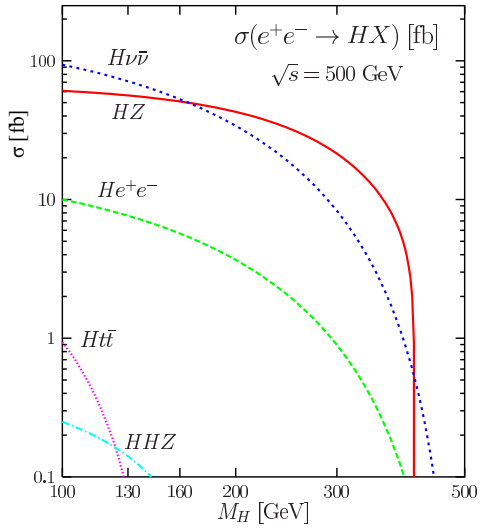

Figure 2.8: Cross section for different production mechanism of Higgs at $\sqrt{s} = 500$ GeV [24].

Higgs-Strahlung mechanism

In e^+e^- collisions, the main production mechanisms for the SM Higgs particle are the Higgs-strahlung [42] and WW fusion [30] processes, as shown in figure 2.9:

$$\begin{aligned} e^+e^- &\to ZH \to f\bar{f}H \\ e^+e^- &\to \bar{\nu}_e\nu_e H \end{aligned}$$

where f are the fermion decay products of the Z boson such as e, μ etc.

The final state $H\nu\bar{\nu}$ is generated in both the fusion and Higgs-strahlung processes. The cross section for Higgs-strahlung scales as $\frac{1}{s}$ and therefore dominates at low energies, while the WW fusion mechanism rises like $\log s/M_H^2$ and becomes more important at high energies. At $\sqrt{s} \sim 500$ GeV, the two processes have approximately the same cross sections, O (50 fb) for the interesting Higgs mass range 115 GeV $\lesssim M_H \lesssim$ 200 GeV. For the planned ILC integrated luminosity of ~ 500 fb^{-1}, approximately 30,000 and 40,000 events can be collected in, respectively, the $e^+e^- \to ZH$ and $e^+e^- \to \nu\bar{\nu}H$ channels for $M_H \sim 120$ GeV. This sample is more than enough to observe the Higgs particle at the ILC and to study its properties in detail.

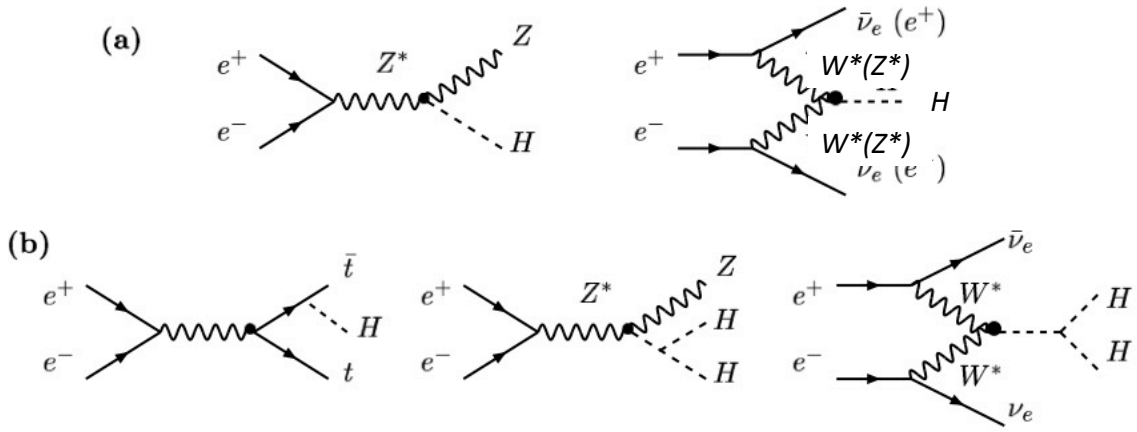

Figure 2.9: Feynman diagrams for the dominant (a) and sub-leading (b) Higgs production mechanisms at ILC

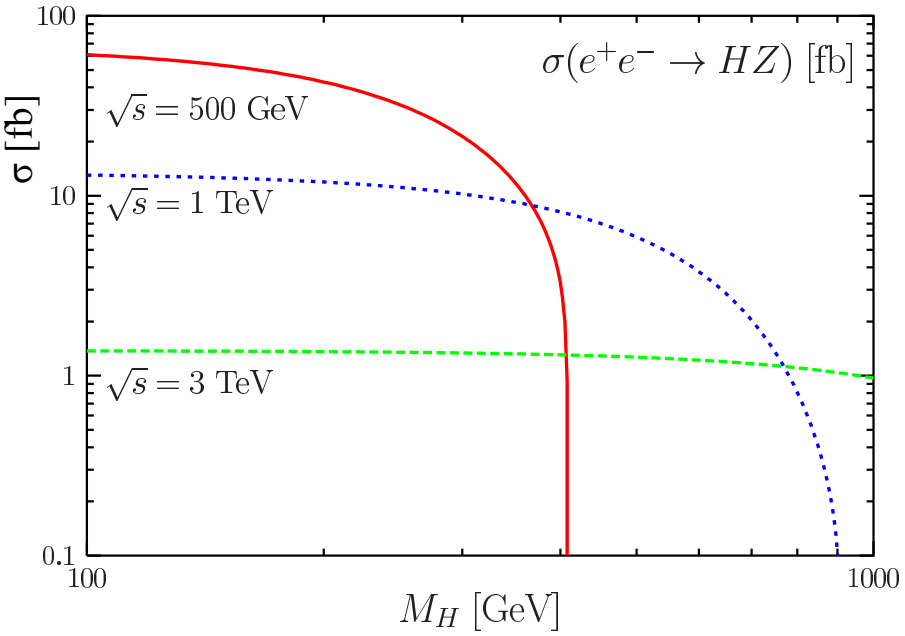

Figure 2.10: Production cross section for Higgs-strahlung mechanism of Higgs at $\sqrt{s} = 0.5$, 1 and 3 TeV [24].

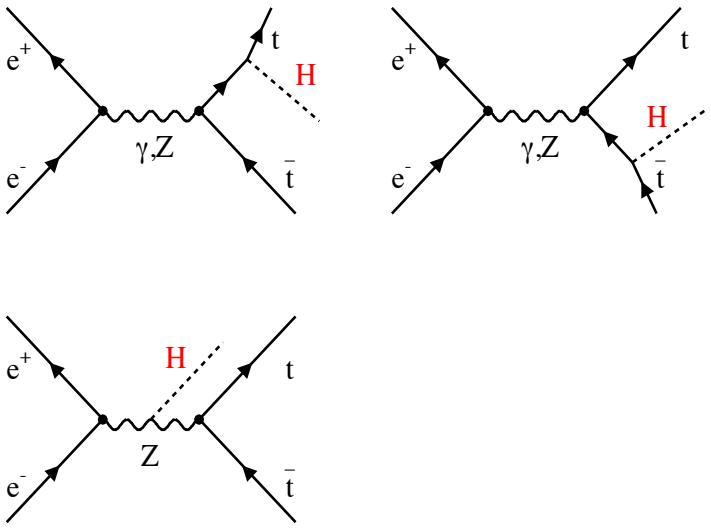

Figure 2.11: Feynman diagrams for Higgs production in association with $t\bar{t}$ pair.

Associated production with top quark pair

The associated production of a Higgs boson with a pair of top quarks [24] in the SM has two Feynman diagrams as shown in figure 2.11. In one diagram the Higgs boson is radiated off the $t\bar{t}$ pair, and the other diagram is where Z and Higgs are produced in association with each other. The associated production with top quarks has a small cross section at $\sqrt{s} = 500$ GeV due to phase space suppression but, at $\sqrt{s} = 800$ GeV, it can reach the level of a few femtobarns. In figure 2.12 the dashed line shows cross section when the contributions are only from the Higgs radiated off the top quark. The additional contributions from Higgs boson emitted by the Z line are small for low $\sqrt{s}$ as shown in the figure 2.12. The $t\bar{t}H$ final state is generated almost exclusively through Higgs-strahlung off top quarks in that case. The electroweak and QCD corrections are known and are moderate, except near the production threshold where large coulombic corrections occur and double the production rate.

Next-to-leading logarithmic (NLL) QCD corrections are determined which enhanced the tree level predictions by about a factor of two. These are important for the determination of the top Yukawa coupling [24]. In the top Higgs Yukawa coupling analysis presented here, the event generator, WIZHARD, makes use of

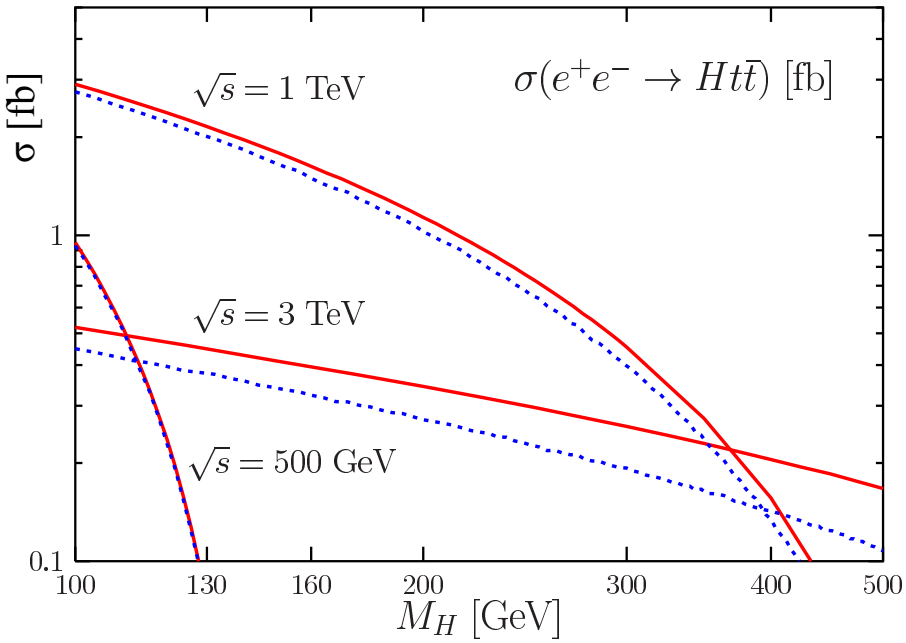

Figure 2.12: The production cross section for associated Higgs boson with $t\bar{t}$ pair at $\sqrt{s}$ = 0.5, 1 and 3 TeV [24]. The dashed line shows the contributions when these are only from the Higgs radiated off the top quark.

the enhanced cross section of $t\bar{t}H$ due to these QCD corrections. The cross section is increased from 0.32 fb to 0.58 fb for $m_t = 175$ and $m_H = 120$ GeV at $\sqrt{s} =$ 500 GeV [26].

2.6 Problems of the Standard Model

In spite of the successful experimental confirmation of the Standard Model (SM), it does not give the full picture of nature [35]. It is rather a low energy effective theory of a more fundamental one. There are certain experimental and theoretical problems associated with the SM. The experimental evidence that neutrino has mass is one conflicting issue of the SM. The hierarchy problem is one issue arising in the theory as explained earlier in section 1.2. The SM leaves unexplained why the strong and the electroweak gauge structure is $SU(3) \otimes SU(2)_L \otimes U(1)$ with different gauge couplings and fermionic quantum numbers whose values are not predicted to the model.

There are a lot of efforts in solving the above mentioned problems [35, 36].

Theories that lie beyond SM include various extensions of the SM through introducing new symmetries such as Supersymmetry (SUSY) or Grand Unified Theory (GUT). There are some entirely novel explanations also exist such as extra dimensions and string theories.

2.7 Higgs Analysis at the International Linear Collider

In this chapter, an overview of the Higgs mechanism in the Standard model, constraints on the mass of Higgs, its different production and decay channels has been reproduced. Certain problems which SM is unable to solve, have been summarised. At last a brief introduction to the experimental high energy physics has been given. Once the Higgs boson is found it will be of great importance to explore all its fundamental properties. This can be done in great detail in the clean environment of e^+e^- linear colliders: the Higgs mass, its spin and parity quantum numbers and its couplings to fermions, massive and massless gauge bosons as well as its trilinear self-couplings can be measured with very high accuracies. The measurements would allow to probe in all its facets the electroweak symmetry breaking mechanism in the SM and probe small manifestations of new physics. In the following chapters, the Higgs-strahlung channel, and the associated production of Higgs with top quark, at the ILC is studied. The aim of the study is to measure the branching ratios of the Higgs to fermions and to test the top Yukawa coupling of the Higgs boson. In both analysis, we have used the mass of Higgs equals to 120 GeV. At 120 GeV the main decay mode of the Higgs is $b\bar{b}$ ($\sim 68\%$). Other significant fermionic decay channels are $c\bar{c}$ ($\sim 3\%$) and $\tau^+\tau^-$ ($\sim 6\%$). One of our study uses a center of mass energy of 250 GeV and the other one uses 500 GeV.

Chapter 3

International Linear Collider and International Large Detector

3.1 Particle Physics Experiments

Particle Physics experiments are conducted using accelerators and colliders. The high energy accelerator today has two kinds; one is synchrotron, where particles follow a high energy constant radius in a time varying magnetic field. The other one is a linear accelerator, where particles have linear motion. These accelerated bunches of particles, called beam, are collided in a detector [40, 41].

Parameters which govern the performance of the accelerators are the center of mass energy $\sqrt{s}$ and the luminosity (L). $\sqrt{s}$ is decided on the basis of what kind of measurements are needed to be done. For example if search of new phenomena is the goal, then as high as possible $\sqrt{s}$ is tried to be achieved. Luminosity and number of events produced are related with each other through:

$$N = \sigma \int L \, dt \tag{3.1}$$

where σ is the cross section of a given process. Luminosity itself is dependent on machine parameters:

$$L = \frac{N_{p1} N_{p2} f_b}{4\pi \sigma_x \sigma_y}, \tag{3.2}$$

with N_{p1} and N_{p2} are the number of particles in two colliding bunches, f_b is the rate of bunch crossings and σ_{xy} are transverse beam spot sizes at the interaction

point.

The detectors are placed at the collision points of the beams. Usually, they obey cylindrical symmetry, with the z-axis defined to be the direction of the beam. There are different subdetectors performing different purposes. A magnetic field is necessary to measure the charge and the momentum of the particle. A general overview of a detector and the purpose of various subdetectors is given below.

- **Impact parameter** of the trajectories of the charged particles with respect to the reconstructed interaction point is measured in the innermost subdetector. Hence help in the tagging of particles which live for relatively long time.

- **Momentum and charge measurement** is performed in the next detector layer. It is done by measuring the curvature of the trajectories of the charged particles in the magnetic field.

- **Particle Identification** is determined by combining information of energy loss per flight length and the momentum measurement.

- **Energy measurement** is done in the calorimeters. The two different kinds of calorimeters; electromagnetic (EM) and hadronic calorimeters (HAD) are used to measure the deposited energy of electron, positron, photon and heavier particles. Heavier particles deposit some of their energy in EM calorimeter if they are charged.

- **Muon Identification** is the aim of the outermost detector layer. Muons are the only interacting particles which are able to cross the calorimeters.

The ILC is a powerful engine in terms of its energy and luminosity, and as such it poses difficult experimental environments. The kinematically accessible range of center-of-mass energy, 0.5-1 TeV, allows new particle production, and their properties can be studied in great detail. New particles can be discovered even if their production cross sections are fairly low, and even if their decays are complicated. The challenges for ILC arise due to the requirements as described in the Reference Design Report, (RDR) [42]. The design of machine is motivated by the desire to investigate the details of electroweak symmetry breaking. At the ILC we know the initial momenta of particles so it allows the reconstruction of the final states with high efficiency and resolution. The center-of-mass energy

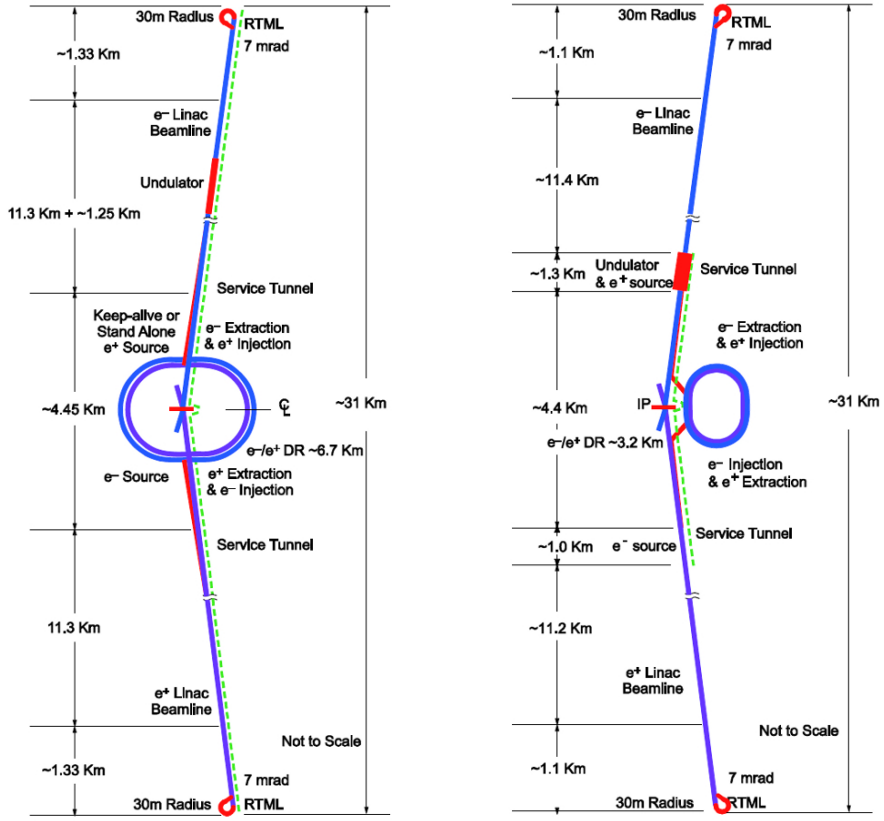

Figure 3.1: The proposed RDR configuration (left) and new configuration of the ILC (right) [39].

is tuneable allowing for precise mass and quantum number measurements from threshold scans. High-luminosity running at the Z-resonance and at the W^+W^- threshold, as well as e^-e^-, $\gamma\gamma$, and γe^- collision modes, offer additional flexibility. The jet energy resolution should be good to separate the hadronic decay of the W and Z decays. Therefore, a big challenge for ILD is to require a jet energy resolution of $\sigma_E/E \sim 3-4\%$ [50].

3.2 ILC Layout

The proposed layout of ILC will be given in the Technical Design Report to be published in 2012 but efforts are being put to decide different parameters of the accelerator [38] shown in figure 3.1. There are already some parameters for

Parameter	unit	RDR (nom.)	Proposed
E_{cm}	GeV	500	500
Rep. rate	Hz	5	5
Q_{bunch}	nC	3.2	3.2
Bunches/pulse		2625	1312
Main Linac			
RF pulse length	ms	1.6	KCS: 1.6 DRFS: 2.2
Beam current	mA	9	KCS: 6 DRFS: 4.5
Average beam power	MW	10.5	5.3
Damping Ring[1]			
Circumference	m	6476	3238
Avg. Current	mA	388	390
Damping time	ms	21	24
RF power	MW	3.97	1.76

Table 3.1: A comparison of the reduced parameter set with those from the RDR. The parameters are shown for two different high-level radiofrequency schemes [47].

TESLA Linear Collider which are used as a baseline for the ILC [24] as given in table 3.2.

There are a number of elements which provide collisions in a linear collider. The central element of the ILC concept is the superconducting RF technology that will be used to accelerate electrons and positrons in the main linac. The choice of accelerating gradient is perhaps the single most important parameter decided, since it determines the length of the machine and has significant cost implications. Electrons and positrons are produced in a source and accelerated to a few GeV. They are injected into a damping ring to reduce the phase space volume of the bunches. During this process these bunches are cleaned and prepared to be used in the main linac where they get the final energy. In the accelerator, the beam delivery system is treated in such a way to condition the bunches for the collision, collimates away tails and eventually focuses the bunches into the interaction region. Beam is then ready to collide. After collision, there is a region behind the interaction point, where beam is dumped and its energy is absorbed as shown in figure 3.1.

The design of the ILC is based on superconducting cavities. An aggressive peak accelerating gradient of 35 MV/m has been chosen which poses a formidable

challenge to achieve this gradient in production cavities. A Japanese cavity now demonstrated the accelerating gradients of 31.5 MV/ for the first time at a test which took place at the Superconducting radio-frequency Test Facility (STF) at KEK [48]. To reach the energy of 500 GeV about 10km of accelerator is needed, based on an operating gradient of 31.5 MV/m for the baseline design. The injection chain, the beam forming, and the beam delivery add another 5-8 km per side, so that in the end the total site length will be about 33 km. If an upgrade to 1 TeV will be done later on, an additional tunnel is needed which will provide additional RF power to the beam.

The electron source is planned to be a conventional laser based electron source, as has been used at the SLC and also at the Tesla Test facility [49]. This allows high intensity production of polarised electrons, and is a very well understood technology.

For the positrons, an alternative to the conventional source is an undulator based source. A high energy electron beam - in principle the electron beam from the main linac can be used for this - is used to produce a very intense photon beam. These photons are then used to produce positrons. The advantage of this source is that it can deliver larger currents for the positron linac, and that it has the option of producing polarised positrons.

The damping rings are a major part of the overall ILC infrastructure. The finalised scheme foresees two rings with a possibility of installing a third damping ring. Each ring has a circumference of 3km at the start of the two linacs. The length of the damping ring is less than the RDR value, 6km, due to a reduction of the number of bunches per pulse by a factor of two from 2625 to 1312. This scheme is currently under aggressive study and It would require a different and untested technology for the kickers, not based on magnet technology but on RF cavities itself. When inside the damping ring, the bunches are subjected to wigglers which will help to reduce the vertical emittance of the bunches. For electrons a one stage damping is deemed sufficient, for positron, two rings on top of each other might be needed to provide enough damping.

The designed luminosity of the ILC is $2 \times 10^{34}\mathrm{cm}^{-2}\mathrm{s}^{-1}$. The average bunch-crossing rate will be $15 - 30$ kHz and the interaction rate will be dominated by $\gamma\gamma$ interactions (~ 0.1 events per crossing). Because of such a low rate, there is no need for a trigger, so the acceptance is maximised. Figure 3.2 shows the beam

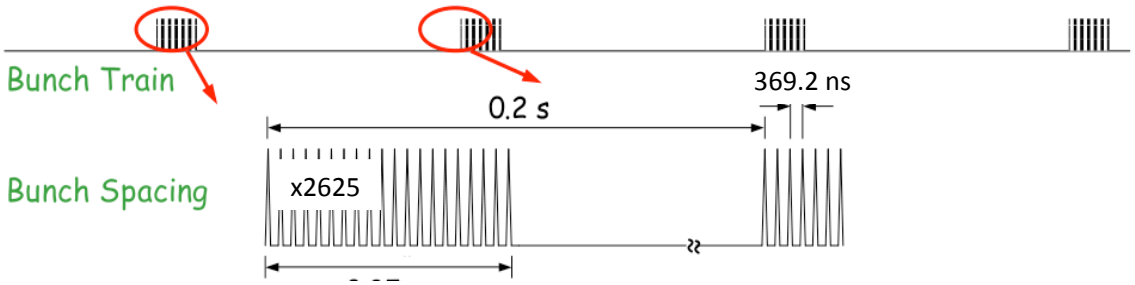

Figure 3.2: The proposed beam structure for ILC [43].

structure for the ILC.

Table 3.2: Main parameters of the International Linear Collider for the energies $\sqrt{s} = 500$ GeV.

Parameter	Label	Units	500 GeV
Luminosity	L	$10^{34}\text{cm}^{-2}\text{s}^{-1}$	2
Number of bunches per pulse	n_b		2625
Number of particles per bunch	N	10^{10}	2
Pulse train length	T_p	μs	950
Bunch interval	t_b	ns	369.2
Repetition rate	f_{rep}	Hz	5
Bunch crossing rate	$f_b = f_{rep}\ n_b$	Hz	13,125
R.M.S beam size at IP	σ_x	nm	639
R.M.S beam size at IP	σ_y	nm	5.7
R.M.S bunch length	σ_z	μm	300
Acceleration gradient	E_{acc}	MV/m	31.5
Beamstrahlung	δ_E	%	2.4

Due to beam-beam interactions there is a high background. The high charge density of the colliding beams produce intense emission of beamstrahlung photons. These photons broaden the energy spectrum of the colliding beams towards lower energies, with typically $85-90\%$ of the luminosity being produced at energies higher than 95% of the nominal center-of-mass energy. The energy loss due to beamstrahlung is roughly of the same size as initial state radiation. These photons also give rise to secondary electrons and positrons in the interaction region. By applying a high magnetic field these pairs can be confined inside a cylinder of radius < 3 cm around the beam line. The signal-to-background

ratio is favourable at lepton collider compared to a hadron collider. With high luminosity, many physics scenarios can be explored in a few years of operation.

The direct mass reach of ILC is limited by the available center-of-mass energy to less than 1 TeV. But due to the clean environment, direct signals of particles with low cross sections, or leaving only a very small amount of visible energy in the detector, can be discovered. The measurements of known processes and the detection of deviation from the expectations of the SM may lead to the indirect discovery of New Physics. So the precision measurements at ILC are the strongest aspect of the collider, allowing the exploration of quantum effects and the possibility to extrapolate the observations to energy scales far above the center-of-mass energy like Planck or GUT scale.

3.3 Detector Concepts for ILC

To extract full information from the physics potential of ILC, highly efficient detectors are needed. There were initially four detectors designs developed. SiD (Silicon Detector) [51], LDC (Large Detector Concept) [57], GLD (Global Large Detector) [56] and "the 4th Concept" [58] with plans to choose two for the final accelerator. The plan was to have these detectors at fixed positions but it turned out to be too expensive. The current design has a single interaction point with the detectors in a "push/pull" arrangement, so that the detector in use at any particular time can be switched out quickly and the other detector moved into the beam line. This should save considerable expense on beam delivery components and the civil engineering required to dig the two detector caverns and the connecting beam tunnels. This option presents a considerable practical challenge to make the switching process quick and realignment reliable. Because of their similarities the LDC and GLD collaborations decided to merge efforts into developing a single detector, International Large Detector (ILD). Hence, at the end only two detector study groups were validated by the ILC Research Director following the recommendation of the International Detector Advisory Group (IDAG) [44]. These detectors are:

- SiD (Silicon Detector) [51]
- ILD (International Large Detector) [50]

The concept of particle flow as a reconstruction method has driven many detector designs [46]. Briefly, this involves reconstructing each particle in an event individually by accurate calorimeter clustering. Charged tracks are then matched to clusters in the calorimeter and all other clusters are reconstructed as neutral particles. This requires a highly segmented calorimeter. Separating the particles in the calorimeter is often more important than accurately measuring the energy of individual particles, so the choice of using particle flow is fundamental to a detector's design.

The physics studies in this thesis were performed using the ILD detector model. But a brief description of the SiD detector concept is given in the next section.

3.3.1 The SiD concept

The SiD concept as shown in figure 3.3 is designed to be sensitive to a wide range of possible new phenomena at the ILC. A plan view of one quadrant of the detector is shown in figure 3.4. SiD is based on silicon tracking silicon-tungsten electromagnetic calorimetry, highly segmented hadronic calorimetry, and a powerful silicon pixel vertex detector. SiD also incorporates a high field solenoid (5T), iron flux return, and a muon identification system. The choice of silicon detectors for tracking and vertexing ensures that SiD is robust with respect to beam backgrounds or beam loss, provides charged particle momentum resolution, and eliminates out of time tracks and backgrounds.

The SiD concept recognises the fundamental importance of calorimetry for ILC physics, and adopts a strategy based on Particle Flow Calorimetry. This leads naturally to the choice of a highly pixellated silicon-tungsten electromagnetic calorimeter, and a multi-layered, highly segmented hadron calorimeter. Achieving excellent jet energy resolution requires both the calorimeters to be located within the solenoid, and cost considerations push the design to be as compact as possible, with the minimum possible radius and length. The use of a high magnetic field solenoid (5 Tesla) compensates for the reduced radius and improves the separation of charged and neutral particles in the calorimeters. Given the high magnetic field, an all-silicon tracker, with its good intrinsic resolution, can provide excellent charged particle momentum resolution. The high magnetic field also constrains e^+e^--pair backgrounds to a minimal radius, and so allows a beam-pipe of small

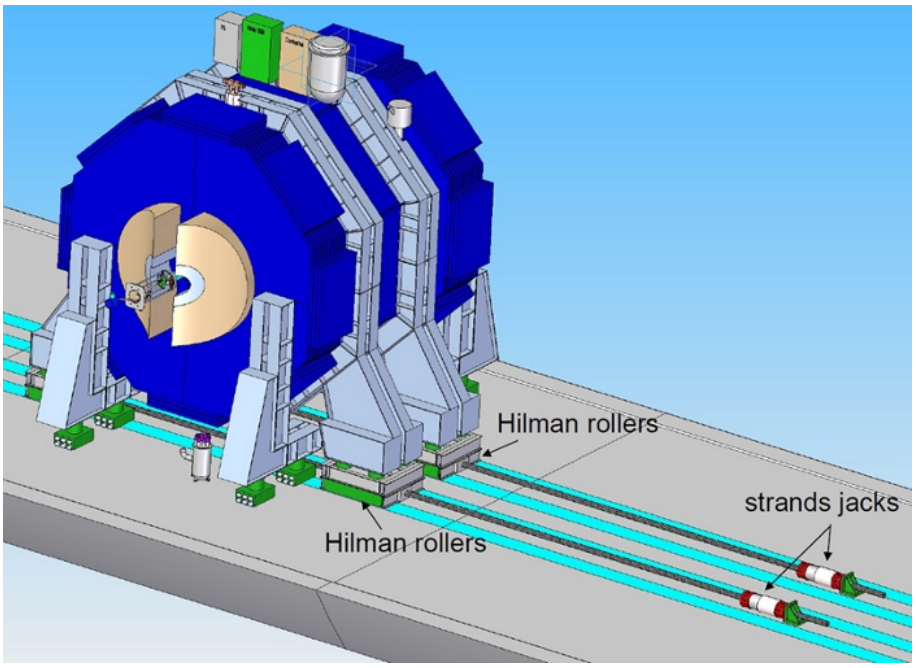

Figure 3.3: The SiD detector mounting on Hilman rollers for push-pull scheme. [51]

radius for high performance vertex detection. The SiD baseline detector has the following components, moving from small to large radii:

- The vertex tracker has five barrel layers of pixel detectors augmented with four endcap layers on each side, beginning at a radius of 1.4 cm and extending to 6.1 cm. The endcap design ensures excellent pattern recognition capability and impact parameter resolution over the full solid angle.

- The main tracking system consists of five layers of silicon microstrip sensors and four endcap layers, which tile low mass carbon fiber/rohrcell cylinders and endcap planes. The sensors are single side Si, approximately 15 cm^2, with a pitch of 50 μm. With an outer radius of 1.2 m and a 5 Tesla field, the charged track momentum resolution will be better than $\sigma(1/p_T) = 5 \times 10^{-5}$ GeV^{-1} for high momentum tracks.

- SiD calorimetry is optimised for jet energy measurement, and is based on a particle flow strategy, in which charged particle momenta are measured

Figure 3.4: Illustration of a quadrant of SiD. Values are in units of mm. [51].

in the tracker; neutrals are measured in the calorimeter and then the charged and neutral components are added. SiD calorimetry begins with an exceptionally dense highly pixilated Silicon - Tungsten electromagnetic section. The ECal has alternating layers of W and silicon pixel detectors; there are 20 layers of 2.5 mm thick tungsten followed by 10 layers of 5 mm tungsten. The silicon detector layers are only 1.25 mm thick. This results in a Molière radius for the thin section of 13.5 mm. The sensor are divided into 1024 hexagonal pixels, forming an imaging calorimeter with a track resolution of ~ 1 mm. The same technology is used in the endcaps.

- The Hadronic Calorimeter (HCAL) is made from 4.5 λ, (λ is the interaction length) of Stainless Steel, divided into 40 layers of steel and detector. The baseline detectors are RPCs with 1 cm pixels inserted into 8 mm gaps between the steel layers. The same technology is used for the endcaps.

- The calorimetric coverage is completed in the forward direction by a LumCal and BeamCal. The LumCal overlaps the endcap ECAL. The LumCal is Si-

W, with the pixelation designed to optimise the luminosity measurement precision. The BeamCal is the smallest angle calorimeter and is mounted to the inboard side of QD0 shown in figure 3.4. The BeamCal sensor technology may be diamond or low resistivity Si.

- The SiD 5 Tesla superconducting solenoid is based on the CMS design, but has 6 layers of conductor. The stored energy is ∼1.6 GJ. The critical cold mass parameters, such as stored energy/Kg, are similar to CMS. The CMS conductor is the baseline choice, but SiD is developing an advanced conductor that would eliminate the e-beam welding of structure alloy and be easier to wind. SiD will carry all the solenoid utilities (power supply, quenching protection, etc) except for the He liquefier, which will be connected by a vacuum insulated flex line.

- The flux return and muon system begins at a radius of 3.33 m and extends to 6.45 m. The flux is returned with an iron structure, configured as a barrel with movable endcap. The present design limits field leakage to < 100 G at 1 m. The flux return is 11 layers of 2cm iron. The flux return also is the absorber for the muon identifier and is an important component of SiD self shielding. The barrel is composed of full length modules to help keep the structure stable during push and pull and to enable full length muon detectors. The endcap support the final-focus QD0 magnets, with provision for transverse alignment of the quads and vibration isolation. A platform fixed to the barrel supports the 2K cryogenic system for the QD0s.

The details of the current status of the SiD concepts is given in reference [51].

3.3.2 The ILD Concept

The International Large Detector (ILD) is a concept for a detector at the ILC. ILD has been conceived to use the particle flow method, and so has finely segmented calorimetry as a major design goal. Tracking is achieved primarily with the silicon pixel vertex detector and a large gaseous tracker, but with extra silicon detectors in regions of low coverage. A 3.5 T magnet using similar technology to that of the CMS detector provides the magnetic field [52, 53]. Figure 3.5 shows the detector concept and Figure 3.6 shows a quadrant of the detector.

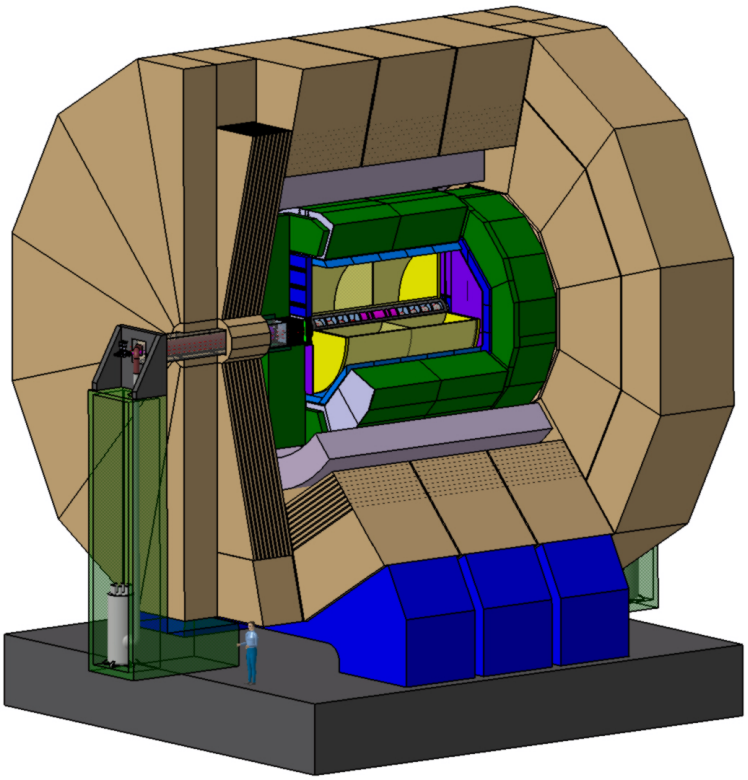

Figure 3.5: The ILD detector [50].

Moving outwards radially is the vertex detector (VXD), intermediate silicon tracker (SIT), the time projection chamber (TPC), the electromagnetic calorimeter (ECAL), the hadronic calorimeter (HCAL) and the magnet return yoke. There is an additional silicon tracking layer between the TPC and the ECAL called the SET.

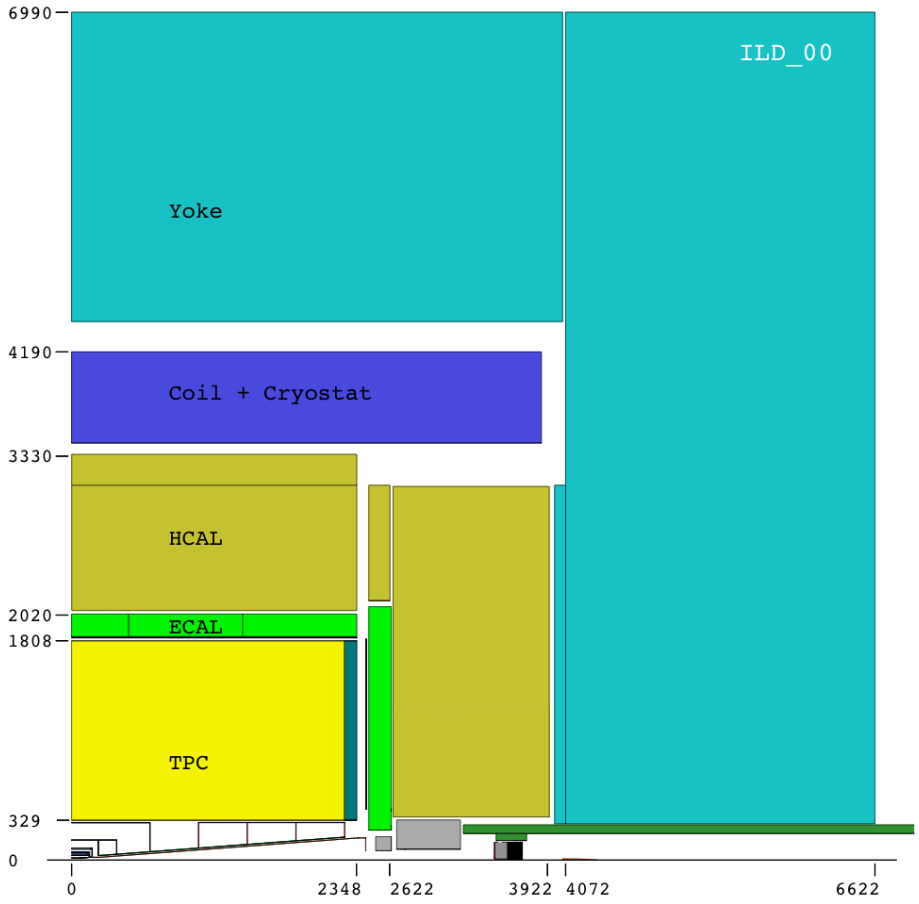

Figure 3.6: Illustration of a quadrant of ILD concept. Values are in units of mm. [50]

In the forward direction are the forward tracking discs (FTD), endcap tracking discs (ETD), luminosity calorimeters (LCAL and LHCAL) and the beam calorimeter (BEAMCAL). These forward calorimeter improve the hermeticity and provide additional functions. The LCAL will use small angle Bhabha scattering to measure the luminosity, and the BEAMCAL will analyse electron-positron beamsstrahlung pairs to provide feedback to the beam delivery system.

The inner tracking system is shown in Figure 3.7. Each of the three main tracking systems, VXD, FTD and TPC, have been designed to be capable of stand alone tracking. The VXD is a three double layer design carried forward from GLD because it had the best impact parameter resolution. The FTD is a series of 7 discs that cover the forward direction down to approximately 10°. Forward coverage by the VXD extends to 15°, although at this angle the obliqueness of tracks reduces precision.

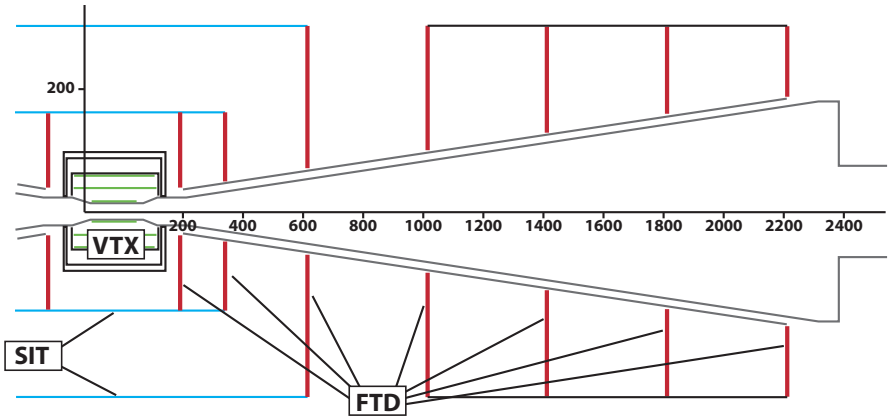

Figure 3.7: The ILD inner tracking system. Lengths are in units of mm. [50]

The other tracking detectors are the FTD between the VXD and the TPC, and the SET and ETD between the TPC and the ECAL in the radial and forward directions respectively. These extra detectors are designed to augment the main tracking with additional high resolution measurements. The desired momentum resolution is [50]:

$$\sigma\left(\frac{1}{p_T}\right) \approx 2 \times 10^{-5}\,\mathrm{GeV}^{-1} \tag{3.3}$$

The electromagnetic calorimeter is made from layers of tungsten absorber and silicon detectors with a cell size of 5×5 mm^2. The physics studies presented in this thesis are performed with a hadronic calorimeter using scintillators, although gaseous detectors are under active research. In both cases the hadronic calorimeter uses stainless steel as an absorber. These choices of calorimeter technology are not intended as an indication of the final technology; the most advanced technology was simply chosen for the first stage of physics simulations.

3.4 Technologies for ILD subdetectors

3.4.1 The Vertex Detector

Several designs and silicon pixel technologies are being considered for the vertex detector. The choice of sensor is still very much in question, with the competing designs being challenged with producing a working ladder by approximately 2012. Details of different technologies are available from [45]. SiD and "4th" have been pursuing a design with short barrels and endcaps, whereas LDC and GLD (and hence ILD) have been looking at long barrel designs [43]. Although the long barrel designs suffer from reduced forward sensitivity due to the obliqueness from the interaction point, a short barrel and endcaps provides a significant challenge for readout electronics placement.

It is widely accepted that a critical parameter for the performance of the vertex detector is the radius of the innermost layer. In essence, this is determined by the radius of the beam pipe, although hits from background electron-positron pairs could force this layer further out. How much the inner layer is affected by backgrounds depends on the integration time of the technology used - technologies with a large integration time will have to be placed further from the beam pipe or the occupation from backgrounds will be over whelming. The integration times of current proposals range from a single bunch to the entire bunch train and having to move the inner layer out from the beam pipe is a very real possibility.

The sensor choice will make a huge impact on the rest of the design. Each of the ten or so technologies being investigated have their own advantages and disadvantages, so it is not simply a case of picking the sensor with the shortest integration time. Power consumption needs to be kept to a minimum to prevent heat build up, and the readout electronics required will have to be factored into the mechanical design. The material budget excludes the option of liquid cooling, so all of the technologies will have to prove that gas cooling is sufficient to keep them at their operating temperature. The sensor itself will have to be very thin, both to minimise material and also the weight and hence the support required to hold it in place. An ILC vertex detector should be able to pin point the interaction point to less than a μm in x and y, a very ambitious goal, so keeping each sensitive layer stable to less than this is imperative. An additional problem is that all of the technologies minimise heat build up by power cycling during

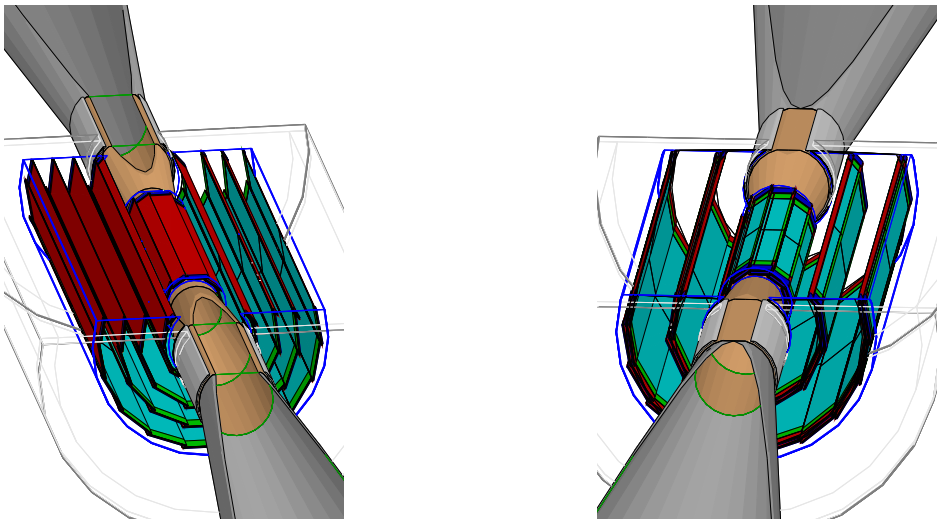

Figure 3.8: Vertex detector geometries of the two design options for ILD. Left: 5 single ladders. Right: 3 double ladders [50].

bunch train gaps, so Lorentz forces from the detector's 3-4 T field during the high current power up will have to be accounted for. A high power sensor will therefore require more support than a similar low power option.

3.4.2 The Time Projection Chamber

Time Projection Chambers are the technology that have been in use for over 25 years, and have proven to be accurate and reliable [54, 55]. They provide an accurate 3 dimensional path for charged particles with a minimal amount of material in their path. The tracking requirements at the ILC however will require a significant increase in performance. The desired momentum resolution is $\delta(1/p_T) \sim 9 \times 10^{-5}$ GeV/c [42], which will require the development of a number of technological improvements to the standard TPC design. A time projection chamber works by having a large volume of gas, which ionises when the charged particles under study pass through it. A large cathode in the center of the detector causes the ionised electrons to drift towards the endcaps, which are held at ground potential. If the ionisation electrons happen to deviate from a path perpendicular to the beam axis, the large magnetic field from the main

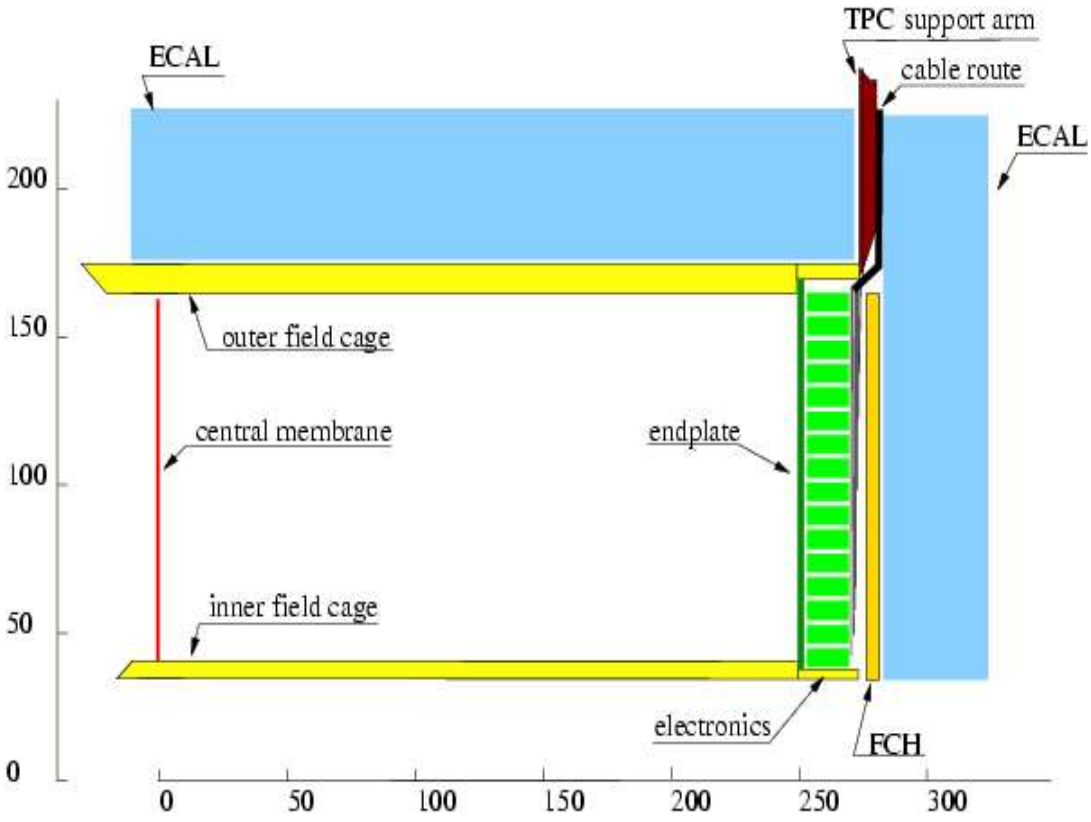

Figure 3.9: The Time Projection Chamber for ILD. Values are in units of cm.

magnet will cause them to travel in small radius, helical trajectory so that they reach the anode in approximately the same position in x and y that they were ionised in. Measurement of this position for all ionised electrons hence gives x and y coordinates of the particle under study all along its path through the gaseous volume. If accurate knowledge of electron travel through the gas is combined with knowledge of the time from ionisation to detection at the anode then a z coordinate can also be inferred, hence the "time projection". The time of ionisation needs to be taken from an external source.

Traditionally, the anode consisted of several wires at known positions; when a signal was detected on one of these wires one of the spatial coordinates of the ionised electrons was known, the anode itself was also the detector. A process of natural amplification occurs in the gas - as the electrons approach an anode wire, the electric field gradient increases and the electrons are accelerated. As they do so, they can knock additional electrons from the gas atoms which are also accelerated and ionise more atoms. This cascade, known as a Townsend avalanche, increases the signal.

One of the new technologies under consideration for improved performance is the Gas Electron Multiplier (GEM). This is a thin piece of dielectric coated on both sides with metal. Tiny holes of no more than 100 μm are drilled in the sheet, so that when a high potential is applied between each side the electric field is concentrated through the holes. Any electrons approaching the sheet are accelerated through the holes, and the field gradient is high enough to create a very localised avalanche that can be detected just the other side of the sheet.

Another candidate is Micromegas (MICROMEsh GAseous Structure) detectors [59]. These involve holding a fine wire mesh a short distance (typically 0.1 mm) above a plane of detector pads. The mesh is held at a voltage of order 400 V so that avalanches are caused in the region between the detector plane and the mesh.

3.4.3 Calorimetry

ILD has been pursuing the particle flow approach, whereby the energy of charged particles is taken from the tracking, and the energy of neutrals from the calorimeters. This requires very high spatial resolution for the calorimetry, so that tracks can be matched to the charged particle clusters (which are effectively

ignored) to distinguish them from clusters created by neutral particles. A mistake in the matching process will either result in missing energy, if a neutral cluster is thought to be associated to a track and hence ignored; or more likely in double counting if the energy of a charged particle is taken from its track, and its calorimeter energy wrongly assumed to be from a neutral particle.

The calorimeter system is comprised of two parts: the electromagnetic and hadronic part, which are installed within the coil to minimise the inactive material in front of the calorimeters.

Electromagnetic calorimetry

Electromagnetic calorimeters are designed to measure the energy of particles that are absorbed in an electromagnetic shower, i.e. either photons or electrons. High energy (above approximately 1 GeV) electrons primarily lose energy through bremsstrahlung, emitting a high energy photon. High energy photons primarily lose energy through pair production, creating an electron and positron pair. These processes continue in turn until ionisation (for electron) or Compton scattering (for photons) takes over as the main form of energy loss. It is the energy loss in these processes that is actually measured by the calorimeter.

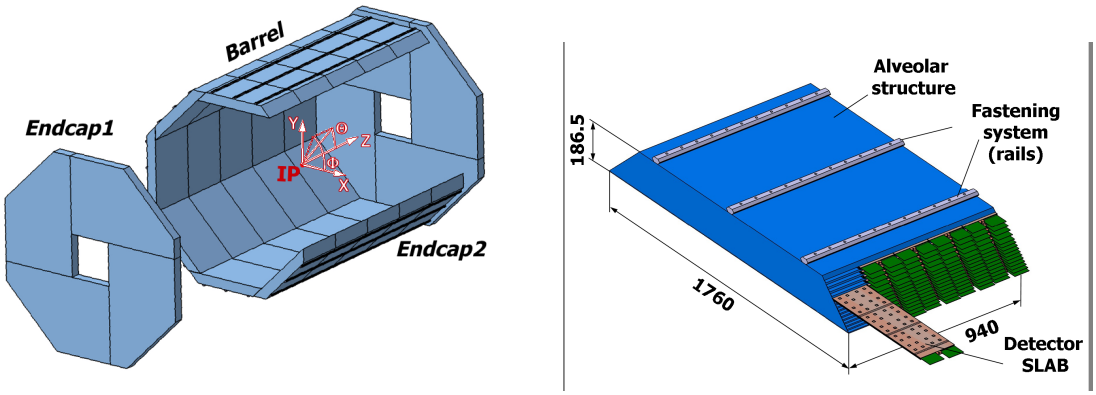

Figure 3.10: Global layout of the ILD ECAL (Left) and layout of one module (Right) [50].

The calorimeter thus has two roles: to induce bremsstrahlung and pair production, and to measure ionisation. For low energies both roles can be fulfilled by one material (homogeneous calorimeter), but at high energies the volume

required to contain the shower would be prohibitive. All ILD electromagnetic calorimeter designs interweave layers of a material with a high radiation length with the detector material. Since shower separation is the primary concern with particle flow algorithms, tungsten will be used as the absorber to contain showers laterally since it has a low Molière radius. Lead is also being considered as a lower cost option. Another goal to minimise lateral shower spread is to minimise the thickness of the sensitive layers. Current designs are aiming for sensitive layers 3 mm thick, including readout. The tungsten absorber layers are between 2 and 3 mm thick at the face of the calorimeter, but then switch to approximately 4 mm thick in the middle of the detector.

Silicon pad diodes, monolithic active pixel sensors (MAPS) and scintillator strips and tiles are all being considered for the sensor layers. MAPS is a relatively new proposal. The technology choice for ILD is still in question, but the scintillator option was used for the physics analyses in this thesis.

Hadronic Calorimetry

The same principle of interspersing a detector medium with a non-sensitive material to induce the shower also applies to hadronic showers. Like EM showers, hadronic showers are an inherently stochastic process, making accurate incident particle energy measurements difficult. The stochastic nature means that the error on the measured energy reduces as energy increases, as opposed to the tracking which has reduced energy resolution for very straight tracks, i.e. for high energy particles. Since any π^0 particles produced will predominantly decay to two photons, hadronic showers naturally have an element of electromagnetic showers as well.

Hadronic showers extend much further than electromagnetic showers, so hadronic calorimeters are naturally larger than electromagnetic calorimeters. The size creates the most common deciding factor in the choice of absorber material - such a high volume of detector requires a very low cost material. Stainless steel was chosen for the analysis presented in this thesis, with the added advantage of its mechanical qualities. Lead is also an option because it would have equal response to the hadronic and electromagnetic components of the shower.

Both gaseous and scintillating detectors are being researched for the detector layers. A gaseous detector layer would use either GEM, micromega or resistive

plate chambers (RPCs). A scintillating layer would use either scintillating tiles, scintillating strips or a combination of the two to maximise granularity.

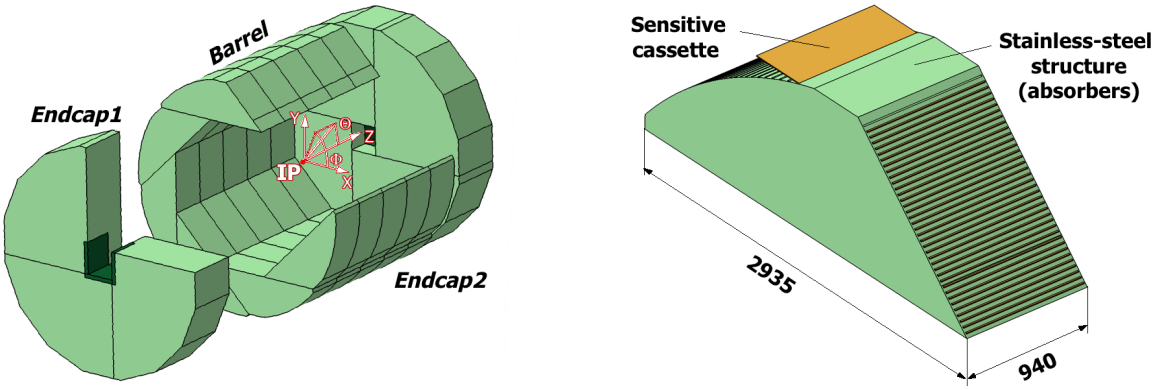

Figure 3.11: Design layout of the ILD HCAL (Left) and layout of one module (Right) [50].

3.4.4 Coil and Return Yoke

The ILD detector design requires a 3.5 T field in a large volume, with a high field homogeneity within the TPC and with a reduced fringe field outside the detector. The parameters of the ILD magnet are very similar to the CMS ones [52] and the basic designs of both magnets are the same. An anti Dipole in Detector (DiD) is also added in the design, which allows to compensate the effect of the crossing angle for the outgoing beam (and pairs) after the interaction point.

Magnet Technology

As several technical aspects of the magnet are quite similar for the ILD and CMS, the experience of CMS will help out for ILD [53]. The conductor will consist of a superconducting cable co-extruded inside a low electrical resistivity stabiliser and mechanically reinforced by adding high-strength aluminium alloy. Two different conductors will be necessary, using different superconducting cables and a different ratio of mechanical reinforcement, but with the same overall dimensions. The winding will be done using an inner winding technique. The magnetic forces will be contained both by the local reinforcement of the conductor

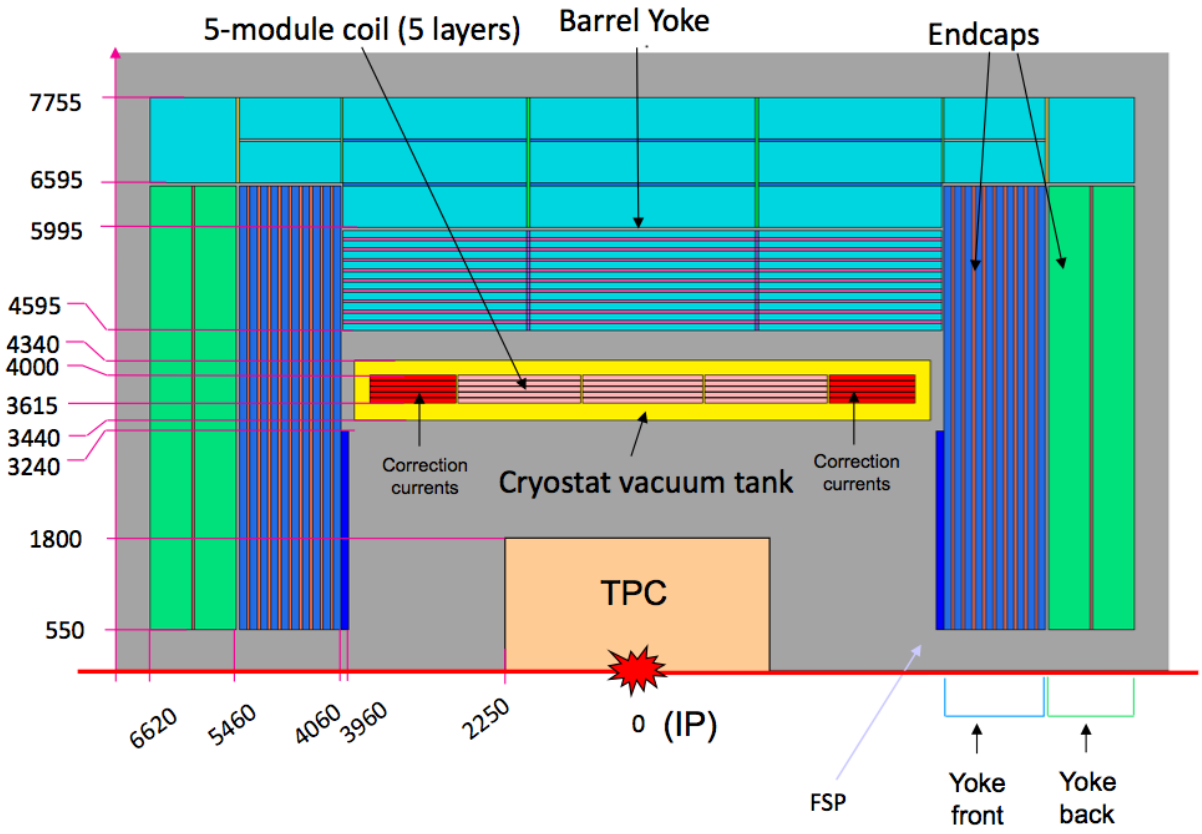

Figure 3.12: Cross section of the ILD Magnet [50].

and by an external cylinder. The coil will be indirectly cooled by saturated liquid helium at 4.5 K, circulating in a thermosiphon mode. The central barrel yoke ring will support the vacuum tank. Internal sub-detectors will be supported on rails inside the vacuum tank.

3.4.5 Muon Detector

The identification of leptons is an important part of the physics programme at the ILC. For muons above a few GeV, the instrumented iron return yoke is used as a high efficiency muon identifier. There is no need to trigger on muon tracks as is the case in hadron colliders. In the clean environment of ILC the linking of track candidates from the inner detectors with tracks in the muon system will be possible.

The system will be instrumented to allow a limited calorimeter performance as well as muon tagging. This will improve the energy measurement by tagging the late developing showers and hence act as a tail catcher.

A muon is easily identified by a track in a muon detector behind significant material. In the ILD design, the muon system is reached by muons with a momentum above about 3 GeV/c. The strong central magnetic field will keep lower energy particles from reaching the muon system. The main challenge then for identifying muons is the joining of a signal in the calorimeter with a track segment outside the coil. Multiple scattering in the calorimeters and the coil will have large impact on this, and the efficiency of association will increase with momentum. At lower momenta, the signal in the calorimeter will be used to identify muons.

Chapter 4

Event Generation and Reconstruction Techniques

The two analyses presented in this thesis use the same types of event samples. The techniques used to simulate, reconstruct and analyse these samples are almost the same for both of the analyses. In this chapter, the detector model is described that is used for the analysis in the following chapters. Techniques which are common to many physics analysis are also described in this chapter. Specifics of the two analyses are discussed in the chapter 5 and 6.

4.1 Software Tools

The ILD concept uses the Linear Collider I/O (LCIO) persistency format and event data model based software framework [63]. Mokka [63] is a GEANT4 [65] based application, used for the detailed simulation of the detector response. A MySQL [66] database is used to store the complete subdetector geometries and component materials which then make up the detailed detector structure. At reconstruction and analysis level, the geometrical properties are accessed by using the GEAR package [68].

Marlin [66] is the reconstruction package which is used to process Mokka generated events. Marlin is provided with plug-in modules, which are called processors, and can be loaded at the run time. These processors can be configured by steering files in xml format. The MarlinReco [62] package is used to carry out the event reconstruction. There are sets of modules for digitisation, track

finding, track fitting, particle flow reconstruction, and flavour tagging in the MarlinReco package. Tracks from standalone pattern recognition in the silicon trackers and in the TPC are combined and refitted using a Kalman-fitter based track reconstruction. Reconstruction of the individual particles in the event is performed with the particle flow algorithm in the PandoraPFA package [70]. The LCFIVertex package [61] employs code for vertex finding/fitting and uses a neural network approach for the identification of heavy flavour jets and estimation of the charge. The JetFinder algorithm within MarlinReco can be used to reconstruct as many jets as required for the analysis. MarlinReco contains some other tools such as the Reconstruction in abstract vertexing environments, RAVE toolkit [71] and kinematic fitting. A schematic diagram of these softwares is given in figure 4.1.

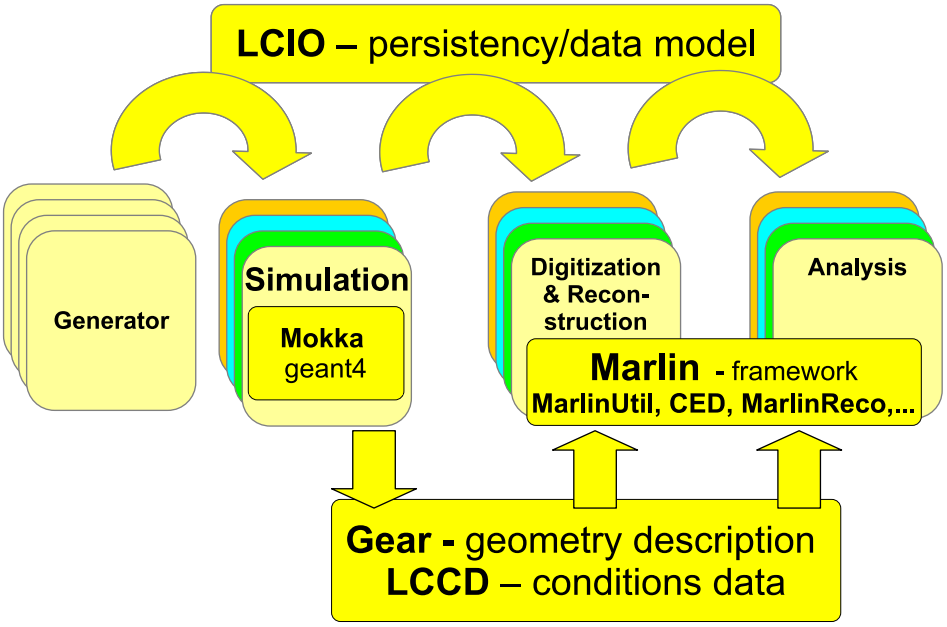

Figure 4.1: Software framework and tools used at different steps of processing [66].

4.1.1 The ILD Simulation Model

For the physics studies, a reference simulation model known as ILD_00 was created in the Mokka simulation program. As far as possible generic expected measurement performances are used instead of selecting a specific technology. As

an example, no readout technology is specified for the tracking systems, and the expected resolution is applied to the hits during digitisation.

In most cases the sub detectors have been implemented with mechanical support structures, electronics, cabling, and realistic dead material and cracks. The three double layers of the Vertex Detector, VXD, were constructed as 50 μm thick silicon ladders, and the Time Projection Chamber, TPC, had the inner and outer field cages modelled. The Forward Tracking Discs, FTD, and Endcap Tracking Discs, ETD, were modelled using discs, and the Silicon Tracker, SIT, and SET, (silicon tracking layer between TPC and ECAL) were modelled using cylinders.

The detector model ILD_00 was simulated with the parameters given in table 4.1.

Table 4.1: Geometrical parameters of the ILD_00 model. Lengths are in units of mm.

Parameters		ILD_00
B field		3.5 T
Beampipe R_{min}		14.5
Vertex Detector	Geometry	ladders
	layers	3 doublets
	R_{min}	16.0
Barrel SIT	layers	2 cylinders
	R_1, R_2	169, 309
TPC drift region	R_{min}	395
	R_{max}	1739
	z_{max}	2247.5
TPC pad rows		224
ECAL barrel	R_{min}	1847.4
	Layers	20+9
	Total X_o	23.6
ECAL endcap z_{min}		2450
HCAL barrel	layers	48
	R_{max}	3330
λ_l (ECAL + HCAL)		6.86

4.2 Particle Flow

Particle Flow [69] reconstruction provides the best way to achieve the jet energy goals for ILC. It poses certain requirements on the separation of photons and showers produced by neutral and charged hadrons.

The jet energy resolution for a given detector design comes from a combination of the detector performance and particle flow software. The unprecedented resolution of the jet energy to be achieved is $\sigma_E/E = 30\%$ of $\sqrt{1/E}$ for a wide range of jet energies at ILC [69]. If a cluster is not correctly assigned to a track or a photon is not resolved from a charged hadron shower, then there is a *confusion* [69] term which degrades the jet energy resolution. The particle flow and calorimeter clustering are performed in ILCSoft package in a single algorithm i.e. PandoraPFA [70]. There are six steps involved:

Track Reconstruction The track reconstruction for ILD is performed mostly on three subdetector VXD, FTD and the TPC separately. A magnetic field of 3.5T is provided outside the tracking system. For example to reconstruct an Interaction point, IP, the track selection is done by requiring at least 20 hits in the TPC or at least three hits in the FTD. There is no requirement on hits in the vertex detector. If there are fewer hits in the TPC or FTD then at least three hits in the vertex detector needed.

The track finding procedure is performed in the entire ILD detector by linking track segments found by the SiliconTracking processor in the silicon detectors and by the LEPTracking processor in the TPC. Each track is characterised by five parameters: Ω (signed curvature), $\tan(\lambda)$ where λ is the dip angle, ϕ (azimuthal angle of point of closest approach), d_0 (signed impact parameter), z_0 (displacement along z axis at the point of closest approach to IP). Figure 4.2 shows these parameters.

Calorimeter Hit Selection Hits identified as isolated on the basis of nearness to other hits, are removed from the initial cluster, and the left over hits are ordered into *pseudo-layers*. The ordering is done with respect to decreasing energy. The pseudo-layers correspond to the detector geometry in the way that pseudo-layers are crossed by particles while going outward. The assignment of hits to the pseudo-layers is carried out by using minimum information of the geometry of

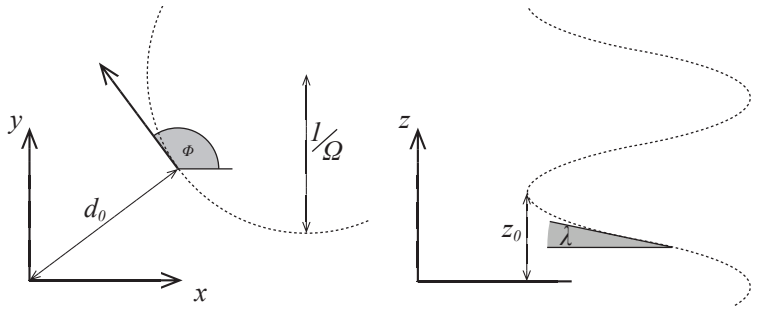

Figure 4.2: Parameters used to characterise a helical track. The reference point in our case is the interaction point, IP.

the detector. It uses the radius of the ECAL barrel, n-fold symmetry of the barrel, the $\pm z$ coordinate of front face of ECAL endcaps and the ϕ offset of the barrel stave with respect to the x-axis.

Cluster Reconstruction Inside the calorimeters, hits are gathered using a clustering algorithm. This algorithm works from the innermost to the outermost pseudo-layer and a direction to the clusters is assigned in this ascending direction. The initial direction of the cluster is the direction of the track. The hits are added to the clusters in the outward direction. In each pseudo-layer, hits are compared to the hits in the previous layer. The association of hits in different layers is made using a cone-cut $d_\perp < d_\parallel tan(\alpha) + \beta D_{pad}$ with α being the cone half angle, D_{pad} is the size of pixel in the layer being considered, β is the number of pixels added to the radius of cone, $d_\perp$ and $d_\parallel$ are the perpendicular and parallel displacement vectors with respect to the propagation direction.

Cluster Merging After the tracking and clustering is performed, a merger of clusters from tracks and hadronic showers takes place. Photons are identified by using the cut-based method while the tracks and hadronic showers are characterised by minimum ionising tracks, back scattering tracks and showers including hadronic interactions before merger. Clusters which are identified as photons are not considered for merger.

Statistical Re-clustering If jets are highly energetic such that the jet energy is greater than 50 GeV, the performance of the algorithm degrades due to the overlap of hadronic showers of different particles. A re-cluster of energy is performed by splitting clusters. This is achieved by temporarily assigning calorimeter clusters to the tracks and performing the association procedure using smaller values of α and β.

Particle Flow Objects (PFOs) Once track and cluster information is gathered, the PandoraPFA algorithm matches clusters to tracks, and performs particle reconstruction. The matching is achieved on the basis of the distance of closest approach of the track projection into the first ten layers of the calorimeter.

In particle flow, every constituent particle of the jet is reconstructed. The identified PFOs are used to reconstruct jets, with jet energy as the sum of the individual particle's energy within the jet. To identify individual PFOs as photons, electrons, muons, charged hadrons or neutral hadrons, the fraction of energy deposited in the ECAL and track-cluster matching is used. When the PFO is charged, tracking information is used to reconstruct the particle's energy; when the PFO is neutral then the calorimeter information must be used to reconstruct the particle's energy.

4.3 Jet Finding

The event processing grouphe reconstructed PFOs into jets, using the so-called Durham (k_T) clustering algorithm [72]. It involves computation of the scaled transverse momentum between two particles i.e.

$$y_{mn} = \frac{2(1 - \cos\ \theta_{mn})\ \min(E_n^2, E_m^2)}{s} \tag{4.1}$$

where (m, n) represents every pair of the final-state reconstructed particles with energies E_n, E_m and mutual angle, θ_{mn} and s is the center-of-mass energy. The two particles with the smallest values of y_{mn} are then combined and if their y_{mn} is smaller than a pre-defined parameter y_{cut}, they are replaced with a pseudoparticle with 4-momentum p_{mn}. The process of combining particles continues until a specific required number of objects is left. It forces reconstructed particles into the number of jets found.

4.4 Vertexing

The LCFIVertex package [67] provides tools for vertex finding, flavour tagging and vertex charge reconstruction. In the next section a brief overview of these tools is presented.

4.4.1 Vertex Finding

The LCFIVertex package provides the vertex finder ZVTOP originally developed at the SLD experiment [73]. There are minor improvements in the currently used version by including a Kalman vertex fit, and adjustments to use ZVTOP in events at the center-of-mass energies above the Z resonance.

The ZVTOP provides two algorithms complementary with each other. In this thesis ZVRES is used. The central idea of the ZVRES algorithm is to define the probability density function $f_i(\vec{r})$ describing each track i. The track function has a Gaussian profile in the plane normal to the trajectory. The track function is defined as:

$$f_i(\vec{r}) = \exp\left[\frac{1}{2}(\vec{r}-\vec{p})V_i^{-1}(\vec{r}-\vec{p})^T\right] \tag{4.2}$$

where $\vec{p}$ is the point of closest approach of track i to space point $\vec{r}$ and V_i is the position covariance matrix of the track. Then a *vertex function*, $V(\vec{r})$, is defined that gives high values in the region of true vertices. The simplest $V(\vec{r})$ for a collection of N tracks is:

$$V(\vec{r}) = \sum_{i=1}^{N} f_i(\vec{r}) - \frac{\sum_{i=1}^{N} f_i^2(\vec{r})}{\sum_{i=1}^{N} f_i(\vec{r})} \tag{4.3}$$

with the second term ensures that $V(\vec{r})$ approaches zero in spatial regions in which only one track contributes significantly.

Fake vertices can be suppressed by weighting the vertex function using the knowledge of the vertices' most likely position. Additionally, the IP position can be used to suppress the fake vertices from tracks passing close by each other in an area near the IP.

The other ZTOP vertex finder algorithm is ZVKIN. It works in the particular situation when ZVRES fails. For example when a b jet decays into two particles but only one charged track is detected. In the current thesis only ZVRES is used

as it applies to a broader class of jets. For more details of ZVKIN, reference [67] can be consulted.

4.4.2 Neural Networks

A Neural Network (NN) is an information processing paradigm. It is composed of a large number of highly interconnected processing elements (nodes) working in unison to solve specific problems. A NN is configured for a specific application, such as pattern recognition or data classification, through a learning process. As an application to the high energy physics, NN achieves usually better results than simple cuts. Basic elements of the NNs, nodes, can exchange information between themselves through synapses. Nodes are grouped into three types of layers: input, hidden and output.

The aim of a NN in a physics analysis is to separate the signal events from the backgrounds. Given a certain number of discriminating variables, $x_1, x_2, ..., x_n$, the NN attempts to define a border between the signal region and the background region. During the training of the NN, weights are assigned to each region. If it is possible to find a set of discriminating variables which distinguish the signal and the background regions in their multi-dimensional space, figure 4.3a, the signal region is assigned large weights and the background region is allotted small weights. Then the NN output will have a peak at one for signal events, figure 4.3b.

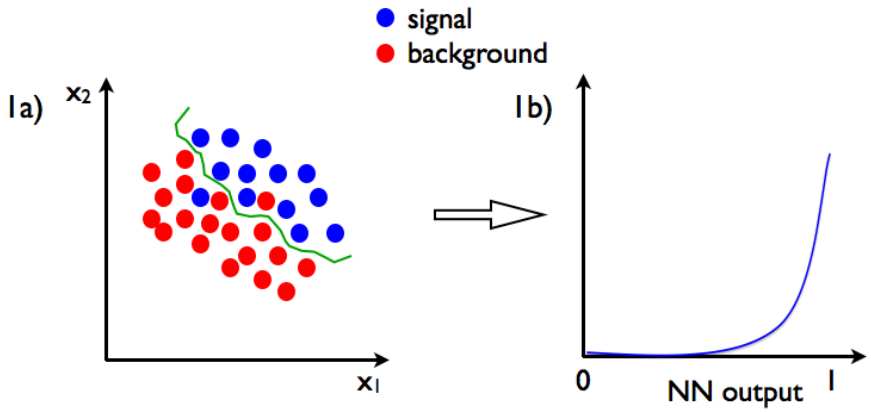

Figure 4.3: Signal and background separation in NN and its output. [79].

In the complex cases, where signal and background are not well distinguished

within the discriminators' space, one might be tempted to perform more training of the NN to improve the separation of the signal and background regions. This may lead to overtraining. In the overtraining, the neural network starts to create islands around concentrations of signal events, figure 4.4a. As in the islands there are not many background events large weights are assigned to them during the training, as well as low weights are assigned to the regions outside them. When one runs then the NN on test samples (different from the training sample), figure 4.4b, a significant fraction of signal events falls outside the islands (low weights) and to them very small values of the NN output will be given. To those events that fall inside the islands (large weights) the response from the NN should be close to one. That's a characteristic of overtraining of a NN: With a pure signal sample the response from the NN show two peaks, one at 0 and the other one at 1, figure 4.4c.

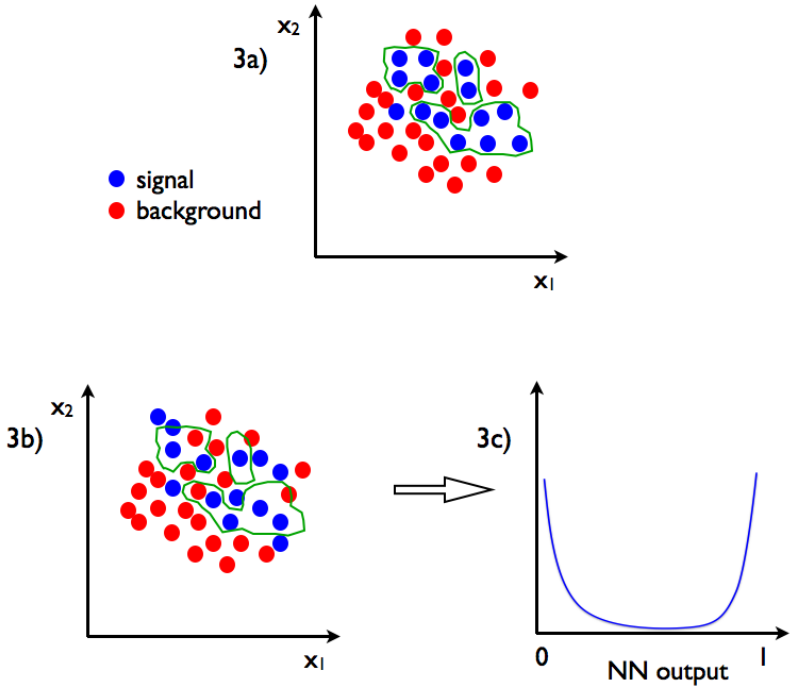

Figure 4.4: Overtraining in the NN. [79].

4.4.3 Flavour Tagging

The LCFIVertex package determines the flavour of the jets based on a neural network (NN). A network is trained on b decays, and another on c decays. Each jet is examined according to the trained NN values to get probabilities of b and c decays. A unique feature of this package is the distinction between IP and non-IP vertices. There are different sets of observables for jets containing one vertex and jets with more than one vertex. If only one vertex is found, then the most significant track information such as the impact parameter and the momentum of the track is used as input for the flavour tag. The most significant track is defined as the track with the smallest absolute value of the impact parameter, $d_0/\sigma(d_0)$, as discussed below. The observables from the second-most significant track help to discriminate between c and b jets, for which it is more likely that two tracks of high impact parameter significance are found, with one resulting from the decay of the leading hadron and one from the decay of the charmed hadron produced in that decay. Further observables, as given below, can be studied to tag the jets for the one vertex case. In practise different algorithms are used for one or more than one vertices but using the same variables. The networks are trained differently for one or more than one vertex. All of the networks used have 8 input nodes/variables, a hidden layer of 14 nodes and one output node. The following set of variables are used to distinguish the flavour of the jets.

Impact parameter significance

The impact parameter significance is the impact parameter divided by its error. Heavy flavour hadrons travel a short distance before decaying, so tracks from these decay products will tend to have larger impact parameters than tracks from light hadrons. This parameter can have a negative or positive sign depending on the intersection of the track with the jet axis in front (positive) or behind (negative) the vertex. Heavy flavour tracks will have positive impact significance as negative can only arise if the detector has imperfect resolution. Light flavour tracks should have symmetric impact parameters. The significance of the impact parameter in the xy plane is defined as $d_0/\sigma(d_0)$, and as $z_0/\sigma(z_0)$ in the z direction. In the one vertex case the track significance is given by $d_0/\sigma(d_0)_1$, and as $z_0/\sigma(z_0)_1$ in the z direction and similarly for the second-most significant track. The distributions of d_0 significance is given in figure 4.5 for a test sample.

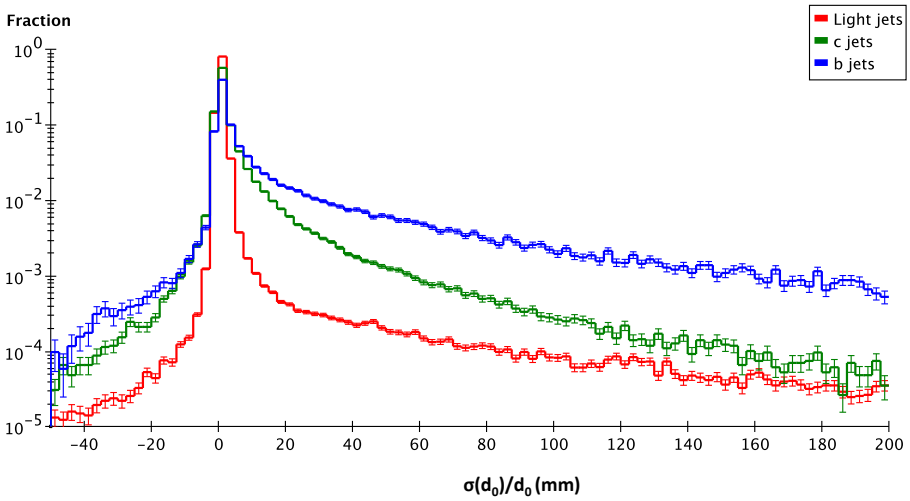

Figure 4.5: Input parameters for flavour tagging: d_0 significance [78].

Joint Probability

The joint probability, J, is the probability that all of the tracks come from the interaction point. The probability variables are calculated from the impact parameter significance in the xy plane and z of all the tracks in the jet. The significance distribution is given as $f(x)$ and probability of a track with significance x (not the spatial co-ordinate x) is:

$$P_i(x) = \frac{\int_x^\infty f(x)dx}{\int_0^\infty f(x)dx} \tag{4.4}$$

where i is to identify each track. This information for each track is combined to form the joint probability for the jet by:

$$J \equiv P \sum_{m=0}^{N-1} \frac{-\log(\prod_i P^i)_m}{m} \tag{4.5}$$

The significance distribution is approximated by a Gaussian with two exponential tails. Since the distribution for light flavours should be symmetric about zero, the form of this function can be found by fitting just the negative side. J_{xy} is the joint probability in the xy plane and J_z in z.

Track momentum

The momentum magnitude for the first and second most significant impact parameter tracks are denoted by $|p_1|$ and $|p_2|$ respectively.

Decay length

The decay length is the distance from the interaction point to the furthest vertex. This is defined as l.

Decay length significance

The decay length significance is the decay length divided by its error. This is defined as $l/\sigma(l)$.

p_T corrected mass

This is the invariant mass of the vertex after applying a momentum correction that would make the momentum vector point directly away from the interaction point and transverse to the beam axis, denoted by M_{P_T}.

Vertex momentum

The vertex momentum p_V, is the sum of the momenta of all tracks in the vertex.

Number of tracks in vertices

The number of tracks associated to any vertex that is not the interaction point, N_V. Figure 4.6 shows the distribution for a test sample.

Secondary vertex probability

This is the secondary vertex probability, P_{V_2}, of the tracks assigned to the decay chain, that is the χ^2 of a new track fit using all of these tracks.

4.4.4 Flavour Tagging Performance

The flavour tag uses the 8 variables presented in the previous section to train three neural networks: one produces the b-tag, one produces the c-tag and the

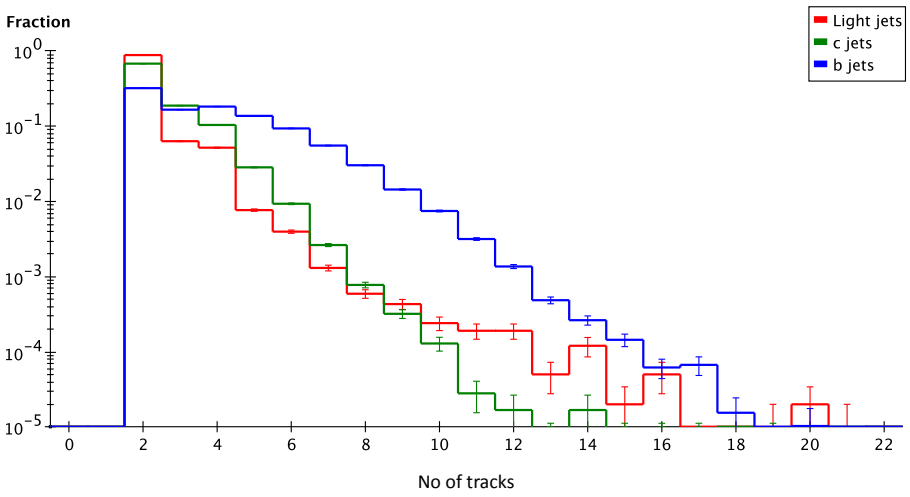

Figure 4.6: Input parameters for flavour tagging: Number of tracks in vertices [78].

third one is designed to tag c jets in the case that the main background is from b jets. Each of the tag outputs has a value between 0 and 1. Figure 4.7 shows the distribution of the b-tags and the c-tags for b, c and light flavour jets from a MC sample of Z bosons decaying into two jets. Figure 4.8 shows the flavour tag performance for the model ILD_00. Although in the ILD_00 model, vertex detector was implemented as three double sided layers, a performance studies for five single sided ladders vertex detector was also conducted by the Edinburgh ILC group. The performance difference between the two geometries is small as shown in figure 4.8. Therefore, any of the vertex detector model can be used for ILD_00.

4.5 Summary

The requirement for precision measurements at the International Linear Collider puts stringent requirements on the reconstruction software. The optimisation of tools and techniques for the reconstruction needs to be excellent. This chapter provides an overview of these tools and techniques. The analysis in the following chapters are performed by using these techniques.

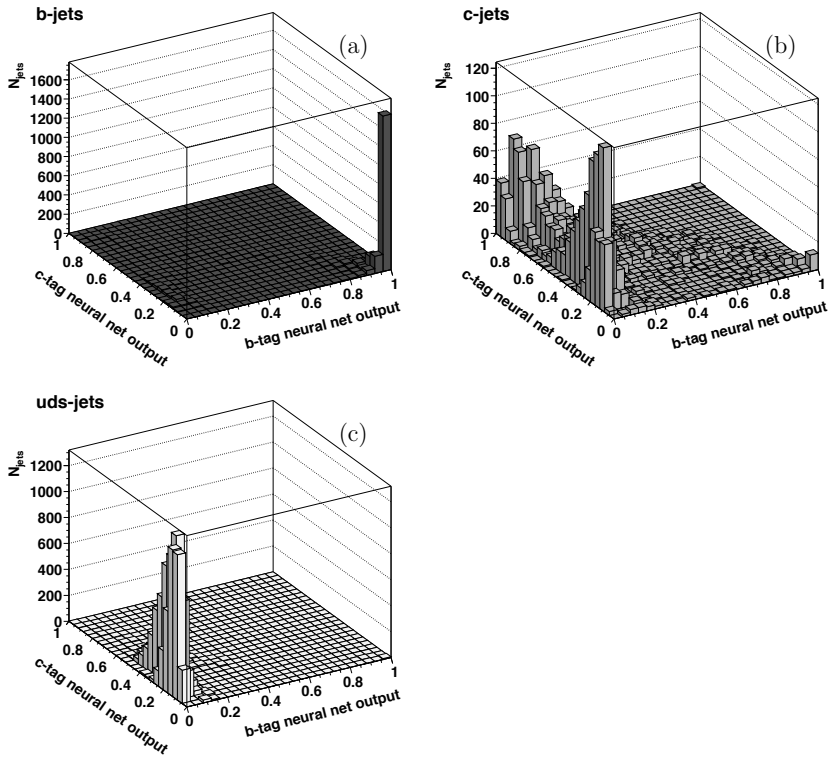

Figure 4.7: c-tag vs b-tag for samples consisting purely of (a) b quark jets (b) c quark jets and (c) light quark jets [67].

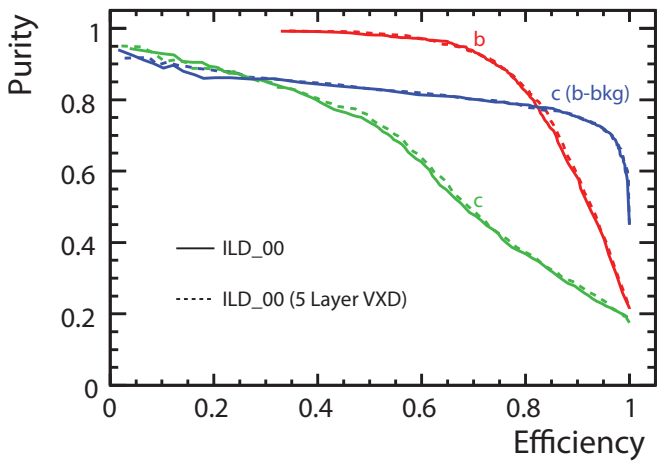

Figure 4.8: The flavour tag efficiency and purity for ILD model for 10000 Z pole events [79].

Chapter 5

Measurement of Higgs Boson Branching Ratios

An analysis of the Higgs branching ratios using $ZH \rightarrow llH$ was prepared for the ILD Letter of Intent (LoI) as a collaboration effort between Edinburgh and Bristol Universities. The muon channel was studied in Edinburgh, while the electron channel was studied by the Bristol collaborators [78]. The statistical uncertainties on the Higgs branching ratios to $b\bar{b}, c\bar{c}$ and gg are estimated, for an integrated luminosity of 250 fb^{-1} at $\sqrt{s} = 250$ GeV and a 120 GeV Higgs.

5.1 Monte Carlo Samples

The samples for this analysis were generated centrally at SLAC by the ILD optimisation group in preparation for the Letter of Intent (LoI) [50]. WHIZARD was used to generate these samples [80]. For simulation, the Mokka [63] package was used which is GEANT4 based. The detector model was ILD_00. MarlinReco, PandoraPFA and LCFIVertex packages were used for the reconstruction. Details of these packages are given in chapter 4.

We used a Higgs with mass 120 GeV and a center of mass energy $\sqrt{s} =$ 250 GeV. The signal used is $e^+e^- \rightarrow ZH$, where the Z decays as $Z \rightarrow \mu^+\mu^-$ and the Higgs boson, H, was allowed to decay according to its Standard Model branching ratios given in figure 2.7. The main background samples were generated as $e^+e^- \rightarrow \mu^+\mu^- q\bar{q}$. Other considerable background, W^+W^-, was also considered for the study. Table 5.1 below shows the sample sizes used in the analysis.

Table 5.1: Number of generated signal ($\mu^+\mu^- H$) and background events in the MC samples.

process	σ(fb)	Sample	Luminosity(fb^{-1})
$\mu^+\mu^- H$	17.1	5000	292
$\mu^+\mu^- b\bar{b}$	56.5	16800	297
$\mu^+\mu^- d\bar{d}$	57.5	17200	299
$\mu^+\mu^- s\bar{s}$	57.5	17000	299
$\mu^+\mu^- u\bar{u}$	53.0	15400	291
$\mu^+\mu^- c\bar{c}$	53.1	15600	291
$\mu^+\nu q\bar{q}$	58.5	100,000	1700

5.1.1 Polarised Electron and Positron Beams

The full potential of the linear collider could be realised only with the polarised electron and positron beams. For the ILC it is possible to get the polarised beams without a significant loss in the luminosity. Having both beams polarised would increase considerably signal rates and efficiently suppress unwanted background processes. This increase in the signal/background ratio gives additional opportunities for possible new discoveries. Studies have shown that the combination of two polarised beams are indispensable for revealing the structure of the new physics [74, 75, 76]. In the Higgs branching ratio analysis, therefore, we have used samples of different polarisations to get an effective beam polarisation of 80% for the e^- beam and 30% for the e^+ beam. Table 5.1 gives unpolarised sample corresponding to the luminosity 292 fb^{-1} while in table 5.2, the number of events corresponds to the luminosity 250 fb^{-1} with beam polarisation, $P(e^+, e^-) = (+30\%, -80\%)$.

5.2 Muon Identification

In our analysis we need a very efficient muon identification to reconstruct the Z boson. The muons arising from the decay of the Z boson are isolated and have large momenta. Single particle samples were generated and simulated with Mokka for the detector model ILD_00. In MarlinReco, no digitisation was implemented and therefore, there was no reconstruction of hits in muon detector. We thus only use calorimeter and tracking information for muon

identification. We obtained the discriminating variables and used them to train different methods implemented in the Toolkit for Multivariate Analysis Package (TMVA). The TMVA provides a ROOT-integrated machine learning environment for the processing and parallel evaluation of multivariate analyses. TMVA consists of the multivariate methods such as likelihood estimation, Neural networks with three implementations (MLP), boosted decision trees (BDT) etc. It provides training, testing and performance evaluation algorithms and visualisation scripts. TMVA supports the use of variable combinations and formulas [81].

Our signal was muons only and the background sample was pions and electrons. We optimised the output of above mentioned multivariate methods, by maximising $S/\sqrt{(S+B)}$:

$$\frac{S}{\sqrt{(S+B)}} = \frac{\text{signal}}{\sqrt{(\text{signal} + \text{background})}} \tag{5.1}$$

These muons are identified by using a set of variables which are used to train the TMVA. These variables use the calorimeter and tracker information. Four variables showed a high power of separation. These variables are:

- E_{Ecal}
- E_{Hcal}
- $E_{Ecal}/(E_{Ecal} + E_{Hcal})$
- $(E_{Ecal} + E_{Hcal})/p$

where E_{Ecal} and E_{Hcal} are the energies that the track leaves in the electromagnetic and in the hadronic calorimeter, respectively and p is the momentum of the tracks. Figure 5.1 shows the distribution of signal and background for these variables.

Based on the efficiencies of different multivariate methods, neural networks MLP, was decided to be used to identify muons. If MLP has value > 0.2932, the particle is identified as a muon. This cut value maximises $S/\sqrt{S+B}$ as shown in right figure 5.2. The distribution of purity verses efficiency for the TMVA output is given in left figure 5.2.

In neural networks, sometime overtraining can arise, as explained in section 4.4.2. We performed an overtraining check for our study and no overtraining was observed after the optimisation cuts. The response of MLP for the overtraining check is shown in right figure 5.2.

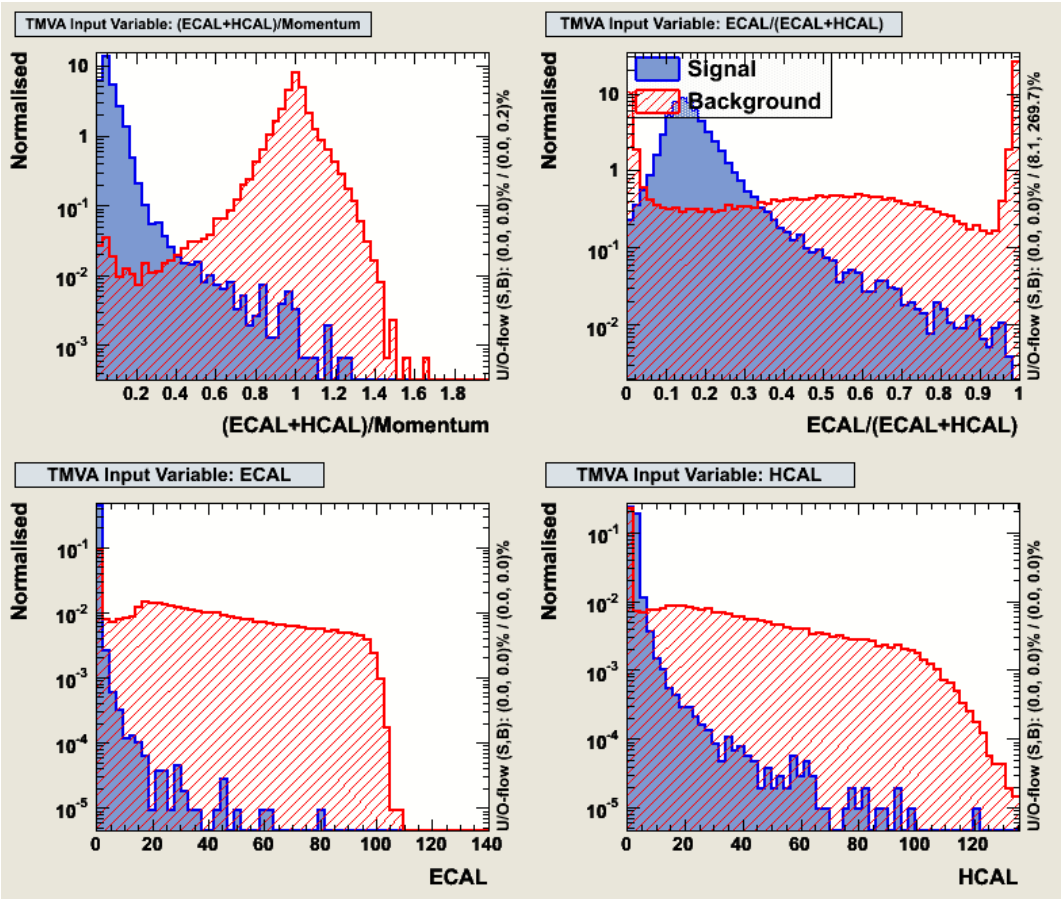

Figure 5.1: Signal and background distributions for the separation variables used for the muon identification. The x-axis in two bottom plots are in units of GeV.

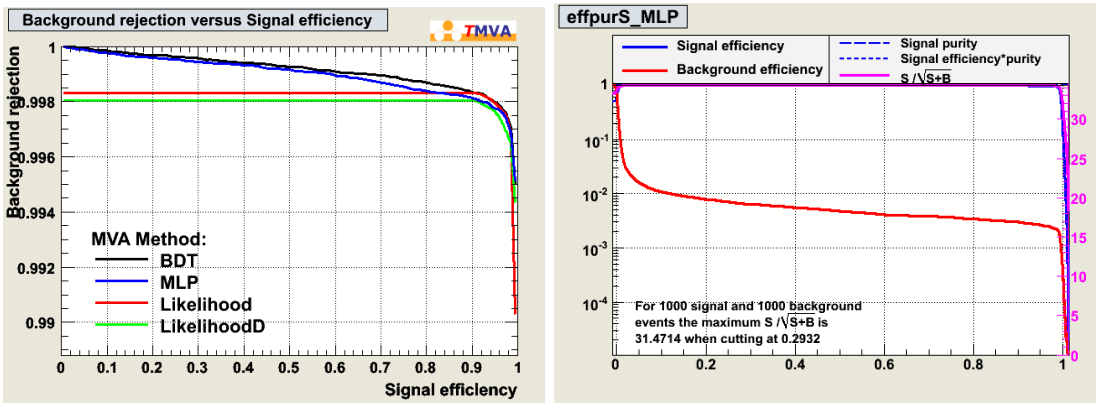

Figure 5.2: Left: Muon selection efficiency vs purity distribution from TMVA. We used the MLP output for muon identification. Right: Efficiency for the MLP optimisation cut.

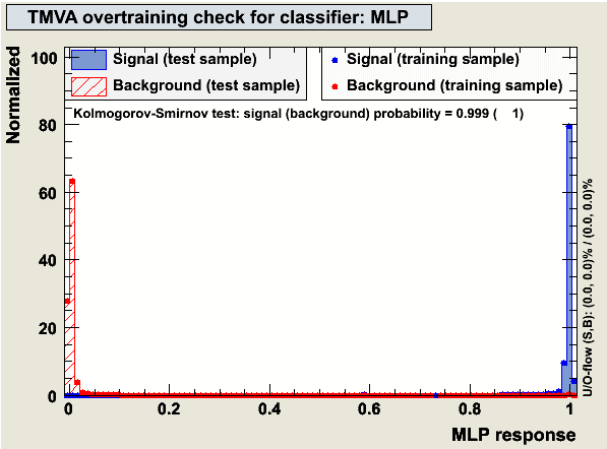

Figure 5.3: Overtraining check.

5.3 Initial-State Radiation

Initial-state radiation (ISR), as discussed in chapter 3, can be a considerable source of degradation of beam energy. Most of the ISR photons have very low transverse momentum and low energy, and fall outside the detector acceptance. The ISR photons that reach the detector are very difficult to distinguish from photons arising from bremsstrahlung of the final state particles. To select ISR photons we used the PFOID algorithm in MarlinReco [82] with the following cuts: energy of the photon $E_\gamma > 5$ GeV, transverse momentum of the photon $p_{T\gamma} < 3$ GeV and no other particle object within 10° around the photon direction. In a sample of 5000 generated $\mu^+\mu^- H$ events, 95 ISR photon candidates were found, of which 45 photons were matched with the generated ones.

5.4 Reconstruction of the Z boson

We reconstructed Z boson candidates by combining a pair of oppositely charged tracks identified as muons. Neural Networks were used to identify the tracks with momentum $p > 20$ GeV and no other track within an angle of 5° around the track direction, as muons. If more than one candidate was found, the one with the reconstructed mass closest to the Z boson nominal mass, $M_Z = 91.2$ GeV, was taken. We obtained 4284 $\mu^+\mu^- H$ and 50994 background events from the date samples given in table 5.1. Figure 5.4 show the distributions of the reconstructed

di-muon mass and the recoil mass as defined in equation 5.2, respectively.

$$M_H^{recoil} = \sqrt{s - 2\sqrt{s}.E_{l^+l^-} + M_{l^+l^-}^2} \tag{5.2}$$

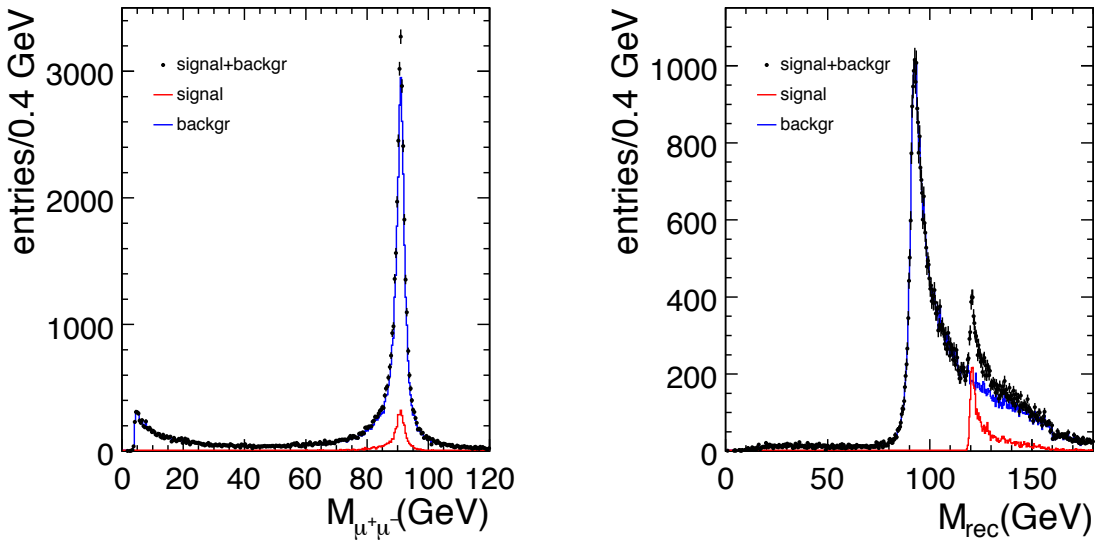

Figure 5.4: Left: Di-muon invariant mass distribution. Right: Recoil mass distribution.

5.5 Jet Finding and Higgs boson Reconstruction

Particles identified as muons and used to reconstruct Z bosons and the ISR photons (if found) are removed from the full reconstructed particle collection. Remaining particles are then forced into two jets using the Durham algorithm as described in section (4.4). Each jet gets a momentum which is the sum of all of the constituent particles. The two jets are combined into a Higgs candidate. The di-jet mass distribution is shown in Figure 5.5. Figure 5.4 and 5.5 attempts to reconstruct the mass of the Higgs candidate. It is noticed that the recoil mass distribution gives a better reconstruction of the Higgs mass as it involves initial

parameter such as the center-of-mass energy, $\sqrt{s}$, which is well defined for the ILC. The other variables, mass and energy of the di-muon system, are also well reconstructed. On the other hand, limitation on the jet energy resolution restricts the reconstruction of di-jet mass, M_{jj}.

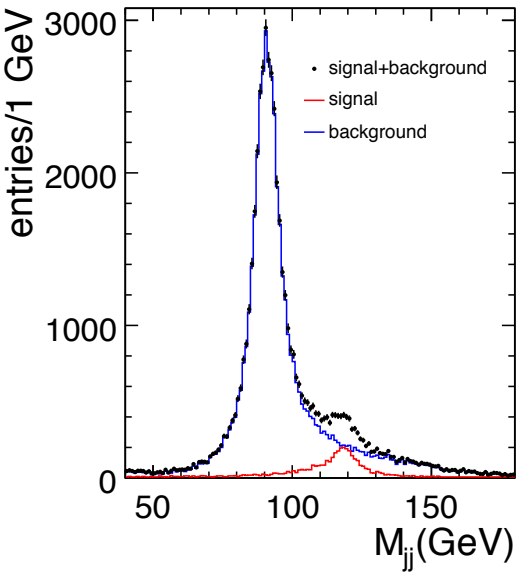

Figure 5.5: Di-jet mass distribution for signal and background.

5.6 Event Pre-Selection

To suppress the background contribution from the non-hadronic Higgs decay modes, in particular the $\tau^+\tau^-$ mode, and from processes with two or four leptons in the final states, only events with 25 reconstructed particle objects or more are accepted. Only events with one Z boson candidate and one reconstructed Higgs boson candidate are accepted, further reducing the contribution from $q\bar{q}$ production. After pre-selection the number of signal events was 3327 and of background was 31123. These numbers correspond to the luminosity 292 fb^{-1}.

5.7 Cut-Based Selection

5.7.1 Selection Variables

The selection variables are defined as:

- **Di-Muon Mass** The invariant mass of $\mu^+\mu^-$ pairs found.
- **Di-Jet mass** The invariant mass of the two jets found by the jet finder.
- **Thrust** The thrust of the particles assigned to the jets. This is calculated in the laboratory frame. The thrust is defined as

$$T = \max_{|\vec{n}|=1} \frac{\Sigma_i |\vec{n} \cdot \vec{p_i}|}{\Sigma_i |\vec{p_i}|} \tag{5.3}$$

  with $\vec{n}$ being unit vector to give maximum value. T can have a value between 1/2 and 1, depending on how linear or isotropic the jet is.
- **Cos(θ_{Thrust})** of the primary thrust axis.
- **Cos** θ_Z of the Z candidate, from the sum of the four momenta of the $\mu^+\mu^-$ pair.
- **Recoil Mass, (M_{rec})** The recoil mass of the muon system. The recoil energy is assumed to be 250 GeV, and the center of mass frame is assumed to be the laboratory frame.
- **Constraint Di-jet Mass** The jets and muon four momenta are fitted with the constraints of having a total four momentum of p^μ (250, 0, 0, 0) GeV, and a di-lepton mass of the Z mass. The invariant mass of the two jets is then taken as the fitted di-jet mass.
- **Jet energy difference** ($|E_{jet1} - E_{jet2}|$) The difference between the energies of the two jets found by the jet finder.

5.7.2 Cuts

Events are required to have the following properties to be considered for further analysis. Figure 5.6 shows distributions of these variables for signal and background.

- 70 GeV $< M_{\mu^+\mu^-} <$ 110 GeV.
- 100 GeV $< M_{jj} <$ 140 GeV.
- 117 GeV $< M_{rec} <$ 150 GeV.
- $|\cos(\theta_Z)| < 0.9$

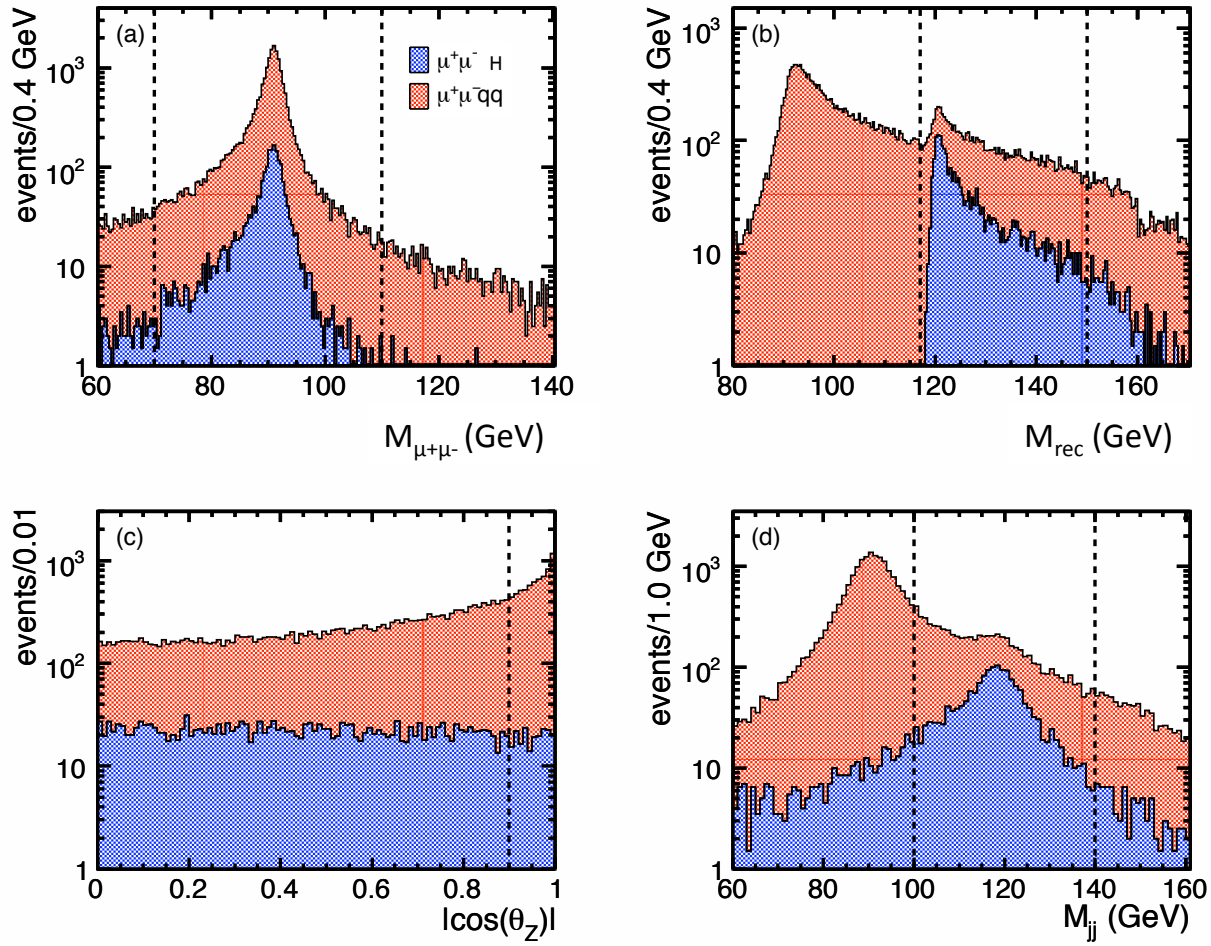

Figure 5.6: Stacked histograms showing distributions of the variables used in the event selection of the muon sample for both signal (blue) and background (red): (a) di-muon invariant mass distribution, (b) recoil mass, (c) polar angle distribution of the di-muon pair and (d) di-jet mass distribution. The dashed lines show the cuts applied.

Table 5.2: Number of selected event for signal and background samples for a luminosity of 250 fb^{-1} with beam polarisation, $P(e^+, e^-) = (+30\%, -80\%)$.

Cuts	$\mu^+\mu^- H$	$\mu^+\mu^- q\bar{q}$
Initial	2202	24003
$N_{particles} > 25$	1957	23132
70 GeV $< M_{\mu^+\mu^-} <$ 110 GeV	1880	18133
100 GeV $< M_{jj} <$ 140 GeV	1767	4270
117 GeV $< M_{rec} <$ 150 GeV	1617	3481
$\lvert\cos\theta_Z\rvert < 0.9$	1371	1665
Efficiency	$(62.26 \pm 1.03)\%$	$(6.93 \pm 0.16)\%$

In each case the cuts were chosen to maximise $\frac{S}{\sqrt{(S+B)}}$. Starting with an initial loose set of cuts, $\frac{S}{\sqrt{(S+B)}}$ is calculated for different cut values. The cut on the variable that offers the best improvement in $\frac{S}{\sqrt{(S+B)}}$ is then tightened to that value and process repeated.

An exception was made for the lower cut on the di-muon mass, $M_{\mu^+\mu^-} > 70$ GeV which does not provide the optimum value of $\frac{S}{\sqrt{(S+B)}}$. A tighter cut was found to reduce the number of $H \to c\bar{c}$ to a level detrimental to the branching ratio extraction. In addition, there was no cross-contamination observed between electron and muon samples.

5.8 Branching Ratio Fitting

The extraction of the branching ratios described here follows the procedure used in [77]. The reconstructed jets were submitted to vertex reconstruction and flavour tagging using the LCFIVertex package [83]. To each jet a value for the b-tag, c-tag and bc-tag is assigned as explained in chapter 4.

For each event the b-likeness and c-likeness is calculated from the b-flavour tag and c-flavour tag information. The b/c-likeness are:

$$X_i = \frac{X_1 \cdot X_2}{X_1 \cdot X_2 + (1 - X_1) \cdot (1 - X_2)} \tag{5.4}$$

where X_i is c- or b-flavour likeness. X_1 and X_2 are the b/c-tag neural net

outputs of the first and second jets respectively. This variable requires both jets to have a high b- or c-tag value for an event to have a high b-flavour likeness or c-flavour likeness.

A template fitting method is then used to extract the branching ratios. Independent Monte Carlo samples passing the same event reconstruction and selection as the "data" samples are used to build the four two-dimensional distributions of b-likeness versus c-likeness for each of the Higgs boson hadronic decay modes ($H \to b\bar{b}, H \to c\bar{c}, H \to gg$) and for the background (everything else). These templates are then fitted to the simulated data distribution. Figure 5.7 shows the four Monte Carlo templates and the simulated data.

The branching ratios are extracted by minimising the χ^2 function

$$\chi^2 = \frac{\sum_{ij}(N^{ij}_{data} - f\sum_s r_s N^{ij}_s)^2}{\sigma^2_{ij}} \tag{5.5}$$

where $\sigma^2 = N^{ij}_{data} + f^2\Sigma_s N^{ij}_s$ takes into account the limited statistics of the Monte Carlo samples, N^{ij} is the number of events in the bin (i, j) of the distributions, $f = 0.217$ is the luminosity used to generate the simulated data divided by the luminosity of the Monte Carlo samples, r_s are the parameters obtained from the fit and correspond to the b/c-likeness distribution, where $s = bb, cc, gg, bkg$.

The measured quantities, cross sections times branching ratio, are calculated from the fitted parameters r_s according to:

$$\sigma(e^+e^- \to HZ) \times BR(H \to s) = r_s \times BR(H \to s)_{SM} \times \sigma(e^+e^- \to HZ)_{SM} \tag{5.6}$$

where SM denotes the Standard Model cross section or branching ratio.

In the Standard Model $r_s = 1$ by definition for $b\bar{b}, c\bar{c}$ and gg. Templates are made of $H \to b\bar{b}$, $H \to c\bar{c}$ and $H \to gg$ decays. All other Higgs decays are put into background to simplify our calculation, fixing the parameter $r_{bkg} = 1$. This is well justified using the fact that the dominant non-hadronic backgrounds, $H \to W^+W^-, H \to ZZ$ and $H \to \tau^+\tau^-$, can all be measured separately with negligible cross contamination from hadronic deays using final state leptons (see [84] for $H \to W^+W^-$) and therefore they are assumed known in this analysis. Figure 5.7 shows the template and data distributions.

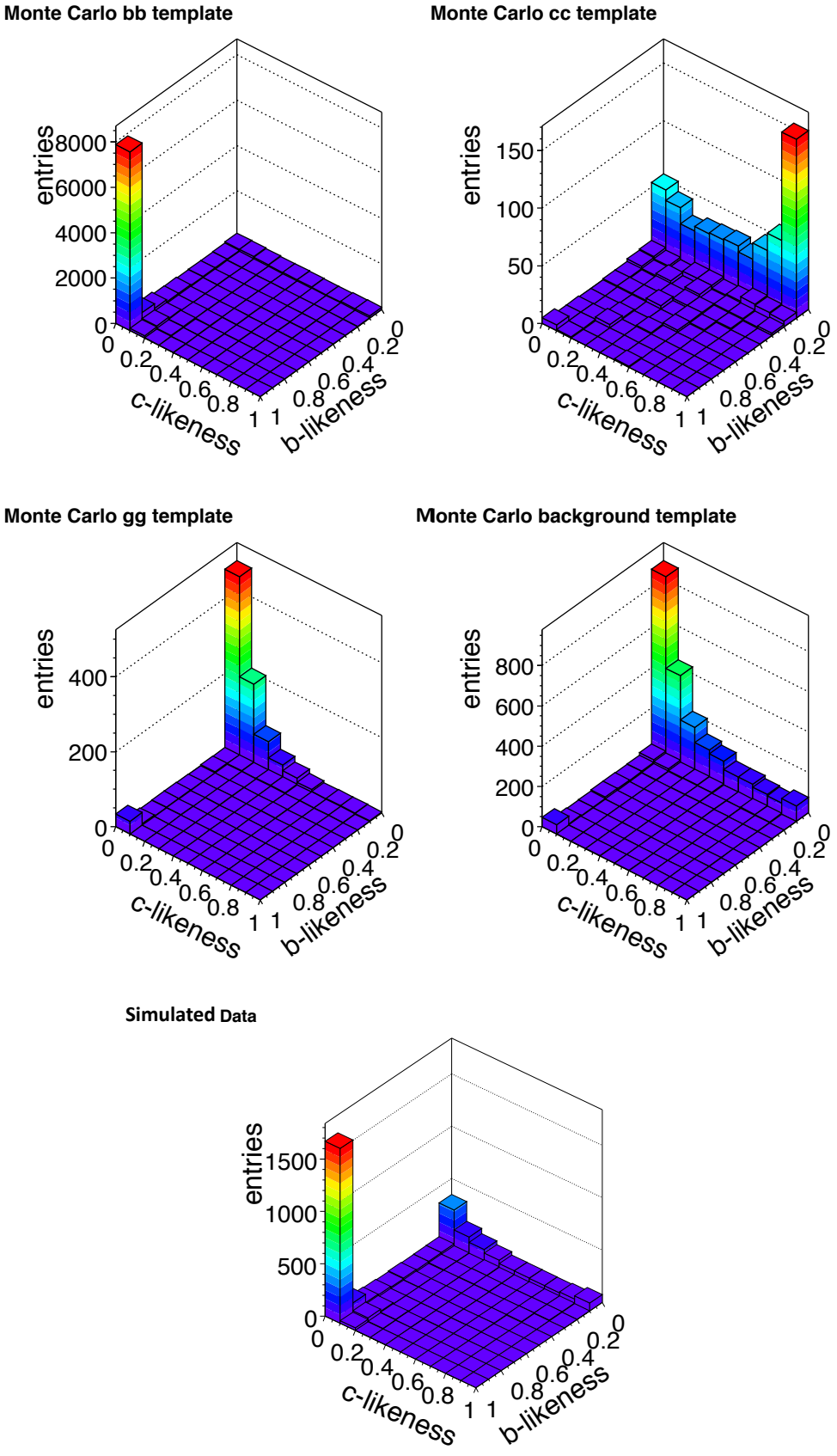

Figure 5.7: Distribution of b-likeness versus c-likeness for the Monte Carlo templates and simulated data.

5.9 Fit Results

The statistical errors obtained for the measurement of $\sigma \times BR(H \to X)$ using a simultaneously fit on the muon channel are 4% ($H \to b\bar{b}$) , 46% ($H \to c\bar{c}$) and 45% ($H \to gg$) for a 120 GeV Higgs mass at $\sqrt{s} = 250$ GeV and luminosity 250 fb^{-1}.

$$\begin{aligned} \frac{BR(H \to b\bar{b})}{BR(H \to b\bar{b})_{SM}} &= 1.00 \\ \frac{BR(H \to c\bar{c})}{BR(H \to c\bar{c})_{SM}} &= 0.87 \\ \frac{BR(H \to gg)}{BR(H \to gg)_{SM}} &= 0.93 \end{aligned}$$

The corresponding fit errors are:

$$\begin{aligned} \Delta\frac{BR(H \to b\bar{b})}{BR(H \to b\bar{b})_{SM}} &= 4\% \\ \Delta\frac{BR(H \to c\bar{c})}{BR(H \to c\bar{c})_{SM}} &= 46\% \\ \Delta\frac{BR(H \to gg)}{BR(H \to gg)_{SM}} &= 45\% \end{aligned}$$

For our analysis we had a very limited sample for $c\bar{c}$ compared to $b\bar{b}$ which give large Poisson fluctuations in the errors.

5.10 Discussion

Combined Results Independent studies for other Z decay channels were also conducted for the ILD Letter of Intent. For this purpose the Higgs branching ratio results for other Z decay channels are combined with the muon channel. The combined results are summarised in table 5.3. An uncertainty on the total cross section of $e^+e^- \to ZH$ is expected to be 5% [86]. This value is obtained by performing a study on the Model Independent analysis which is added in quadrature for the combined results in table 5.3. The precision achieved in this analysis and the combined results for different Z decay modes demonstrate the

general purpose nature of the ILD.

Channel	$Br(\mathrm{H} \to \mathrm{b\bar{b}})$	$Br(\mathrm{H} \to \mathrm{c\bar{c}})$	$Br(\mathrm{H} \to gg)$
$\mathrm{ZH} \to \mathrm{q\bar{q}c\bar{c}}$	–	$(30 \oplus 5)\,\%$	–
$\mathrm{ZH} \to \nu\bar{\nu}H$	$(5.1 \oplus 5)\,\%$	$(19 \oplus 5)\,\%$	–
$\mathrm{ZH} \to \ell^+\ell^-\mathrm{q\bar{q}}$	$(2.7 \oplus 5)\,\%$	$(28 \oplus 5)\,\%$	$(29 \oplus 5)\,\%$
Combined	5.5 %	15 %	29 %

Table 5.3: Precision for the Higgs boson branching fraction for different Z decay channels and combined results at $\sqrt{s} = 250$ GeV [50].

Analysis Improvements Progress in the detector model and the software can refine the analysis significantly. Improvements in flavour tagging can be achieved by re-examining the jet finding. In jet finding, we force particles into a jet which sometime don't belong to that jet. It could affect the energy of the reconstructed jet. A scaling of the flavour tag variables to the reconstructed jet energy can minimise these effects but a study of these effects is beyond the scope of this thesis. For signal and background separation, we used only cut based method. An improvement can be achieved by using the TMVA likelihood method as explained in section 5.11.

Error Analysis To investigate the experimental systematics, a very good understanding of the detector performance is needed. This investigation and a good understanding of the SM backgrounds is not in the scope of this study. The errors for $H \to c\bar{c}$ and $H \to gg$ are certainly statistics limited. For systematic uncertainties, a very good understanding of the detector performance and response is needed. It is believed that it is possible to achieve a systematic uncertainty of 1% for the $b\bar{b}$ channel based on the fact that there will be manifold possibilities for calibration and cross checks. [77].

5.11 Future Enhancement in Signal Selection

Likelihood Method

A selection of events based on the likelihood method implemented in TMVA was used in order to achieve better separation of the signal and the background but due to lack of time this was not completed and not implemented in the analysis. However, a future study of the Higgs branching ratio can include this neural network based selection and get an improvement in the selection efficiency of the signal and background rejection. The input variables were $M_{jj}, E_{\mu^+\mu^-}, |\cos(\theta_Z)|$, thrust of the hadronic system, difference of the two jets energies, $|E_{j1} - E_{j2}|$, and $|\cos(\theta_{thrust})|$. Figure 5.8 shows the distributions of signal and background of the separation variables. The cut on the likelihood was optimised to maximise

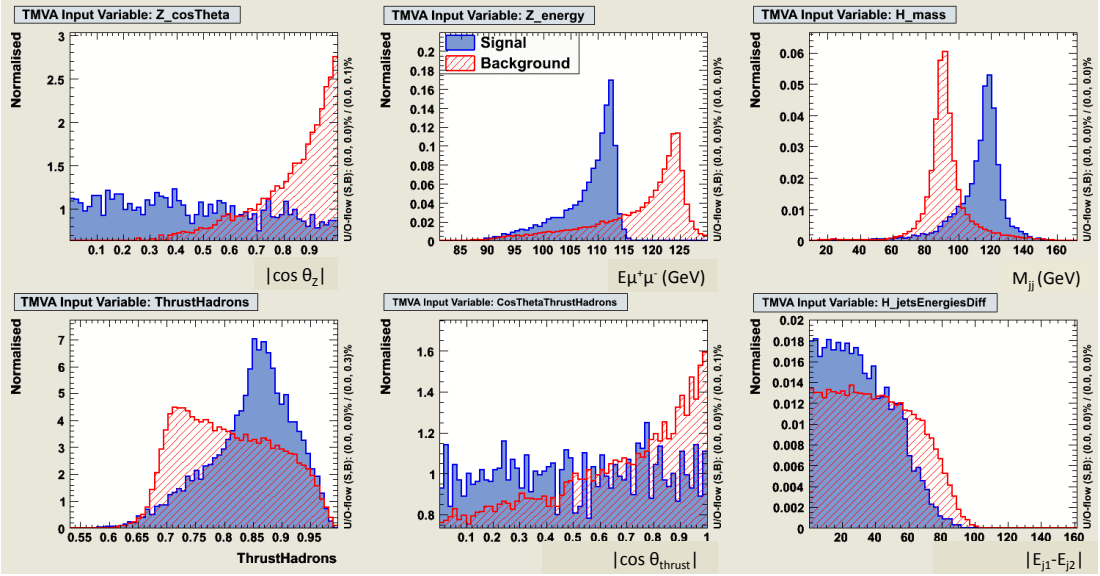

Figure 5.8: The input distributions used in the likelihood selection. Here signal is $\mu^+\mu^- H$ and background is $\mu^+\mu^- q\bar{q}$.

$\frac{S}{\sqrt{(S+B)}}$. This selection left us with 81.9% signal and 7.7 % background events (compared with 62.26% signal and 6.93% background events with the cut based selection method). Figure 5.9 shows the recoil mass distribution before and after applying the likelihood selection cuts.

These results show that a factor of 4/3 improvement in the selection efficiency of the signal can be attained by implementing the TMVA likelihood method in

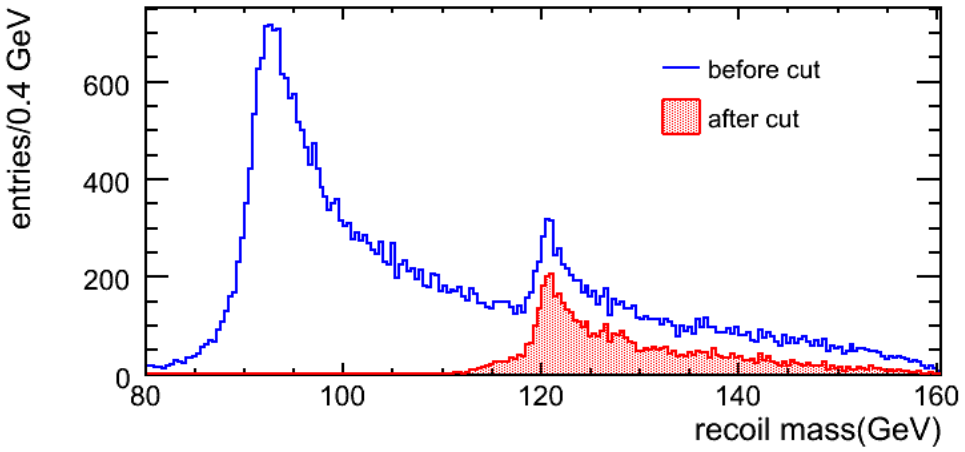

Figure 5.9: The recoil mass distribution before and after applying the likelihood cuts as discussed in section 5.11.

the Higgs branching ratio analysis.

Chapter 6

Top Higgs Yukawa Coupling Analysis

6.1 Overview

This chapter presents the analysis which the author carried out on the $t\bar{t}H$ process. References [89] and [91] have performed earlier feasibility studies of the top-Higgs Yukawa coupling via the process $e^+e^- \rightarrow t\bar{t}H$ at a linear collider and in [88], an analysis was performed at 800 GeV center-of-mass energy. We perform a complete analysis of the process for the Higgs with mass 120 GeV and the channel where one W boson from the top quark decay, $t \rightarrow bW$, decays as $W \rightarrow l\nu$ and the other as $W \rightarrow q\bar{q}$. The full reconstruction of the final state was conducted by reconstructing one hadronic and one leptonic W decays. Top quarks and the Higgs boson were then reconstructed from W's and b jets. Missing energy reconstruction has a large impact on the reconstruction of the semi-leptonic channel, and b-tagging has a crucial role in separating signal and background. The analysis is carried out for an integrated luminosity, L, of 1000 fb^{-1} at $\sqrt{s} = 500$ GeV. At this center of mass energy and L, the main background process is $t\bar{t}$.

6.2 Monte Carlo Samples

The analysis was performed with the samples provided by the ILD optimisation group. The samples were generated at SLAC using WHIZARD, and then

simulated and reconstructed on the DESY Grid nodes. The GEANT4 based Mokka package was used for simulation in the ILD-00 detector model, which is the first simulated reference model of ILD. Reconstruction was performed using MarlinReco, PandoraPFA and LCFIVertex with the versions supplied in ILCInstall v01-07 as described in chapter 4.

The signal used is $e^+e^- \to t\bar{t}H$ at $\sqrt{s} = 500$ GeV, where t decays with 100% into a b-quark and a W, and Higgs are allowed to decay according to the Standard Model branching ratios. The signature of the process $e^+e^- \to t\bar{t}Z$ and its cross section are very close to those of the signal. The process $e^+e^- \to t\bar{t}$ has a rather large cross section and could mimic the signal. In table 6.1, the sample sizes used in the analysis for $\sqrt{s} = 500$ GeV are shown. Note that $e^+e^- \to t\bar{t}$ has two leptons and two light jets in final state. Time constraints compelled us to include only this final state in our study. Inclusion of this final state will change the results of this study to some extent. We had intended to extend this study for all signal and background channels.

Table 6.1: Cross section and luminosity for signal ($t\bar{t}H$) and different background processes.

Process	σ (fb)	Sample size	Luminosity (ab^{-1})
$e^+e^- \to t\bar{t}H$	0.576	20000	34
$e^+e^- \to t\bar{t} \to l\nu q\bar{q}$	230	400000	1.7
$e^+e^- \to t\bar{t}Z$	0.58	24000	41

6.3 Semi-Leptonic Channel

For our analysis we selected the semi-leptonic channel of the signal process in which both top quarks decay into a W and a b-quark, and one W bosons decays into a charged lepton and a neutrino and the other one decays into light jets. The final state in this channel has 6 jets among which four are b-jets and two light jets, j, plus one charged lepton, l, and missing energy for ν. The final state follows from the process:

$$e^+e^- \to t\bar{t}H \to W^+bW^-\bar{b}b\bar{b} \to l\nu 2j4b \tag{6.1}$$

The effective branching ratio with the Standard Model values [12] is given:

$$\begin{aligned} BR(t\bar{t}H \to l\nu 2j4b) &= 2 \star BR(H \to b\bar{b}) \star BR(W^{\pm} \to 2j) \star BR(W^{\pm} \to l\nu) \\ &= 30\% \end{aligned}$$

Figure 6.1, shows the branching fraction for different final states of the W^+W^- in $t\bar{t}H$. Although the hadronic final state has a larger branching ratio compared to the semi-leptonic state, it is difficult to reconstruct due to the presence of 8 jets in the final state. The leptonic final state has two charged leptons which can be reconstructed efficiently but two neutrinos posses difficulty in reconstructing the full final state. Moreover, the branching ratio is very small for this channel.

In selecting the semi-leptonic channel, we have filtered out τ leptons as they are difficult to reconstruct and identify with an optimal efficiency. This reduces further the signal efficiency to $\sim$ 20%. There are 20,000 initial events from which we select the semi-leptonic channel filtering to 4,400 events $\sim$ 22% of the signal events. There are 3% badly reconstructed events which passed the filtering process which are easily removed by imposing the condition on the lepton number > 0 in an event, leaving 3860 events $\sim$ 19.3%.

6.4 Lepton Identification

The first step of the analysis is to select events with a topology compatible with that of the signal. We need an efficient lepton identification for reconstruction of the final state. In MarlinReco, there was no reconstruction of hits in muon detector. We thus only use calorimeter and tracking information for muon identification. The selection of a lepton is based on the cuts obtained by studying single particle MC samples (same samples used for the muon identification in section 5.2).

In the analysis presented in chapter 5, the identification of muons is performed by using the NN approach. A cut based selection study is conducted at the same time for the identification of both electrons and muons. In the current top Higgs Yukawa coupling analysis, we have used the cut based selection.

We generate these single particle samples of 10,000 events each using the Generic built-in GEANT4 Particle Gun package [90]. The energies of these generated particles are between 50 and 65 GeV. Five single particle samples

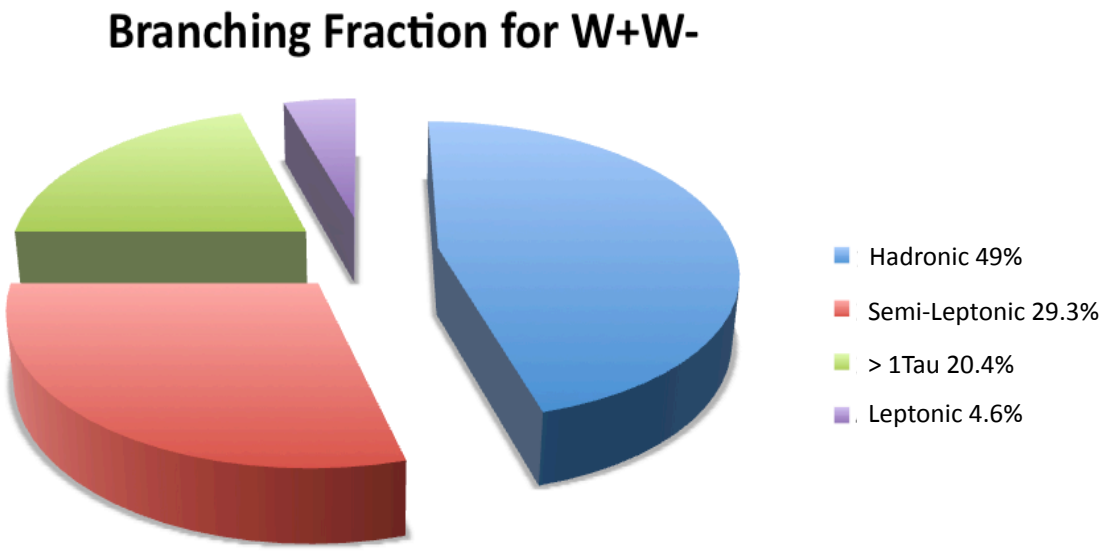

Figure 6.1: Branching fractions for W^+W^- in $t\bar{t}H$ events.

are generated: muons ($\mu^{\pm}$), pions ($\pi^{\pm}$), electrons ($e^{\pm}$), kaons ($K^{\pm}$) and protons ($p, \bar{p}$). The most important variables we investigate are:

- Reconstructed energy in Electromagnetic calorimeter, E_{ECal}
- Reconstructed energy in Hadronic calorimeter, E_{HCal}
- Ratio of the energy in Electromagnetic calorimeter and the Total energy, E_{ECal}/E_{Tot}
- Ratio of Total energy and momentum, E_{Tot}/P

These variables, E_{Tot}, E_{ECal}/E_{Tot}, E_{HCal}/E_{Tot} and the E_{Tot}/P are shown in figure 6.2.

We examine the behaviour of the particles in the individual sub-detectors: tracking detector, calorimeters, vertex detectors and TPC Tracker. To decide the selection cuts for the identification of the electron and muon, we analyse efficiencies for different cut variables. The efficiencies vary with the values of the cut applied. For example in figure 6.3, the top center plot shows the efficiency changes as the result of varying the upper cut on E_{ECal} listed in table 6.2.

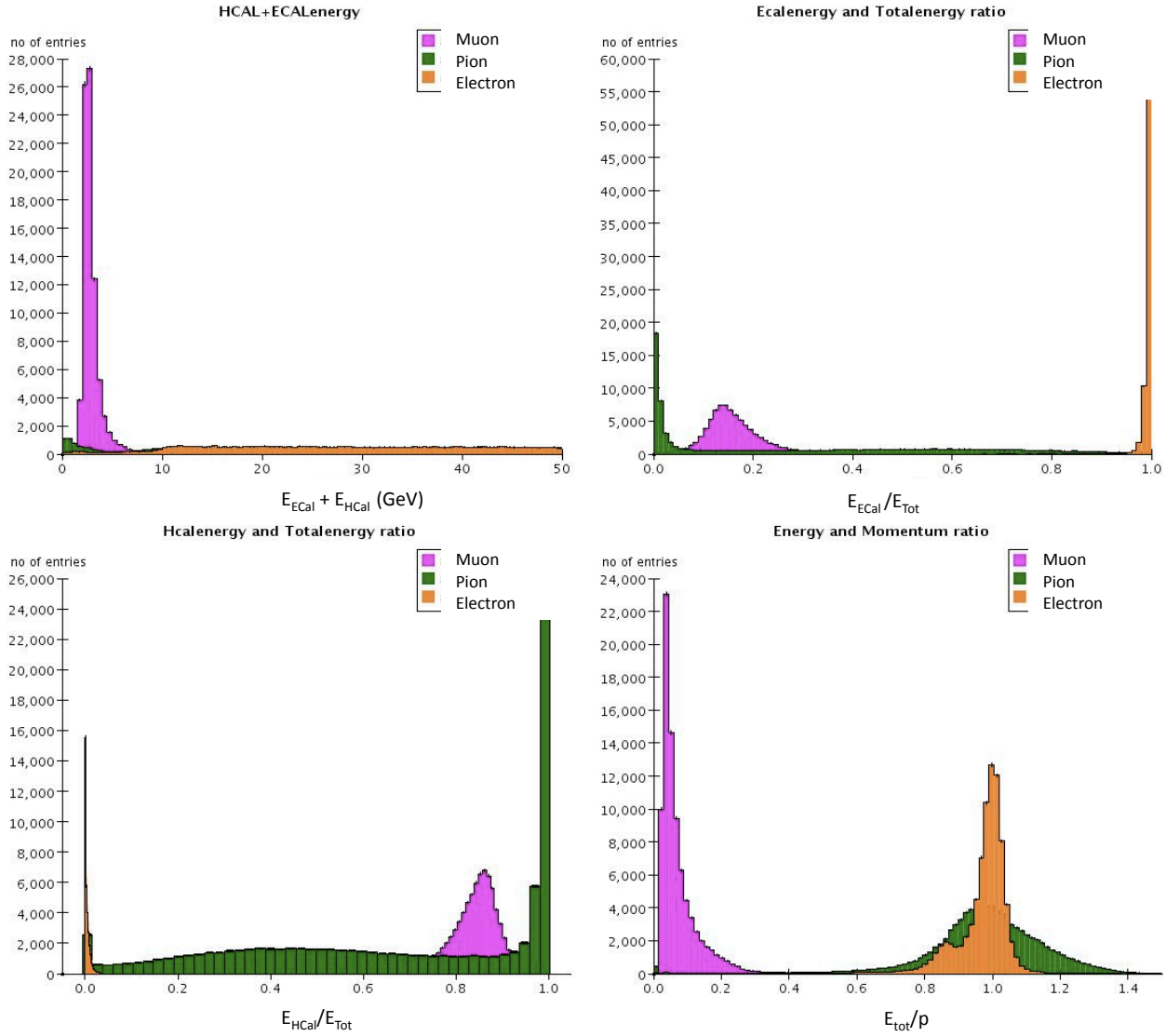

Figure 6.2: E_{Tot} (Top left), E_{ECal}/E_{Tot} (Top right), E_{HCal}/E_{Tot} (Bottom left) and E_{Tot}/P (Bottom right) for single particle MC samples. Pink is for muons, green is for charged pions and orange is for electrons.

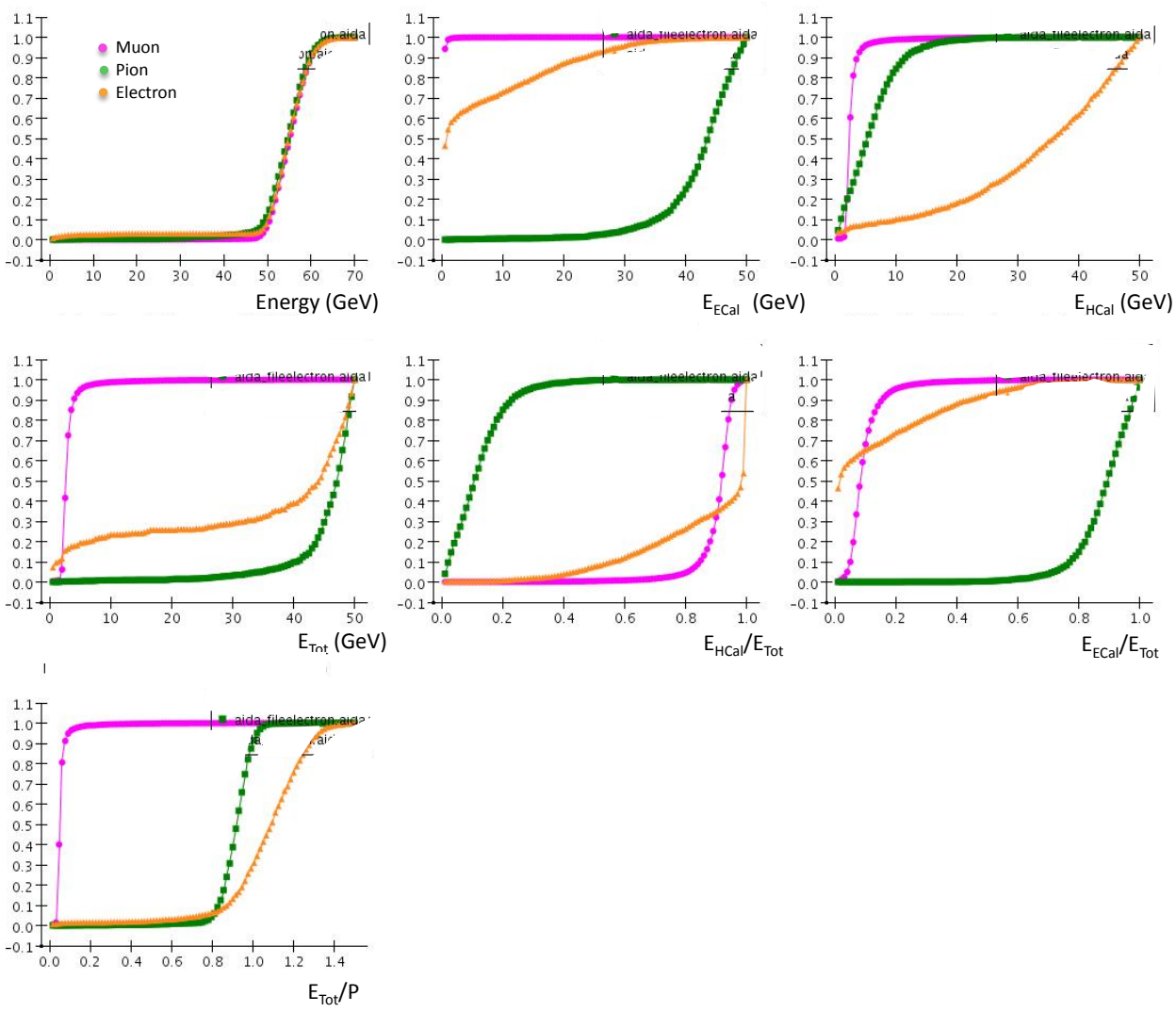

Figure 6.3: Efficiency for individual lepton selection cuts using single particle MC samples. The x-axes shows the relevant variables and the y-axes shows their efficiencies.
Top row left to right: Cut on tracking momentum, Upper cut on E_{ECal}, Upper cut on E_{HCal}.
Middle row left to right: Cut on E_{Tot}, Cut on E_{HCal}/E_{Tot}, Cut on E_{ECal}/E_{Tot}.
Bottom row: E_{Tot}/P.
Pink is for muons, green is for charged pions and orange is for electrons.

After examining the plots in figure 6.3 we chose the following cuts for Muon and Electron identification:

Table 6.2: Cuts for muon and electron identification.

Variable	Muon Cut	Electron Cut
Momentum	20GeV $< P <$ 100 GeV	20GeV $< P <$ 100 GeV
E_{ECal}	< 2.5 GeV	> 32 GeV
E_{HCal}	< 15 GeV	< 15 GeV
E_{ECal}/E_{Tot}	< 0.5	> 0.6
E_{Tot}/P	< 0.3	> 0.7

The overall efficiencies of the Muon cuts are:

- $\epsilon^{(\mu)}_{Muon} = 98.8\% \pm 0.7\%$
- $\epsilon^{(\mu)}_{Pions} = 3.4\% \pm 1.3\%$
- $\epsilon^{(\mu)}_{Electron} = 0^{+0.01}_{-0}\%$

Similarly the overall efficiencies of the Electron cuts are:

- $\epsilon^{(e)}_{Electron} = 97.7\% \pm 0.1\%$
- $\epsilon^{(e)}_{Pions} = 0.80\% \pm 0.13\%$
- $\epsilon^{(e)}_{Muon} = 0^{+0.01}_{-0}\%$

6.5 Lepton Selection and Jets Finding

We apply the cuts obtained from the single particle sample study on the PFOs (section 4.2) in the $t\bar{t}H$ sample to identify leptons. Figures (6.4) shows the resolution of the reconstructed three momentum of selected leptons. It should be noted that we consider only electrons and muons as the lepton candidates, as tau's are difficult to reconstruct and identify.

Once we select the leptons, we remove them from our sample and force the remaining particles into 6 jets by using the JETFinder algorithm (see section 4.4). The LCFIVertex reconstruction is performed on the jets afterwards.

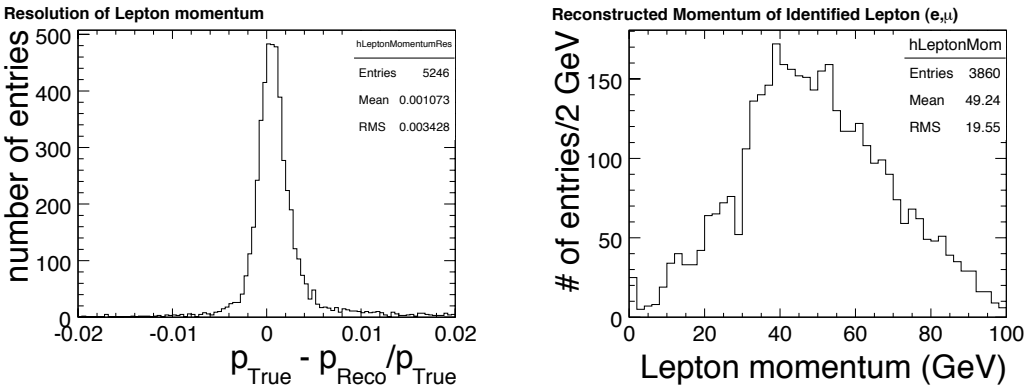

Figure 6.4: Charged leptons. Left: Momentum resolution, $(p_{True} - p_{Reco})/p_{True}$. Right: Momentum p_{Reco}.

6.6 Reconstructing Missing Momentum

In the semi-leptonic channel, there is missing momentum due to the presence of a neutrino. The reconstruction of this missing momentum summed over all the particles, i, in the event.

$$p_x^{miss} = -\Sigma_i p_{xi}, \quad p_y^{miss} = -\Sigma_i p_{yi}, \quad p_z^{miss} = -\Sigma_i p_{zi} \tag{6.2}$$

The transverse component of the the neutrino momentum is equal to the corresponding component of the missing energy in the event, defined as:

$$p_T^{miss} = \sqrt{(p_x^{miss})^2 + (p_y^{miss})^2} \tag{6.3}$$

Figure 6.5 shows the reconstruction of the transverse component of the missing momentum. Comparing the transverse component and the z-component, the resolution for p_z is slightly worse compared to p_T as shown in right figure 6.6 but far better than at the LHC. This is a motivation and an advantage of the ILC that the z-component of momentum is well reconstructed compared to the LHC.

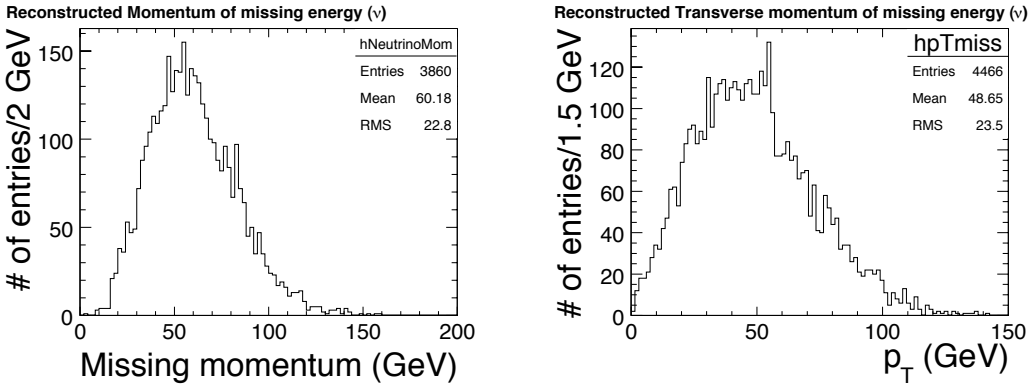

Figure 6.5: Missing energy. Left: Reconstructed momentum of the missing energy. Right: Transverse component of missing momentum.

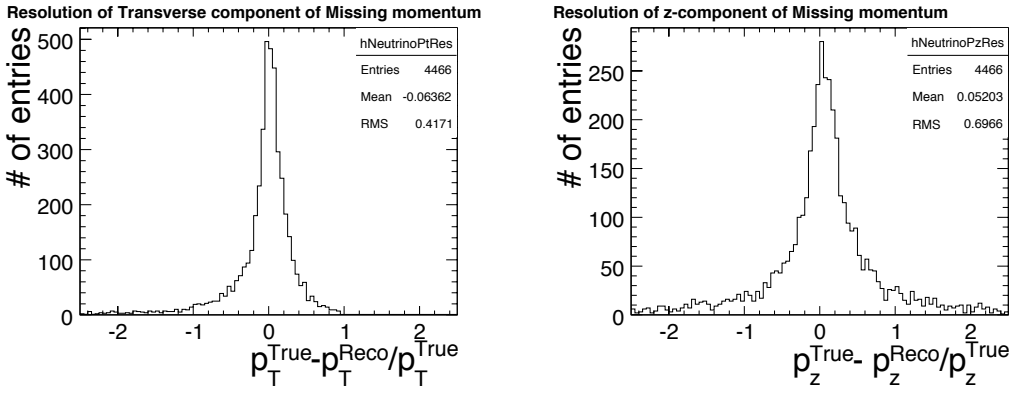

Figure 6.6: Missing momentum resolution, $(p^{miss}_{True} - p^{miss}_{Reco})/p^{miss}_{True}$. Left: Transverse component. Right: z-component.

6.7 Pre-Selection

Once leptons are identified, only those events are selected which have at least one charged lepton (electron or muon). If there are more than one electron or muon in the event, then the charged lepton with highest momentum is selected to reconstruct the final state. Remaining leptons are included in the reconstructed jets.

6.8 Reconstruction of Semi-Leptonic W

Compared to the LHC where the complete reconstruction of $W \rightarrow l\nu$ is limited by the impossibility of reconstructing fully the neutrino four-momentum, at a linear collider it is possible to fully reconstruct the semi-leptonic W. The W boson mass can be reconstructed using equation:

$$M_W = \sqrt{(E_\nu + E_l)^2 - (p_{\nu x} + p_{lx})^2 - (p_{\nu y} + p_{ly})^2 - (p_{\nu z} + p_{lz})^2} \tag{6.4}$$

In the left figure 6.7, the reconstructed mass of the W candidate, given in equation 6.4, is shown. Equation 6.4 is also used to combine the truth information of the charged lepton and missing energy to get the mass of W as shown in the right figure 6.7. In this plot, some events are in the lower W mass range due to the linking processor used to get the truth W mass. In this processor, the reconstructed and true particle are linked. In some of the events, this linking is not effective as it matches a wrong true particle with the reconstructed one, having a lower momentum. The combination of wrong true particles gives a smaller W mass as shown in the right figure 6.7. The width of the distribution is the natural width of the W boson.

The z-component of the missing momentum can be reconstructed at ILC far better than at the LHC, therefore, it is worth calculating the transverse mass of W-boson and compare with the full reconstructed mass. The reconstructed transverse mass of W boson and the true transverse mass of W boson in figure 6.8 are given by the equation:

$$M_{WT} = \sqrt{2p_T^l p_T^\nu (1 - \cos(\phi^l - \phi^\nu))} \tag{6.5}$$

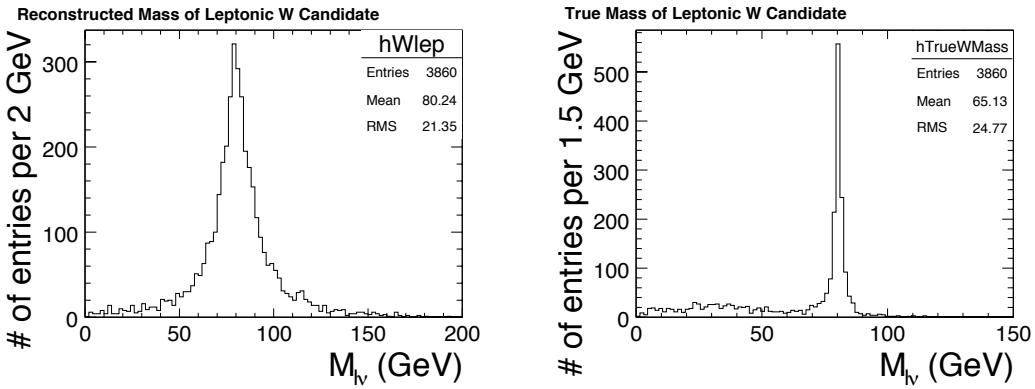

Figure 6.7: Mass of W candidate combining lepton and missing energy as defined in equation 6.4. Left: using reconstructed information. Right: using truth information.

where p_T^l and p_T^ν are the transverse momentum of the reconstructed lepton and missing energy respectively, while ϕ^l and ϕ^ν are the polar angles of lepton and missing energy with the z-axis.

In the figure 6.8, the reconstruction of transverse mass is compared with the true transverse mass. Both distributions have same shape but the reconstructed transverse mass has more events for lower values. It is due to the uncertainty in the reconstruction of x- and y-components of both missing momentum and the lepton.

6.9 Reconstruction of Hadronic W

Jets passing the LCFIVertex reconstruction are sorted according to their b-tag value. These four jets with the highest b-tag value are considered as the b-jets and the two with the lowest b-tag value are considered as the light jets. Hadronic W candidates are created from pairs of light-jets in the event. Right figure 6.9 shows the distribution of the Hadronic W reconstructed mass where we see a very wide range of the distribution. The b-tag of all six jets is examined as shown in left figure 6.10 and it is noticed that in an event not all four b-jets have a very high b-tag value. Sometime the value of jet three and four is very close to the b-tag value of jets tagged as light jets. Therefore, reconstruction of W by using this method of sorting is not always effective. There is a possibility that a wrong

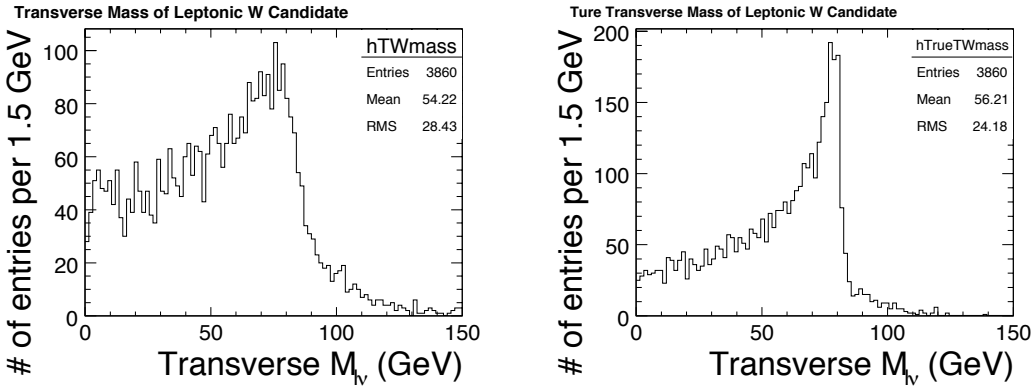

Figure 6.8: Transverse mass of W candidate combining lepton and missing energy as given in equation 6.5. Left: using reconstructed information. Right: using truth information.

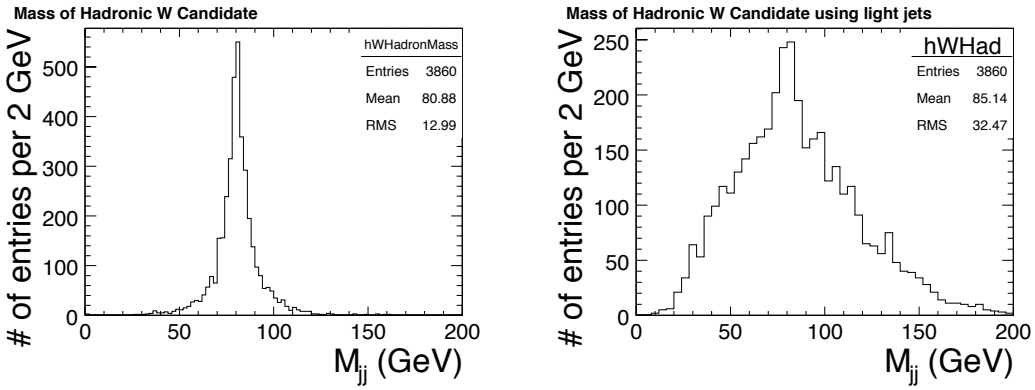

Figure 6.9: Reconstructed Mass of W combining light di-jet pair using two methods as explained in section 6.9.
Right: W mass reconstructed by combining the light di-jet pair which are selected according to the lowest value of b-tag.
Left: W mass reconstructed by combining the light di-jet pair (with b-tag > 0.09) which gives mass closest to the W mass.

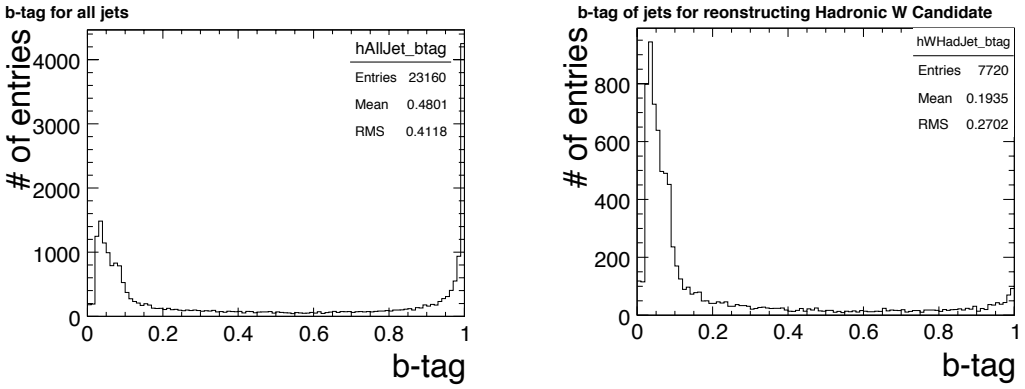

Figure 6.10: Left: b-tag value of all six jets. Right: b-tag of best combination of jets for reconstruction of W, chosen to be < 0.09.

jet is tagged as the light jet.

Therefore, another way of reconstructing the mass of hadronic W is attempted in which all jets with b-tag value less than 0.09 are combined. This value is selected by using the optimised cut value of 0.09 on the b-tag of third and fourth jet as explained in the next section. Among all these combination, that one is selected where the invariant mass of the light jet pair is closest to the W mass as shown in left figure 6.9. The remaining jets are considered as the b-jets and they are used to reconstruct $M_{bb}, M_{l\nu b}$ and M_{jjb}. Right figure 6.10 shows b-tag value of the jet pair which is chosen to reconstruct W.

6.10 Full Reconstruction of the Final State

From the six jets, four jets are tagged as b-jets (those with highest b-tag value). Top-quarks are reconstructed using a tagged b-jet and a reconstructed W candidate and the Higgs boson is reconstructed from a pair of tagged b-jets. All possible combinations of tagged b-jets are examined to reconstruct the mass of Higgs boson and both top-quarks simultaneously. Figure 6.11 shows the mass distributions for the 12 possible combinations of reconstructed Higgs and top-quarks per event.

To reduce combinatorial background, only that combination is selected per

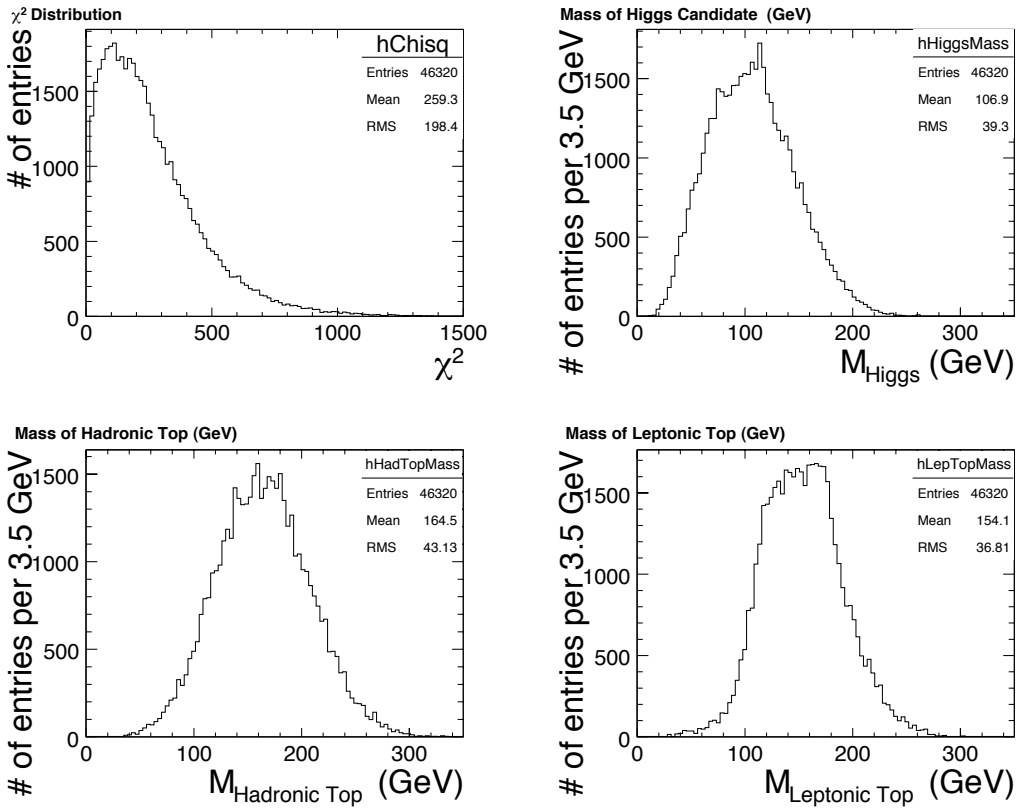

Figure 6.11: Plots for the 12 possible Higgs and top quarks combinations. Top left: χ^2, as defined in equation 6.6. Top right: Reconstructed mass of b-jet pair, M_{bb}. Bottom left: Reconstructed mass of two light- and one b-jet, M_{jjb}. Bottom right: Reconstructed mass of lepton, missing energy and b-jet, $M_{l\nu b}$.

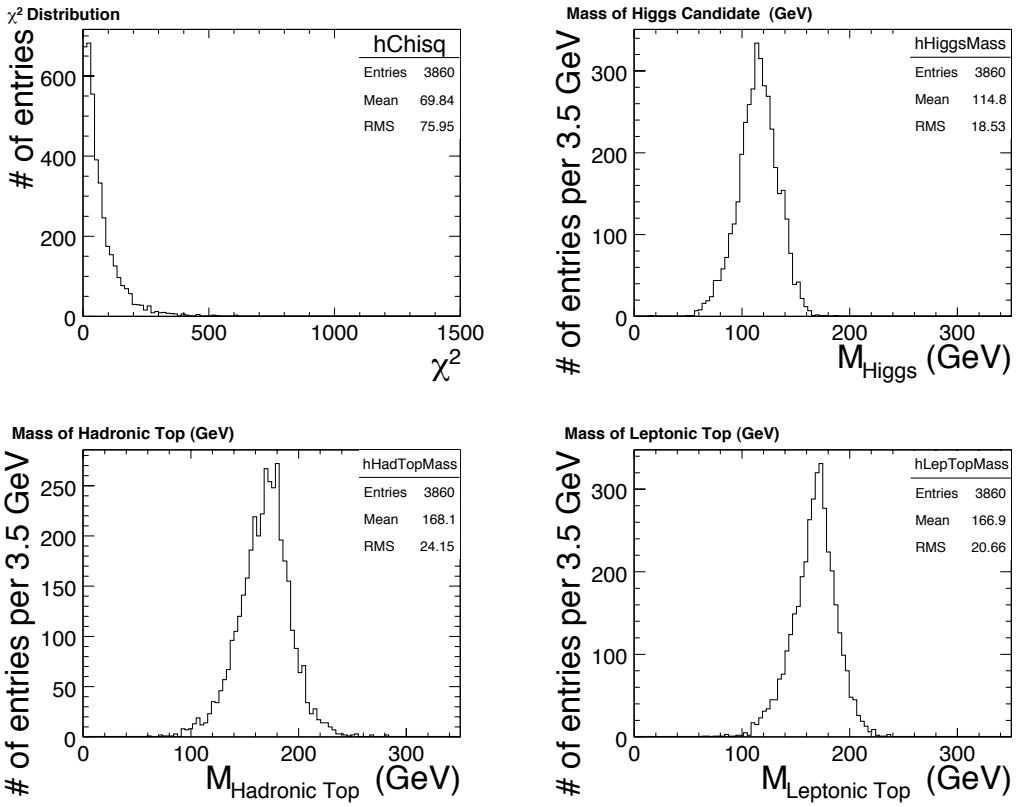

Figure 6.12: Plots for the best Higgs and top quarks combination. Top left: χ^2, as defined in equation 6.6. Top right: Reconstructed mass of b-jet pair, M_{bb}. Bottom left: Reconstructed mass of two light- and one b-jet, M_{jjb}. Bottom right: Reconstructed mass of lepton, missing energy and b-jet, $M_{l\nu b}$.

event, which minimises χ^2:

$$\chi^2 = \frac{(M_{l\nu b} - M_t)^2}{\sigma^2_{l\nu b}} + \frac{(M_{jjb} - M_t)^2}{\sigma^2_{jjb}} + \frac{(M_{bb} - M_{Higgs})^2}{\sigma^2_{bb}} \tag{6.6}$$

where the first term is from the reconstructed semi-leptonic top-quark, the second term from the hadronic top-quark reconstructed from the two light jets W, and the final contribution is from the Higgs boson, with $M_t = 175$ GeV and $M_{Higgs} = 120$ GeV. The χ^2 incorporates the uncertainties, (σ')s, on the jet energies. These σ's are determined from the mass distributions of Higgs and top quarks given by the minimisation of χ^2 with σ's considered as equal. From the Higgs and top quark mass distributions we get:

$$\begin{aligned} \sigma_{l\nu b} &= 20.7 \pm 0.2 \text{ GeV} \\ \sigma_{jjb} &= 23.5 \pm 0.3 \text{ GeV} \\ \sigma_{bb} &= 19.3 \pm 0.2 \text{ GeV} \end{aligned}$$

The mass distributions of the lowest χ^2 combination are given in figure 6.12.

6.11 Signal Background Separation

Once a full reconstruction of the final state has been achieved, we include background samples in our analysis. There are ∼400,000 events in the $t\bar{t}$ sample and 24,000 events for $t\bar{t}Z$ background process. A cut-based method is used to reduce these main background processes.

6.11.1 Selection Cuts

The following variables are used to select events to be considered for further analysis:

- $E_{AllReco}$ is the sum of the energies of all reconstructed particle in the event.
- $P_{RecoLep}$ is the reconstructed momentum of the identified lepton.
- P_{miss} is the reconstructed missing momentum.
- P_{Jets} is the momentum of each of the reconstructed jets.

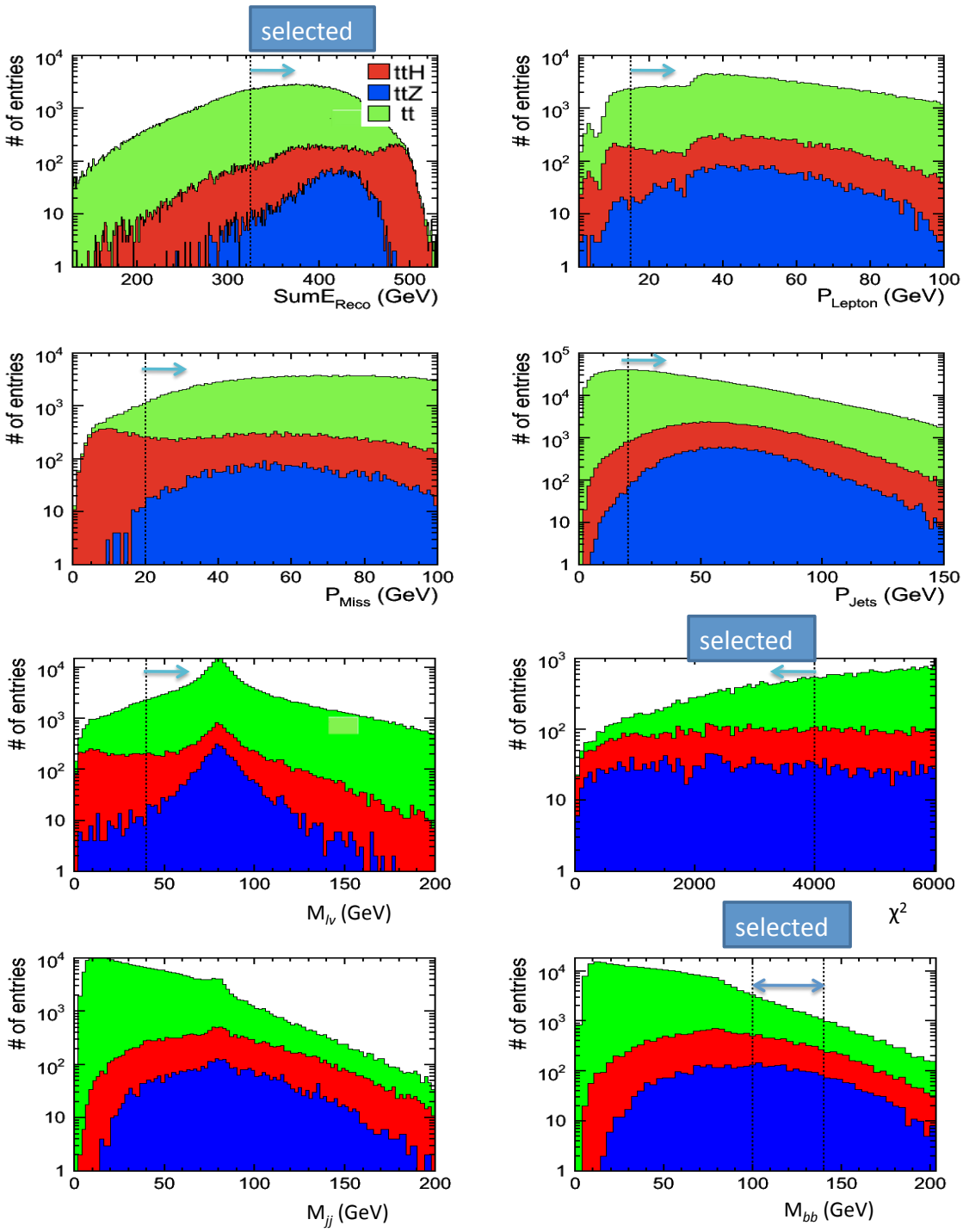

Figure 6.13: Stacked plots showing selection variables for signal and background. All distributions are randomly normalised. Left top: sum of energy of all reconstructed particles. Right top: reconstructed momentum of the charged lepton. Second row left: reconstructed missing momentum. Second row right: reconstructed momentum of jets. Third row left: reconstructed mass of the $l\nu$ pair. Third row right: χ^2. Left bottom: reconstructed mass of the light di-jet pair. Right bottom: reconstructed mass of b-jet pair. Here the dotted lines show the cut values selected.

Figure 6.13 shows the distribution of variables used to separate signal and background. In each case the cut values are chosen to maximise $\frac{S}{\sqrt{S+B}}$.

6.11.2 B-tag of Light Jets

The b-tagging information separates the signal and background quite significantly. As the background events do not have $H \rightarrow bb$, therefore the b-tag values of jet3 and jet4 can remove a significant number of background events as shown in the figure 6.14.

6.11.3 Cuts Summary

Two other variables which can improve the separation of signal and background are χ^2 and the mass of $W_{l\nu}$. The mass of the W_{jj}, which we obtain by combining the light jets tagged in order of the highest b-tag, does not help much to reduce the separation of background due to its large distribution width. Table 6.3 summarises the number of signal and background events at each consecutive step of the reconstructed procedure.

Figure 6.15 shows that the selection variable, total reconstructed mass in the event, discriminate $t\bar{t}$ background significantly. It is defined as:

$$\text{TotalM}_{Event} = m_{b\bar{b}} + m_{l\nu b} + m_{jjb}. \tag{6.7}$$

We vary the TotalM_{Event} to optimise the quantity $\frac{S}{\sqrt{S+B}}$. We select the events which have $TotalM_{Event}$ greater than 420 GeV. After applying this cut, our final state looks like as shown in figure 6.16. We notice that the signal events in M_{bb} distribution are mostly in mass window (100 , 140) GeV. Finally we apply this cut to suppress the background contribution.

The cut based selection reduces the $t\bar{t}$ background significantly to 0.11% and $t\bar{t}Z$ to 2.76%, whereas the efficiency for signal is $\sim$ 8%. Our final state is shown in figure 6.16 after applying all cuts except the Higgs mass window selection.

6.12 Measurement of $\mathbf{g_{t\bar{t}H}}$

The coupling of the Higgs boson to the fermions, scale with the fermion mass as explained in chapter 2. To measure the top Higgs Yukawa coupling in this chapter,

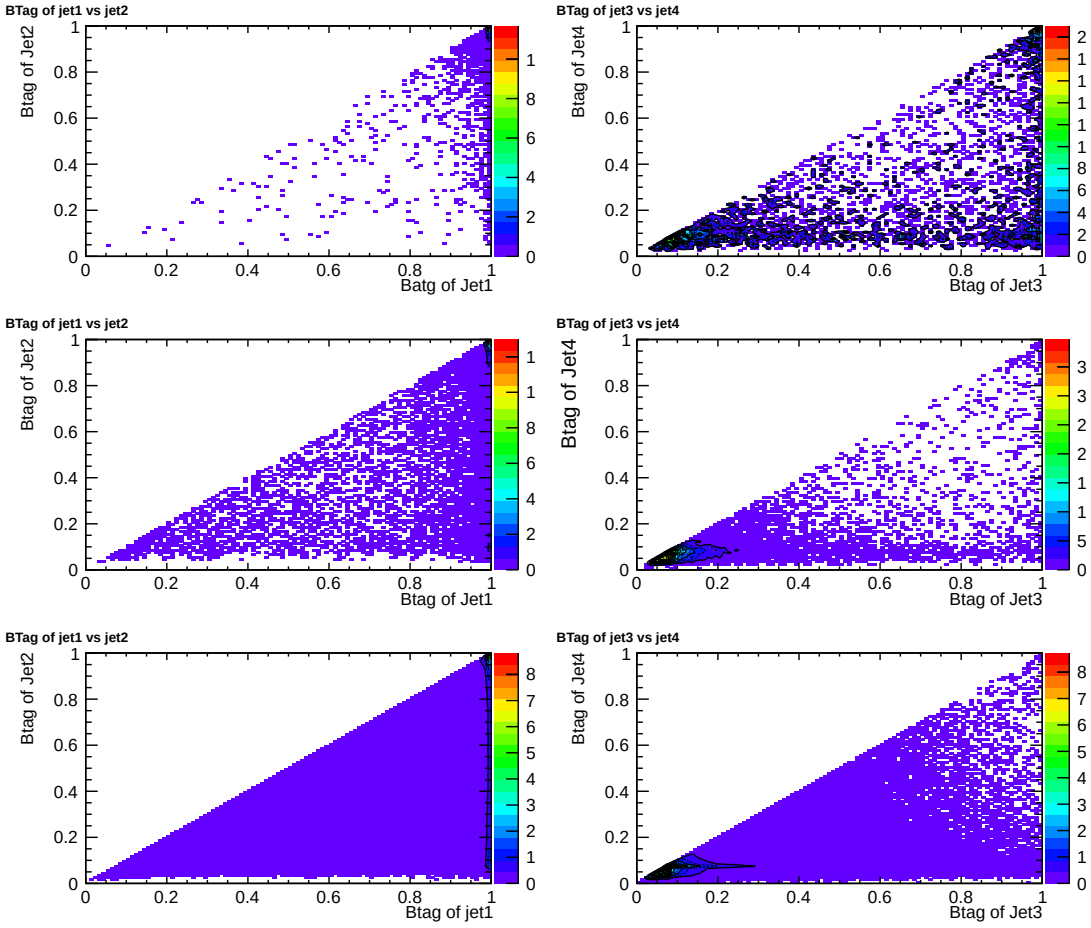

Figure 6.14: b-tag of the four tagged b-jets arranged in descending b-tag order. Top row: signal $t\bar{t}H$. Middle row: $t\bar{t}Z$ background. Bottom row: $t\bar{t}$ background. Here dotted line shows the cut value > 0.09 applied on the b-tag of 3rd and 4th jet.

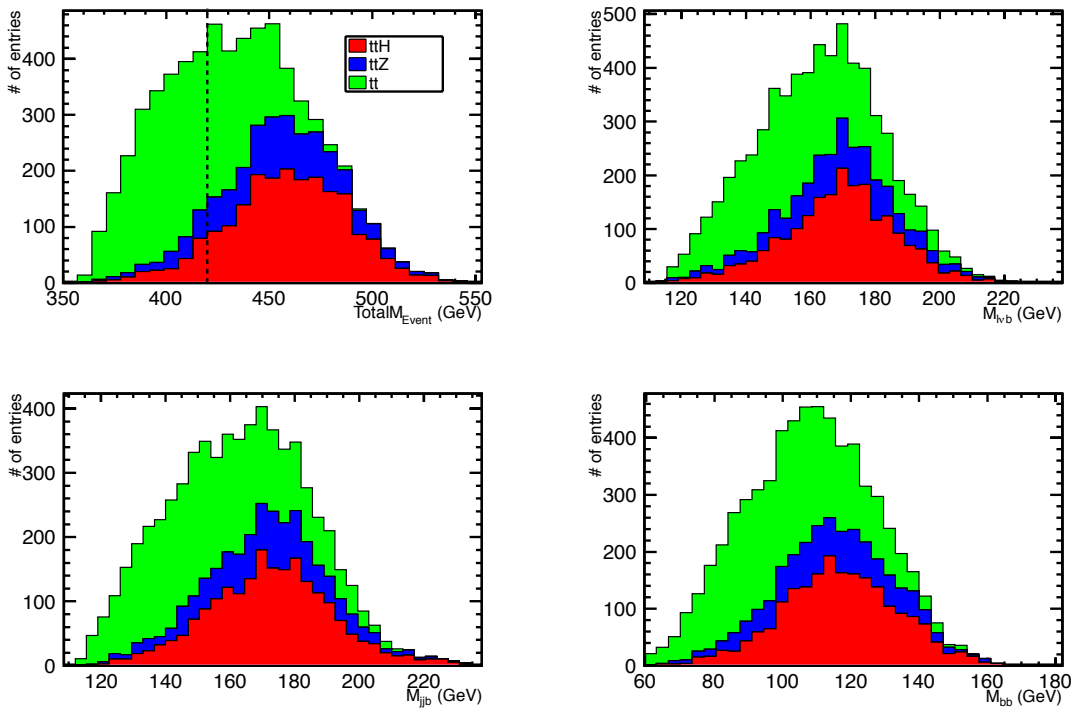

Figure 6.15: Stacked plots for the masses of Higgs and top quarks after applying the first eight selection cuts as given in table 6.3. All distributions are randomly normalised. Left top: Sum of the mass of the final state particles ($m_{b\bar{b}} + m_{l\nu b} + m_{jjb}$). Right top: Reconstructed mass of lepton, missing momentum and b-jet, $M_{l\nu b}$. Left bottom: Reconstructed mass of light- and b-jets, M_{jjb}). Right bottom: Reconstructed mass of the b-jet pair, M_{bb} pair.

Table 6.3: Cut based scheme of background and signal samples.

	Cuts	$t\bar{t}H$ Sample	$t\bar{t}Z$ Sample	$t\bar{t}$ Sample
0	Initial	20000	24000	376276
1	no. Lep > 0	3860	14536	282404
2	$E_{AllReco} > 325$ GeV	3600	8021	68439
3	$P_{RecoLep} > 15$ GeV	3167	7128	55206
4	$P_{miss} > 20$ GeV	3119	5610	54488
5	$P_{Jets} > 20$ GeV	2978	4837	33909
6	3^{rd} and 4^{th} jet b-tag > 0.09	2215	1544	11017
7	$\chi^2 < 4000$	2161	1487	1822
8	$M_{l\nu} > 40$ GeV	2135	1330	1778
9	TotalM$_{Event} > 420$ GeV	1871	873	711
10	100 GeV $< M_{bb} <$140 GeV	1513	662	464
	Accepted cross section (fb)	0.04	0.02	0.29

we followed procedure given in [88]. In an analysis, yielding a selection efficiency of the signal ϵ^{sel}_{signal} and a purity of the selected sample ρ^{sel}_{sample} and assuming an integrated luminosity of L, the statistical and systematic uncertainties on the measurement of $g_{t\bar{t}H}$ can be expressed as:

$$\left(\frac{\Delta g_{t\bar{t}H}}{g_{t\bar{t}H}}\right)_{stat} \approx \frac{1}{S_{stat}(g^2_{t\bar{t}H})\sqrt{\epsilon^{sel}_{signal}\rho^{sel}_{sample}L}} \tag{6.8}$$

$$\left(\frac{\Delta g_{t\bar{t}H}}{g_{t\bar{t}H}}\right)_{syst} \approx \frac{1}{S_{syst}(g^2_{t\bar{t}H})}\frac{1-\rho^{sel}_{sample}}{\rho^{sel}_{sample}}\frac{\Delta\sigma^{BG}_{eff}}{\sigma^{BG}_{eff}} \tag{6.9}$$

The value of L we used in finding our final results is 1000 fb^{-1}. This large value is essential to get the statistical uncertainty at the level of a few percent. At the ILC with three to four years data, 1000 fb^{-1} luminosity can be achieved at 500 GeV center-of-mass energy. $\frac{\Delta\sigma^{BG}_{eff}}{\sigma^{BG}_{eff}}$ is the relative uncertainty in the residual background normalisation. It is due to the badly known differential cross-section for $t\bar{t}$ in weakly populated phase space areas. It is sizeable and moreover difficult to estimate. In [88], two values 5% and 10% were used for this uncertainty. A study to measure the top pair production cross section at the ILC, is currently in process at LAL, Orsay [92]. Once these results are ready, we can use that value in the analysis but currently the 5% value is chosen. The large cross section and low

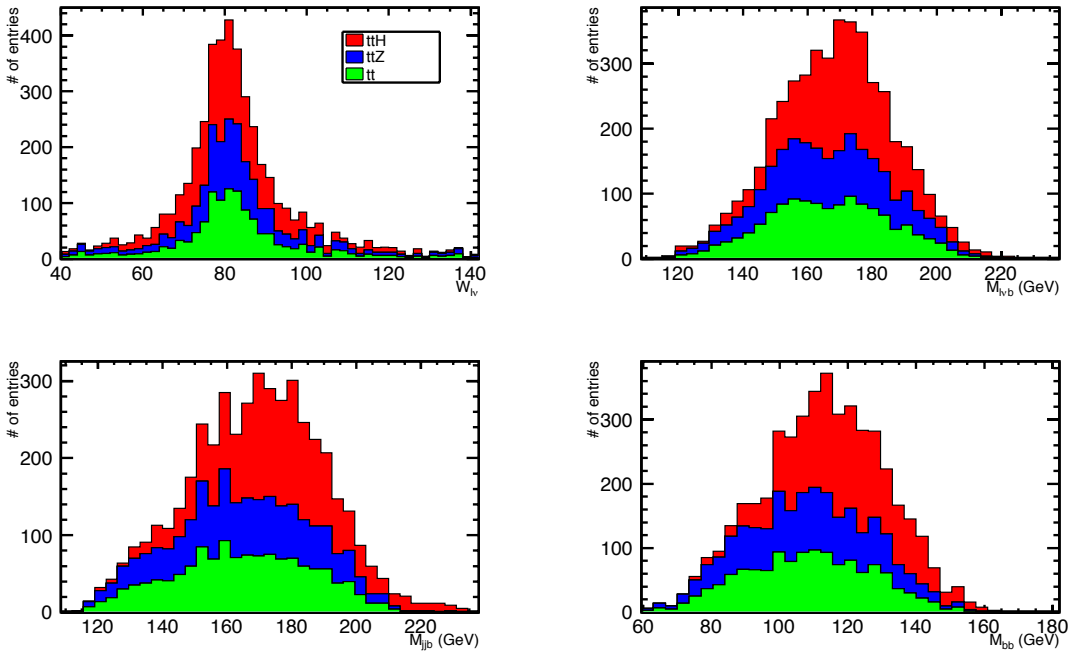

Figure 6.16: Stacked plots for the Higgs and top masses distributions after applying cuts on all selection variables including $TotalM_{Event}$. All distributions are randomly normalised. Left top: Reconstructed mass by combining charged lepton and missing momentum, $M_{l\nu}$. Right top: Reconstructed mass of $(l\nu b)$. Left bottom: Reconstructed mass of (jjb). Right bottom: Reconstructed mass of $b\bar{b}$ pair.

selection of $t\bar{t}$ background sample limits available MC sample statistically. In the systematic uncertainty, we just take into account the one which arises from the effective background normalisation since it is by far the largest one among those we can estimate. The sensitivity factors S_{stat} and S_{syst} in the above relations express the dependency of the cross section on the squared coupling:

$$S_{stat}(g^2_{t\bar{t}H}) = \frac{1}{\sqrt{\sigma_{t\bar{t}H}}} \left| \frac{d\sigma_{t\bar{t}H}}{d(g^2_{t\bar{t}H})} \right| \tag{6.10}$$

$$S_{syst}(g^2_{t\bar{t}H}) = \frac{1}{\sigma_{t\bar{t}H}} \left| \frac{d\sigma_{t\bar{t}H}}{d(g^2_{t\bar{t}H})} \right| \tag{6.11}$$

As shown in figure 2.11, the contribution from Higgs radiation off the Z to the signal cross-section is very small. In order to calculate the sensitivity factors, we will thus neglect it, allowing a very simple calculation. In this approximation, we can write:

$$\sigma_{t\bar{t}H} \approx g^2_{t\bar{t}H} F(m_H, m_t, s) \tag{6.12}$$

And thus:

$$\frac{d\sigma_{t\bar{t}H}}{d(g^2_{t\bar{t}H})} \approx F(m_H, m_t, s) \approx \frac{\sigma t\bar{t}H}{(g^2_{t\bar{t}H})} \tag{6.13}$$

where s is the squared collision energy. The values of S_{stat} and S_{syst} for $m_H = 120$ GeV and $\sqrt{s} = 500$ GeV are:

$$S_{stat} = 1.50 \text{ fb}^{1/2} \tag{6.14}$$

$$S_{syst} = 1.98 \tag{6.15}$$

6.13 Results

In the previous section a description of cuts applied to separate signal and background is given. The cut values are chosen such that the quantity $\frac{S}{\sqrt{S+B}}$ maximises. We define efficiency and purity of sample as:

$$\epsilon_{sel} = \frac{\text{number of events passing the cuts}}{\text{Total number of events}} \tag{6.16}$$

$$\rho^{sel}_{sample} = \frac{S}{S+B}. \tag{6.17}$$

We scale our signal and background to the luminosity 1000 fb^{-1}. Figure 6.17 shows the distribution for the scaled signal and background samples. The main background after selection is due to the top-pair production. Table 6.4 summarises the efficiency and effective cross section for signal and background and table 6.5 gives the systematic and statistical uncertainties on the measurement of the coupling for the case where $m_H = 120$ GeV and $\frac{\Delta\sigma_{eff}^{BG}}{\sigma_{eff}^{BG}} = 5\%$.

Table 6.4: Selection efficiencies and corresponding effective cross sections.

Final State	ϵ_{sel} (%)	σ_{eff} (fb^{-1})
$t\bar{t}H$	7.57 ± 0.19	0.04
$t\bar{t}$	0.116 ± 0.005	0.29
$t\bar{t}Z$	2.76 ± 0.12	0.02

Table 6.5: Expected uncertainty on the measurement of coupling. Selection efficiency of the signal and purity of the selected sample are shown.

Parameter	value (%)
$\frac{\Delta\sigma_{eff}^{BG}}{\sigma_{eff}^{BG}}$	5
ϵ_{sel}	7.6 ± 0.2
ρ_{sample}^{sel}	12.5 ± 0.3
$\left(\frac{\Delta g_{t\bar{t}H}}{g_{t\bar{t}H}}\right)_{stat}$	21.6
$\left(\frac{\Delta g_{t\bar{t}H}}{g_{t\bar{t}H}}\right)_{syst}$	17.6
$\frac{\Delta g_{t\bar{t}H}}{g_{t\bar{t}H}}$	27.9

6.14 Discussion

The expected precision on measuring the top-Higgs Yukawa coupling is better than 28% for $m_H = 120$ GeV, if the knowledge of $t\bar{t}$ background normalisation is known at the 5% level. Much of the uncertainty on the results of this analysis is due to the small cross section of the $t\bar{t}H$ signal process. Even though the signal cross section is very small at the $\sqrt{s} = 500$ GeV, yet 28% accuracy is achieved. At higher energies, the cross section of the signal process is larger, therefore it

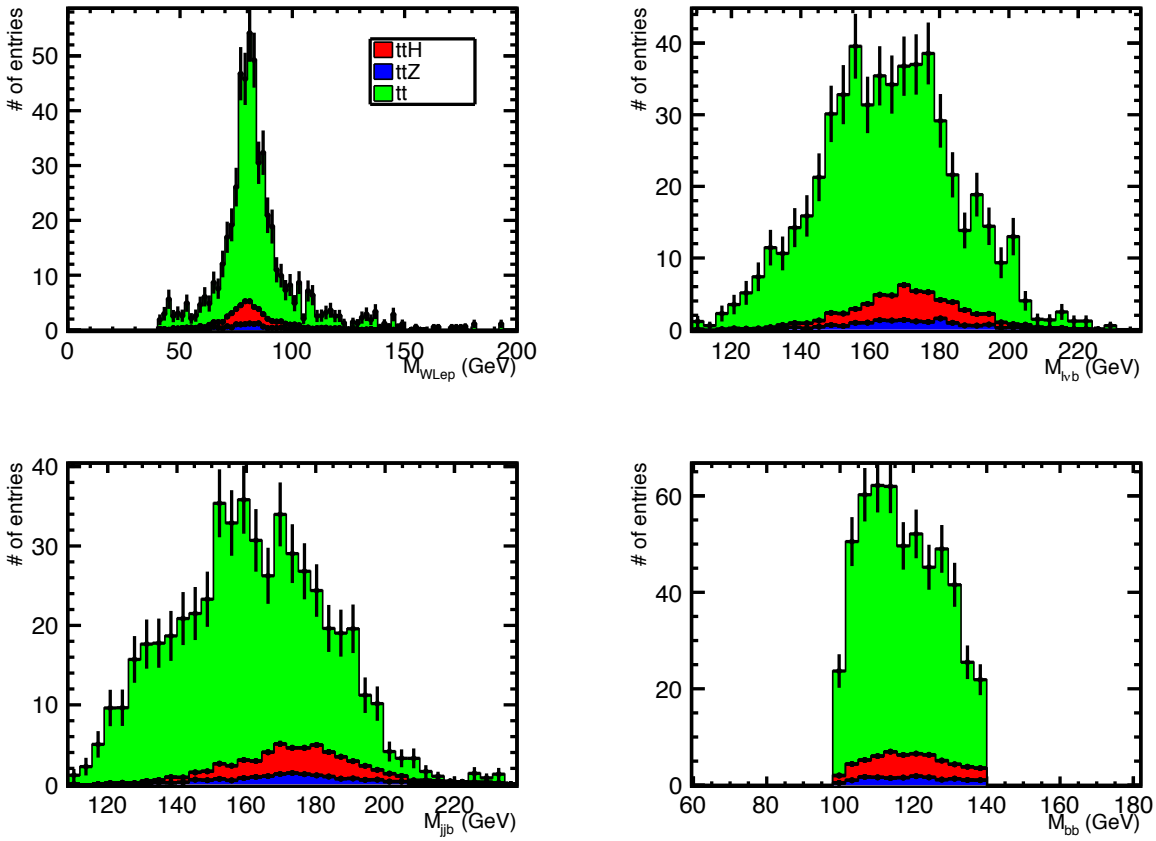

Figure 6.17: After applying all selection cuts, the scaled signal and background distributions for Higgs and top masses. Left top: Reconstructed mass by combining charged lepton and missing momentum, $M_{l\nu}$. Right top: Reconstructed mass of $(l\nu b)$. Left bottom: Reconstructed mass of (jjb). Right bottom: Reconstructed mass of $b\bar{b}$ pair.

motivates an increased center of mass energy for the ILC. For example, at $\sqrt{s} =$ 800 GeV, the signal to background ratio decreases to $\sim$ 100 as compared to the ratio $\sim$ 900 at 500 GeV.

Certainly there is room for improvement of the study presented in this chapter. As explained for the Higgs branching ratio analysis (section 5.10), jet finding can be re-examined to refine the flavour tagging. Improved jet finding and flavour tagging processors are available recently in the new ILC software but a study of the top-Higgs Yukawa coupling analysis with this version of software is beyond the scope of this thesis.

One of the areas of consideration is the improvement in the hadronic W reconstruction. A cut on the b-tag value of the jets is used to identify light jets which are then combined to reconstruct the W boson. This cut was decided to accommodate the selection cut on b-tag of third and fourth jet. A re-examining of the cut on b-tag of fifth and sixth jet could recover the signal events with a b-tag > 0.09 and hence, improve the efficiency and purity of the sample.

A cut based strategy is applied to discriminate the signal and background events. It is shown in previous studies that the use of neural network and likelihood methods can perform the signal background separation with better efficiency [91]. Hence, it is anticipated that a 2-3% improvement in the precision can be achieved by using neural network analysis.

For the current study, six fermion backgrounds are not included but reference [88] shows that the loss of precision on $g_{t\bar{t}H}$ measurement is negligible due to this background. An amendment in the analysis involves the $t\bar{t}$ background normalisation which is 5% in our analysis. If the exact background normalisation $\frac{\Delta\sigma^{BG}_{eff}}{\sigma^{BG}_{eff}}$ is used, our results might change. Once the results from the group working on measuring the cross section of top pair production [92] are ready, they can be included in the analysis.

Chapter 7

Summary and Conclusions

In this thesis we have presented two studies measuring the coupling of the Standard Model Higgs boson to quarks using the proposed ILD detector at the proposed ILC collider. In both cases we have used a Higgs boson with mass of 120 GeV. If a SM-like Higgs boson exists, it's very likely to be found at LHC which is currently operational. However, as LHC is a hadron collider, it may not be possible to measure the interesting properties of Higgs boson which could discriminate the SM from the other models, such as Supersymmetry. Therefore, one purpose of the ILC is to precisely specify the properties of Higgs boson. Two key properties are the coupling of Higgs with the heaviest quark, top, and different branching ratios of Higgs to quarks. These properties are predicted to be poorly measured at the LHC.

In the first part of this thesis, a study of the Higgs branching ratio measurements was conducted. The channel studied is $ZH \rightarrow \mu^+\mu^- H$ at 250 GeV center of mass energy. The main background is ZZ production. Muons were identified using a Neural Network. The identified muons were removed from the sample and the remaining particles were used to reconstruct exactly two jets. Subsequently, successive cuts were applied to suppress the background process. b- and c-tagging was then used to distinguish between the final states of the Higgs decay. In this study, the SM branching ratio of Higgs to $b\bar{b}$ can be measured with a precision of 4% with an integrated luminosity of 250 pb^{-1}. Similarly, the SM branching ratios to $c\bar{c}$ and gg are both measured with precision of $\sim 45\%$. Results from other independent studies were combined with the branching ratio analysis presented in this thesis for the ILD Letter of Intent [50]. Including a

5% uncertainty on Higgs production cross section, the combined precision on the BRs are 5.5% for $b\bar{b}$ and 15% for $c\bar{c}$.

The second study for this thesis involved measuring the top Higgs Yukawa coupling using the $t\bar{t}H$ production at 500 GeV. The top quark always decays as $t \rightarrow bW$. The semi-leptonic channel was investigated where one W boson decays into leptons and other into light jets and the Higgs boson decays into b-jets. The full reconstruction of the final state is performed by identifying the charged lepton and reconstructing the missing momentum and six jets. b-tagging plays a crucial role in identifying different jet flavours. Among six jets in the final state, four are tagged as b-jets and two as light jets. The leptonic and hadronic W bosons are reconstructed by combining the charged lepton and missing momentum information and the two light jets, respectively. The combinatorial background, in reconstructing final state top quarks and Higgs using the four b-tagged jets, is suppressed by minimising the χ^2:

$$\chi^2 = \frac{(M_{l\nu b} - M_t)^2}{\sigma^2_{l\nu b}} + \frac{(M_{jjb} - M_t)^2}{\sigma^2_{jjb}} + \frac{(M_{bb} - M_{Higgs})^2}{\sigma^2_{bb}}$$

where the $M_{l\nu b}$, M_{jjb} and M_{bb} are the reconstructed invariant masses of the leptons and jets, σ are the resolutions of the reconstructed invariant masses and M_{Higgs} and M_t are the Higgs and top quark masses respectively. To discriminate the signal, $t\bar{t}H$, and background $t\bar{t}$ and $t\bar{t}Z$ processes, selection cuts are applied. In this analysis, top Higgs Yukawa coupling is measured with a precision of 28% including an uncertainty of 5% on the cross section normalisation of the $t\bar{t}$ background.

We have studied the prospects of precise measurement of the Higgs boson branching ratios and top quark Yukawa coupling during the first phase of the ILC with center of mass energy 500 GeV. These shows that a $\sqrt{s} = 500$ GeV collider adds enough to our physics knowledge to justify the project. However, an upgrade to $\sqrt{s} = 1$TeV increases significantly the value of the ILC. The ILC will be essential to interplay the LHC discoveries and move forward on our understanding of the Higgs physics. Both analyses in this thesis are the optimised studies performed for the ILD_00 detector model. They do not represent the ultimate ILD performance as significant improvements in the analyses are possible. However, the precision achieved by these studies showed that the ILD detector concept

meets the requirements for an ILC detector.

Bibliography

[1] S.L. Glashow *Nucl. Phys. 22*: 579-588 (1961) A. Salam, *Weak and electromagnetic interactions, Proceedings of the Nobel Symposium*, held 1968 at Lerum, Sweden

[2] S. Weinberg *Phys. Rev. Lett. 19*, 1264-1266c (1967)

[3] A. Salam (1968). N. Svartholm ed. *Elementary Particle Physics: Relativistic Groups and Analyticity* Eighth Nobel Symposium. Stockholm: Almquvist and Wiksell. pp. 367

[4] J. Gunion, H. Haber, G. Kane, and S. Dauson, *The Higgs Hunters Guide*, Addison Wesley, Reading (USA),1990.

[5] H. Georgi, S.L. Glashow. *Phys. Rev. Lett. 33*, 614 (1974)

[6] Peter W. Higgs *Phys. Rev. Lett. 13*, 508-509 (1964)

[7] D. I. Kazakov, *Beyond the Standard Model (In Search of Supersymmetry)* (hep-ph/0012288v2)

[8] W. Greiner, B. Muller *Gauge Theory of Weak Interactions.* Springer, 2009

[9] F. Cooper, A. Khare and U. Sukhatme. *Phys. Rep. 251* (1995) 267-85

[10] S. Weinberg, *The Quantum Theory of Fields, Volume 3: Supersymmetry*, Cambridge University Press, Cambridge, (1999).

[11] S. Stephen P. Martin *A Supersymmetry Primer* (hep-ph/9709356v5)

[12] K. Nakamura et al. (Particle Data Group) J. Phys. G**37**, 075021 (2010)

[13] G. Altarelli, Ferruccio Feruglio. CERN-PH-TH/2004-079, DFPD-04/TH/11, May 2004. 44pp (hep-ph/0405048v2)

[14] R. N. Mohapatra *Phys.Scripta T121* (2005) 185-191 (hep-ph/0412050)

[15] S. Y. Choi 12 Nov 2007. - 9 p. *15th International Conference on Supersymmetry and the Unification of Fundamental Interactions*, Karlsruhe, Germany, 26 Jul - 1 Aug 2007 (arXiv:0711.1393)

[16] J. R. Ellis, J. S. Hagelin, D. V. Nanopoulos, K. A. Olive and M. Srednicki, Nucl. Phys. B **238** (1984) 453.

[17] J. Bagger et al. *The LHC Theory Initiative from the Standard Model to New Physics,* http://www.pas.rochester.edu/∼orr/lhc-ti_whitepaper.pdf

[18] *ATLAS Collaboration, Physics TDR*, CERN-LHCC-99-14 and CERN-LHCC-99-15.

[19] *CMS Collaboration, Physics TDR*, CERN/LHCC/2006-021, June 2006 .

[20] *LHCb Collaboration, Physics TDR*, CERN-LHCC-98-004, LHCC-P-4.

[21] W.N. Cottingham, D. A. Greenwood *An Introduction to the Standard Model of Particle Physics*, Cambridge University Press, Cambridge, (1998).

[22] S. F. Novaes (hep-ph/0001283)

[23] J. R. Espinosa, Surveys High Energ. Phys. **10** (1997) 279-311. [hep-ph/9606316].

[24] A. Djouadi. The Anatomy of elecroweak symmetry breaking. I: The Higgs boson in the standard model. *Phys. Rept.*, 457:1-216, (2008)

[25] A. Djouadi et al. *International Linear Collider Design Report Volume 2: Physics at the ILC*. 2007.

[26] C. Farrell, A. H. Hoang, Phys. Rev. **D74** (2006) 014008.

[27] R. Barate *et al.* [LEP Working Group for Higgs boson searches, the ALEPH Collaboration, the DELPHI Collaboration, the L3 Collaboration and the OPAL Collaboration], Phys. Lett. B **565** (2003) 61 [arXiv:hep-ex/0306033].

[28] J. Erler, Phys. Rev. **D81**, 051301 (2010). [arXiv:1002.1320 [hep-ph]].

[29] *Combined CDF and D0 Upper Limits on Standard Model Higgs Boson Production with up to 8.6 fb^1 of Data*, FERMILAB-CONF-11-354-E [arXiv:1107.5518 [hep-ex]].

[30] D.R.T. Jones and S.T. Petcov, *Phys. Lett.* **B84** (1979) 440.

[31] M. A. Travel *Transp.Theory Statist.Phys.1*:183-185,(1971).

[32] S. F. Novaes (Sao Paulo, IFT) *Standard model: An Introduction.* IFT-P-010-2000, Jan 1999. 101pp. To be published in the proceedings of 10th Jorge Andre Swieca Summer School: Particle and Fields, Sao Paulo, Brazil, 31 Jan - 12 Feb 1999. In *Sao Paulo 1999, Particles and fields* 5-102. [hep-ph/0001283]

[33] http://gfitter.desy.de/GSM/

[34] H. Flacher, M. Goebel, J. Haller, A. Hocker, K. Monig and J. Stelzer, Eur. Phys. J. C **60** (2009) 543

[35] J. D. Lykken, CERN Yellow Report CERN-2010-002, 101-109. [arXiv:1005.1676 [hep-ph]].

[36] J. D. Wells, [arXiv:0909.4541 [hep-ph]].

[37] http://acfahep.kek.jp/acfareport/node30.html

[38] Ties Behnke *J. Phys.: Conf. Ser. 53*, 371 (2006)

[39] http://www.linearcollider.org/GDE/Director%27s-Corner/2010/2-December-2010—Evolving-the-ILC-baseline

[40] http://pdg.lbl.gov/2011/reviews/rpp2011-rev-accel-phys-colliders.pdf

[41] E. J. N. Wilson, *An introduction to particle accelerators* , Oxford University Press, 2001, ISBN 0198508298

[42] B. W. Lee, C. Quigg and H. B. Thacker, *Phys. Rev. D16*, 1519, (1977).

[43] J. Brau (ed.) et al. *International Linear Collider reference design report. 4: Detectors.* ILC-REPORT-2007-001.

[44] http://www.docstoc.com/docs/23406448/REPORT-OF-THE-THIRD-MEETING-OF-THE-ILC-PROJECT

[45] ILC Detector R&D Panel. ILC Detector R&D Panel website. https://wiki.lepp.cornell.edu/ilc/bin/view/Public/WWS/.

[46] M. A. Thomson, *Progress with Particle Flow Calorimetry* arXiv:0709.1360 [physics.ins-det].

[47] http://newsline.linearcollider.org/2011/04/14/low-power-option-adopted-for-ilc-technical-design-baseline/reduced-parameter-set-2/

[48] http://www.kek.jp/acc/eng/topics/topics101209.html

[49] http://tesla.desy.de/TTF_intro.html

[50] M. Thomson. et al. *Letter of Intent for the ILD detector concept.*

[51] H. Aihara, P. Burrows, M. Oreglia et al. *Letter of Intent for the SiD detector concept.*

[52] CMS Collaboration, G. Acquistapace et al., *CMS, the magnet project: Technical design report.* http://cmsdoc.cern.ch/ftp/TDR/MAGNET/magnet.html. CERN-LHCC-97-10.

[53] A. Hervè, F. Kircher, et al., *Experience Gained from the Construction, Test and Operation of the Large 4-T CMS Coil* in IEEE Trans. on Appl. Superc., vol. 18-2, pp. 346351. 2008.

[54] T. J. Chapin, R. L. Cool, K. Goullianos, J. P. Silverman, G. R. Snow, H. Sticker, S. N. White, and Y.-H. Chou. Development and performance of a high pressure hydrogen time projection chamber. *Nuclear Instruments and Methods in Physics Research*, 197(2-3):305 315, 1982.

[55] C. Lippmann and the ALICE collaboration. *The Time Projection Chamber for the ALICE Experiment*. 2008. arxiv:0809.5133v2[nucl-ex]

[56] GLD Concept Study Group, K. Abe et al., GLD detector outline document arXiv:physics/0607154.

[57] LDC Working Group, D. Kisielewska et al., Detector Outline Document for the Large Detector Concept. http://www.ilcldc.org/documents/dod/.

[58] A. Fedorov et al. Letter of Intent from the Fourth Detector Collaboration at the International Linear Collider: http://www.4thconcept.org/4LoI.pdf.

[59] http://irfu.cea.fr/Sap/en/Phocea/Vie_des_labos/Ast/ast_technique.php?id_ast=2307

[60] ILCInstall Homepage, http://ilcsoft.desy.de/portal/software packages/ilcinstall/.

[61] http://ilcsoft.desy.de/portal/software packages/lcfivertex/.

[62] http://ilcsoft.desy.de/portal/software packages/marlinreco/.

[63] Mokka Homepage, http://polzope.in2p3.fr:8081/MOKKA.

[64] The WHIZARD Event Generator, http://whizard.event-generator.org/.

[65] GEANT4 Collaboration, S. Agostinelli et al., GEANT4: A simulation toolkit *Nucl. Instrum. Meth.* A506 (2003) 250303

[66] F. Gaede and J. Engels, *Marlin et al - A software Framework for ILC detector R&D*. http://www.eudet.org/e26/e27/e584/eudet-report-2007-11.pdf. EUDET-Report-2007-11.

[67] LCFI Collaboration, S. Hillert, *The LCFIVertex Package: vertex detector-based Reconstruction at the ILC*. Nucl.Instrum.Meth.A610:573-589, (2009)

[68] GEAR - a geometry description toolkit for ILC reconstruction software. http://ilcsoft.desy.de/portal/software_packages/gear.

[69] M. A. Thomson, *Particle flow calorimetry at the ILC*, AIP Conf. Proc. 896 215-224 (2007).

[70] M. A. Thomson, Nucl. Instrum. Meth. **A611** (2009) 25-40. [arXiv:0907.3577 [physics.ins-det]].

[71] http://hep.ph.liv.ac.uk/ green/silc/talks/MitaroffRaveVertigo.pdf

[72] S. Catani, Y. L. Dokshitzer, M. Olsson, G. Turnock and B. R. Webber, Phys. Lett. B **269** (1991) 432.

[73] S. M. Xella Hansen, M. Wing, D. J. Jackson, N. De Groot, and C. J. S. Damerell. *Update on flavour tagging studies for the future linear collider using the BRAHMS simulation*. LC-PHSM-2003-061.

[74] B. Badelek *et al.* [ECFA/DESY Photon Collider Working Group], Int. J. Mod. Phys. A **19** (2004) 5097 [arXiv:hep-ex/0108012].

[75] T. Abe *et al.* [American Linear Collider Working Group], in *Proc. of the APS/DPF/DPB Summer Study on the Future of Particle Physics (Snowmass 2001)* ed. N. Graf, arXiv:hep-ex/0106055, arXiv:hep-ex/0106056, arXiv:hep-ex/0106057, arXiv:hep-ex/0106058.

[76] G. Moortgat-Pick *et al.*, Phys. Rept. **460**, 131 (2008) [arXiv:hep-ph/0507011].

[77] T. Kuhl and K. Desch. *Simulation of the measurement of the hadronic branching ratios for a light Higgs boson at the ILC*. LC-PHSM-2007-001.

[78] Mark Grimes, *A Study of the Measurement of the Standard Model Higgs Boson Branching Ratios at the International Linear Collider* PhD thesis, *Bristol University*, 2009.

[79] R. Walsh, https://www.wiki.ed.ac.uk/display/Walsh/flavour+tagging+performance

[80] http://www-flc.desy.de/simulation/databasereco/

[81] http://tmva.sourceforge.net/

[82] https://svnsrv.desy.de/viewvc/marlinreco/MarlinReco/tags/v00-19/PFOID/

[83] http://ilcsoft.desy.de/portal/software_packages/lcfivertex/

[84] J. C. Brient. *Measurement of the Higgs decays into W W* at future e+ e- linear colliders*. LC-PHSM-2004-002, http://www-flc.desy.de/lcnotes/.

[85] G. Moortgat-Pick et al., [POWER Collaboration], *Polarized positrons and electrons at the linear collider*. Physics Reports 460 (2008) 131

[86] http://www.ilcild.org/documents/ild-letter-of-intent/ild-loi-material/zh_note_idag.pdf/view

[87] R.N. Cahn and S. Dawson, *Phys. Lett. B136*, 196 (1984).

[88] Arnaud Gay *Eur.Phys.J.C*49:489-497,2007

[89] H.Baer, S. Dawson and L. Rein *Phys.Rev.D* 61 (2000), 013002

[90] http://geant4.slac.stanford.edu/SLACTutorial09/ParticleGun.pdf

[91] A. Juste, G. Merino, [hep-ph/9910301].

[92] Philippe Doublet (LAL) http://ilcagenda.linearcollider.org/conferenceDisplay.py?confId=4983